ELPH

Annual Report 2019

Research Center for Electron Photon Science
Tohoku University

Preface

We are pleased to issue the “ELPH Annual Report 2019” that covers scientific and technical activities carried out at Research Center for Electron Photon Science (ELPH), Tohoku University in FY2019 (April, 2019 to March, 2020).

The ELPH has been in a second organization term of Joint Usage / Research Centers. The Joint Usage / Research Centers (JURC) system was engaged in FY2010 by the Ministry of Education, Culture, Sports, Science and Technology (MEXT) to encourage and promote collaborative research passing through the border of respective universities. In FY2018, an interim evaluation for the first half term was performed. Thanks to great support of ELPH users, we received “A” evaluation. However we have still suffered shortage of budget that is crucial problem for university accelerator facilities, such as ELPH. To save the electricity cost, a solid state RF system for the synchrotron was introduce last spring. Although we had expected a great reduction of the electricity power consumption, the unit prices increase of it has been significantly passed the electricity saving.

“The ELPH Symposium”, which is to explore the interest of basic for mutual collaboration between difference scientific fields, has been annually. In March 2020, the 3rd ELPH symposium had been scheduled and Prof. Ryosuke Kodama, director of the Institute of Laser Engineering, Osaka University, and Prof. Katsuhiro Sano of Center of Northeast Asian Studies, Tohoku University were invited to give special lectures. Unfortunately the symposium was not implemented due to Covid-19 pandemic. Though it was very much disappointing we hope human beings overcome the pandemic very soon, and sincerely ask facility users and related scientific field communities for continuous supports and cooperation.

November 2020
Director
Hiroyuki Hama

ELPH Annual Report 2019

Contents

I. Papers

Ⅱ. Status Report

Ⅲ. List of Publication

Ⅳ. Members of Committees

Ⅴ. Approved Experiments

I. Papers

(ELPH Experiment : #2500, #2501)

Performance test of Water Cherenkov Detector for the J-PARC H-Dibaryon Search Experiment

S.W. Choi[1], J.K. Ahn[1], S. Hayakawa[2], Y. Ichikawa[2], W.S. Jung[1], B.M. Kang[1], S.H. Kim[1], and H. Sako[2]

[1]*Department of Physics, Korea University, Seoul 02841, Republic of Korea*
[2]*Advanced Science Research Center, Japan Atomic Energy Agency, Tokai 319-1195, Japan*

We have developed a water Cherenkov detector (WC) for the H-dibaryon search experiment (E42) at J-PARC. The WC was designed to suppress low-momentum proton-associated triggers. It consists of 20 WC modules placed most downstream of the E42 spectrometer. We commissioned a WC module using 460-MeV positrons at ELPH. We measured the individual photomultiplier signals at both ends of the WC module and the summed signal. The number of photoelectrons was obtained as 33.7 ± 0.05 with a custom-made signal mixer. The summed signal was found to decrease the position and angular dependences of the WC output, thereby providing stable online trigger.

§1. Introduction

A six-quark H-dibaryon is searched for via ^{12}C(K^-,K^+) reaction at 1.8 GeV/c in the J-PARC Hadron Experimental Facility [1]. Outgoing charged particles are reconstructed with two dipole spectrometers. The Hyperon spectrometer consists of a conduction-cooled superconducting magnet [2] and a GEM-based time projection chamber [3] surrounded by 32 plastic scintillators with MPPC readouts. The forward KURAMA spectrometer constitutes a dipole magnet, three drift chambers, trigger scintillators, a time-of-flight counter, and two Cherenkov detectors. A large array of 20 water Cherenkov detectors (WC) is placed most downstream of the E42 apparatus. The WC was designed to suppress online triggers due to low-momentum protons.

We commissioned a WC module using 460-MeV positrons at ELPH. We report the performance of the WC, which includes the number of photoelectrons for individual and summed readouts, the position and angular dependences, and a custom-made mixer logic circuit.

§2. Design of Water Cherenkov Detector

The design of the WC structure was based on the small-size WCs of the J-PARC E05 pilot experiment studying Ξ^- hypernuclear spectroscopy via (K^-,K^+) reaction [4]. The WC array is composed of 20 WC modules alternatively stacked in two layers. The WC module is made of 20-mm thick acrylic to form a rectangular hollow vessel with a dimension of $257 \times 207 \times 1880$ mm^3. The acrylic vessel was fixed with polymerization except the top lid. The inner rectangular pipe was wrapped with Tyvek diffuse reflector sheets. The top lid was glued later to the vessel with silicone sealant.

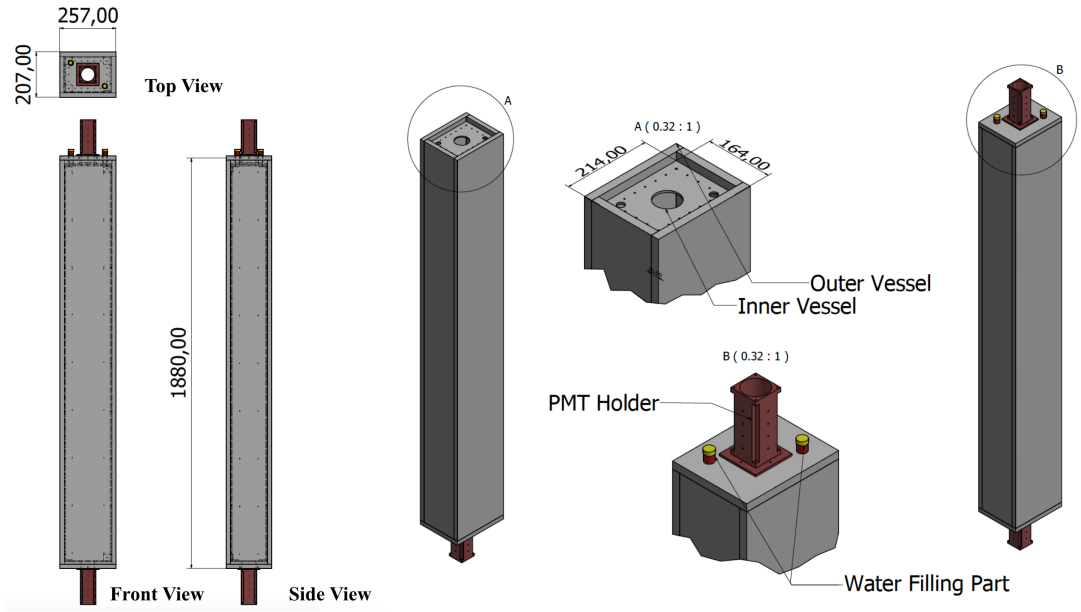

Fig.1. Schematic of a water Cherenkov detector for the beam test.

Cherenkov light propagates in water medium and enter photomultiplier tubes (PMT) (Hamamatsu H11284-100UV) through 5-mm thick UV-transparent acrylic window (ACRYLITE # 000) at both ends of the WC. The PMT has UV-transparent quartz window and super bialkali photocathode with the peak quantum efficiency of 35% at 350 nm. The PMTs are optically coupled to the acrylic window with optical grease (RX-688).

§3. Beam test with positron beam

We tested a WC module using 460-MeV positrons at Research Center for Electron Photon Science, Tohoku University (ELPH). The positron beam intensity ranges up to 1 kHz. Fig. 2 represents a photo of the ELPH test setup. The WC was installed between T1 and T2 trigger detectors. The T1 is composed of two plastic scintillation counters, each of which was perpendicularly placed and separated by 2 mm. At the most downstream, a veto counter with a ϕ25 hole was installed to reject background events from electromagnetic shower. The alternative trigger detector T3 was also prepared in front of the T2 counter to increase the online trigger rate. Detailed information of the detectors is listed in Table 1. The WC data were collected with 4-fold coincidence trigger.

3.1 Experimental Setup

The WC position and direction were changed using a lifter. We collected data with beam positions along the y-axis at angles $\theta_y = 0^\circ$ and 15°, and along the x-axis at an angle $\theta_x = 0^\circ$. The z-axis is directed in parallel to the beam direction. We also took data at $(x, y) = (0.0)$ with various incident angles.

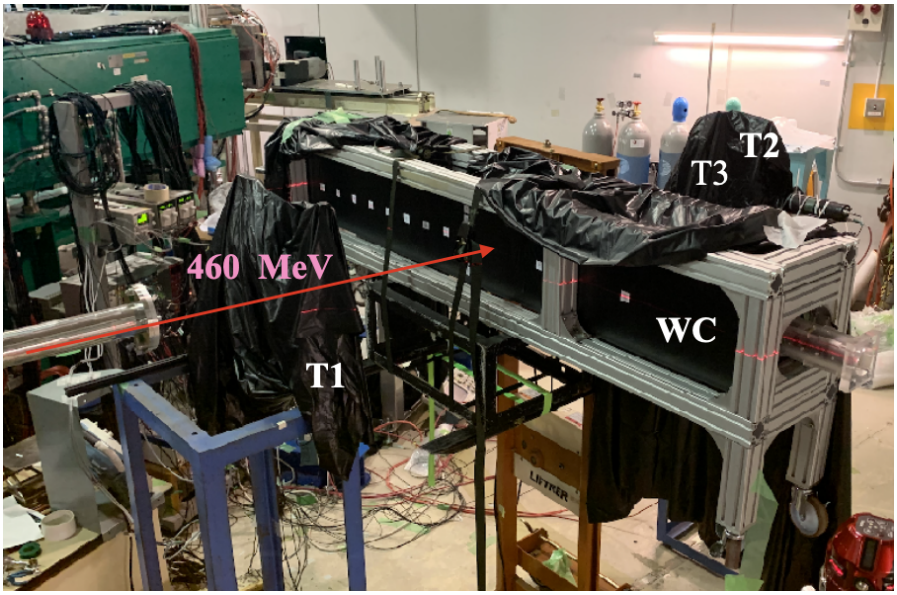

Fig.2. Photo of the experimental apparatus.

Detector	Distance [mm]	Size [mm]	Remarks
T1	300	$13^W \times 100^H \times 5^T$	Plastic Scintillation Counter (Trigger, MPPC Readout)
WC	403.5	$257^W \times 207^H \times 1880^T$	Water Cherenkov Detector (SBA-UVT PMT Readout)
T3	1510	$50^W \times 150^H \times 5^T$	Plastic Scintillation Counter (PMT Readout)
T2	1650	$13^W \times 100^H \times 5^T$	Plastic Scintillation Counter (MPPC Readout)
V(Veto)	1719	$200^W \times 200^H \times 5^T$ (ϕ25 hole in the center)	Plastic Scintillation Counter (PMT Readout)

Table 1. Locations and sizes of the detectors in the ELPH beam test

3.2 WC Mixer Logic

As the WC signal is involved in the online trigger of the J-PARC E42, it is crucial to make the WC signal height independent of the hit locations on the WC module. We developed a signal mixer logic to test if the summed signal can be used for the WC trigger signal.

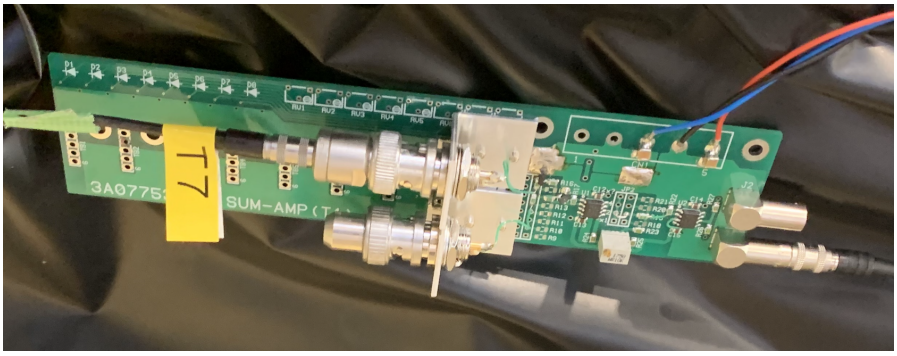

Fig.3. Photo of the WC mixer logic with two inputs and two outputs.

We compared the offline sum of each PMT signal with the online sum output of the mixer logic. The individual out signal contains a bunch of peaked pulses due to the fast response of the PMT and long time dispersion from diffuse reflection. This makes it difficult to set stable threshold levels. On the other hand, the mixed signal shows good pulse shape and helps to set almost constant thresholds throughout the beam test. The typical pulse shapes of the individual and summed signals are illustrated in Fig.4.

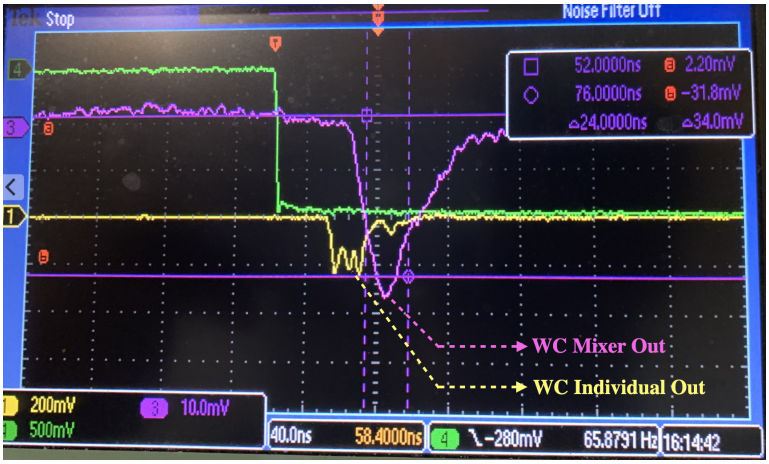

Fig.4. Pulse shapes of the water Cherenkov detector. Individual PMT and the WC mixer signals are indicated by arrows.

3.3 LED Calibration

During the beam test, we calibrated each PMT using a LED light source, driven by a clock generator with a signal width of 25 ns.

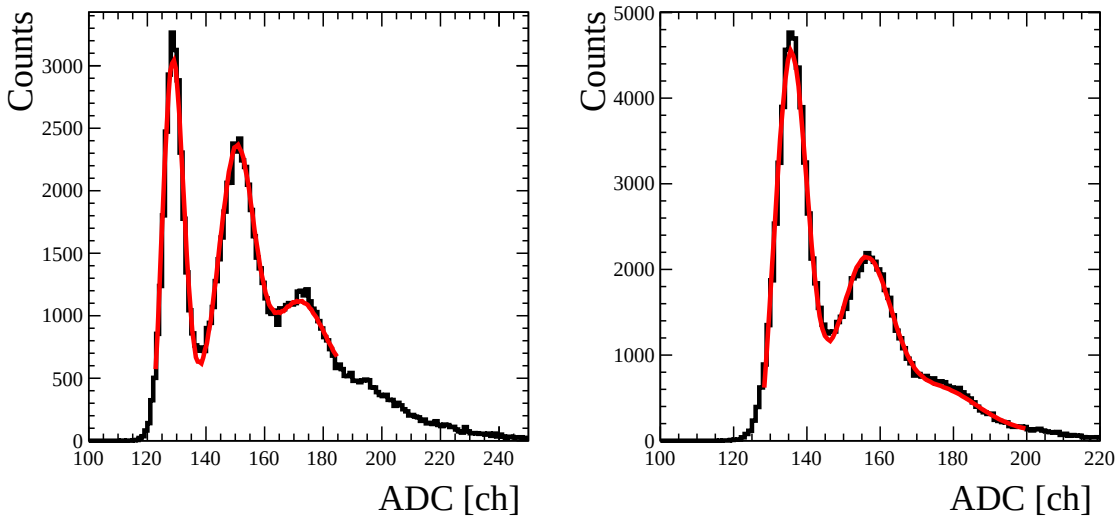

Fig.5. ADC spectra of (left) top and (right) bottom PMTs of the WC using a LED light source.

The measured ADC spectrum is fitted with the single photoelectron response function of the PMT. The fit function describes a convolution of Gaussian distribution for pedestal and photoelectron peaks,

Poisson distribution for Cherenkov photon statistics reaching the PMT, and exponential background distribution [5]. The pedestal position and the PMT gain were deduced from the fit and used for the ADC to $N_{p.e}$ conversion.

§4. Results and Discussion

4.1 Number of photoelectrons

The ADC spectra for two PMTs at both ends were summed and converted to the $N_{p.e}$ distribution using the equation 1.

$$N_{p.e} = \frac{\text{ADC} - \text{Pedestal}}{\text{Gain}} \tag{1}$$

We selected the events leaving hits on the T1 detector. Fig 6 shows an $N_{p.e}$ distribution of the WC when the beam hits the center of the WC. The gain and mean values of the $N_{p.e}$ distribution are summarized in Table 2.

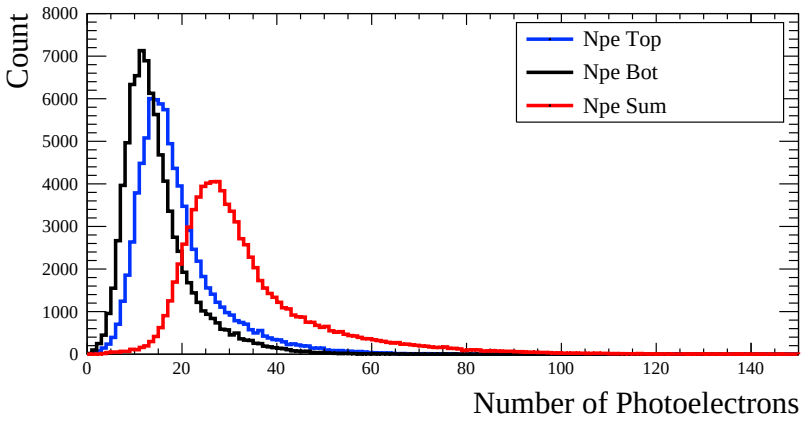

Fig.6. $N_{p.e}$ distributions for individual outputs and their offline sum.

Channel	Gain	Mean $N_{p.e}$
WC Top	22.36 ± 0.09	18.9 ± 0.03
WC Bottom	20.59 ± 0.62	14.8 ± 0.03
WC Sum		33.7 ± 0.05

Table 2. Gain values from the LED calibration in Section 3.3, and mean values of the $N_{p.e}$ distribution using Eq. 1.

The mean value for the summed $N_{p.e}$ distribution was obtained as 33.7. However, The mean value of the top PMT signal is different from that of the bottom PMT signals by approximately 4 photoelectrons. This difference could come from slightly unequal structures between the top and bottom surfaces or, and possibly nonuniform gap difference between the inner and outer vessels. A possible air gap between the PMT and optical acrylic window could also contribute the difference.

4.2 Position Dependence

4.2.1 Horizontal Position Dependence

The beam hit the WC in every 3 cm along the x-axis in the range from $x = -9$ cm to $x = 9$ cm. The measurement results for $N_{p.e}$ along the x-axis are shown in Fig.7. No significant dependence on the x position was observed for both individual and summed signals. Furthermore, the results fit very well with Geant4 optical simulation results.

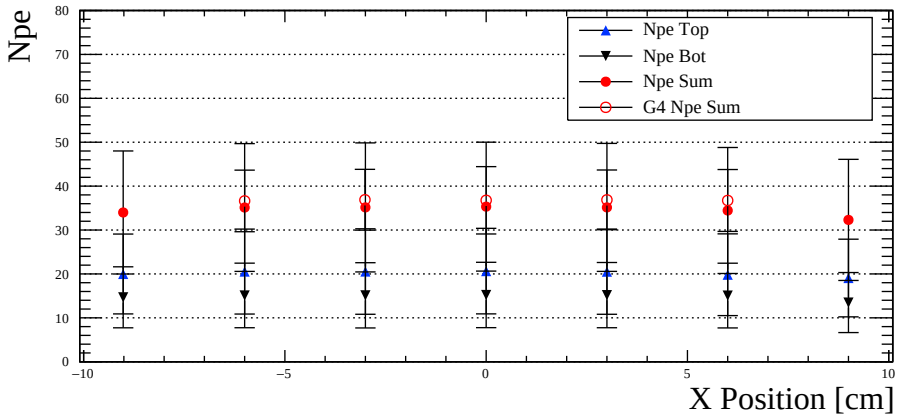

Fig.7. Mean values of $N_{p.e}$ of each channel and their sum along the x-axis

The online output of WC mixer logic is shown in Fig. 8.

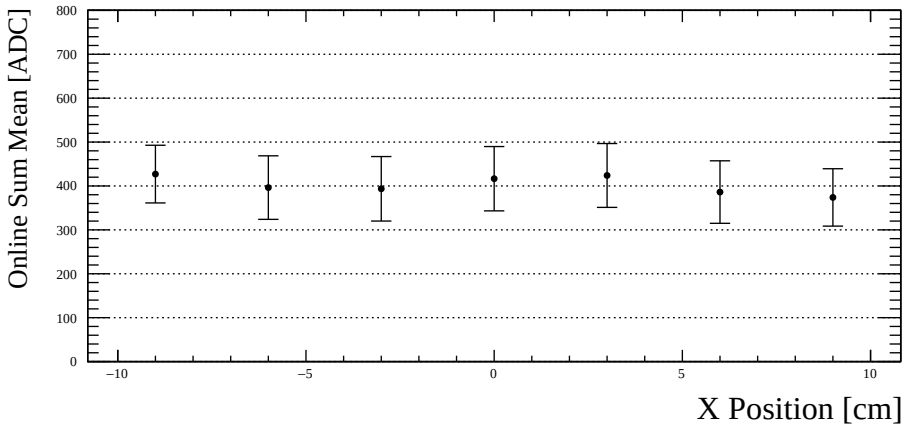

Fig.8. Scanned mean of ADC distribution of WC mixer output along x-axis

It also shows no significant position dependence along the x-axis. The variation in mean ADC values was kept within 10%, referenced to the value for the beam position hitting the center.

4.2.2 Vertical Position Dependence

We also measured the y position dependence in every 10 cm steps, from the center to $y = 80$ cm. To confirm the reliability of the measurement, we also took the data at $y = -30$ cm and $y = -60$ cm. The

results of the offline and online analysis are shown in Fig.9 and Fig.10.

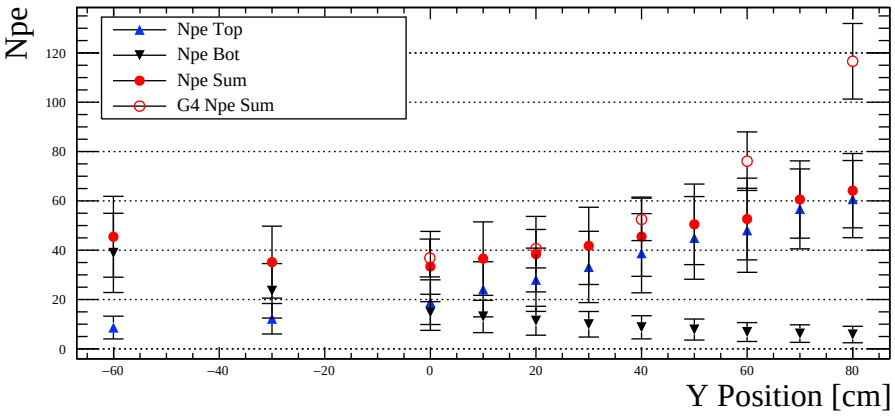

Fig.9. Mean values of $N_{p.e}$ of individual channels and their sum along the y-axis.

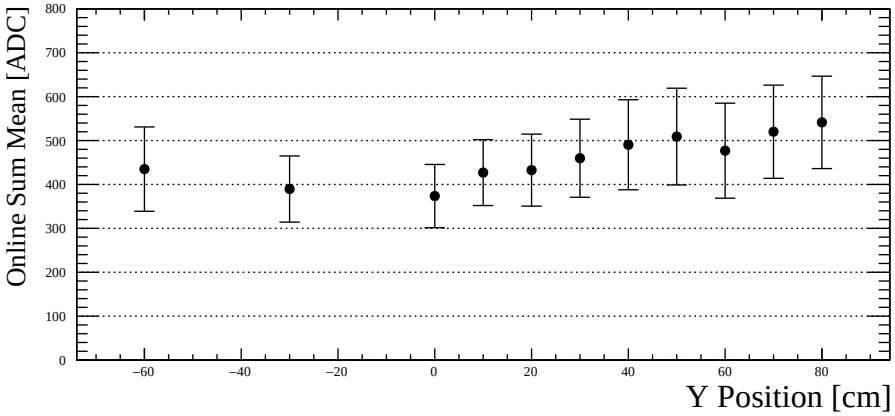

Fig.10. Mean values of the ADC distribution of the WC mixer output along the y-axis

While a large change is predicted in the output along y-axis, the measurement results show no such a large position dependence.

4.3 Incident Angle Dependence

We measured the signals in every 20 cm steps from $y = 0$ to 80 cm at the incident angle $y' = 15°$.

The measured results are compared with the $y = 0°$ results. In the central region for $y < 40$ cm, the WC mixer outputs are almost identical at the angles of $0°$ and $15°$.

4.4 Linearity

The online sum signal of the WC mixer logic was found to be linearly proportional to the summed value of the two PMT ouputs obtained in offline analysis, which verified the performance of WC mixer

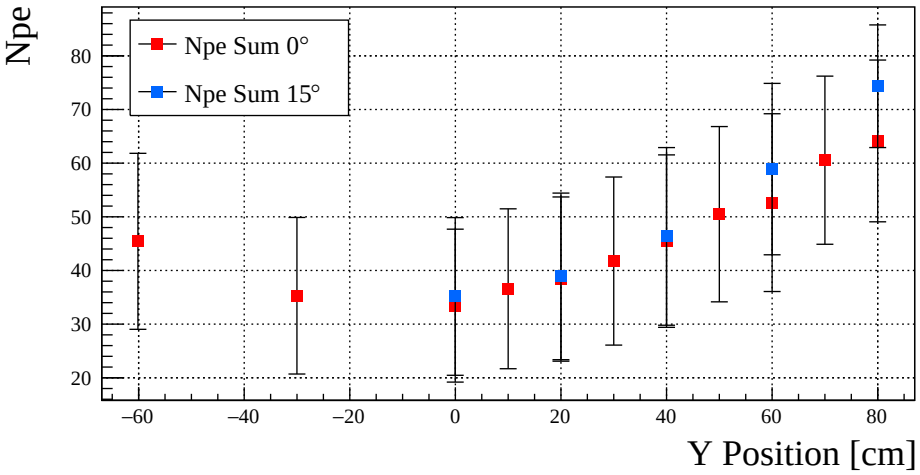

Fig.11. Measured numbers of photoelectrons along the y-axis when the beam is incident at (red) 0° and (blue) 15°.

logic for the online trigger. Fig.12 represents a correlation between online mixer and offline sum signals. The scatter data were fitted with a straight line.

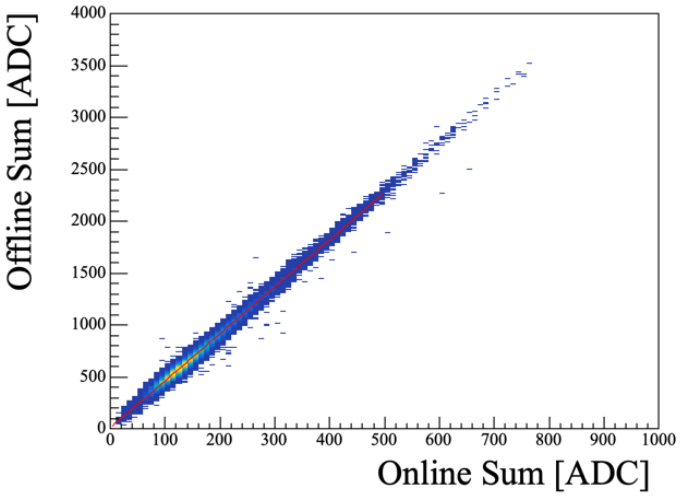

Fig.12. Scatter plot of the offline sum and online mixer signals.

§5. Conclusion

We have constructed a Water Cherenkov detector for the H-dibaryon search experiment (E42) at J-PARC. The WC was designed to suppress low-momentum proton-associated triggers. We commissioned a WC module using 460-MeV positrons at ELPH. We measured the individual photomultiplier signals at both ends of the WC module and the summed signal. The number of photoelectrons was obtained as 33.7 ± 0.05 with a custom-made signal mixer. The summed signal was found to decrease the position and angular dependences of the WC output, thereby providing stable online trigger.

Acknowledgment

We greatly appreciate to the staff of ELPH for their extensive support and stable beam operation.

References

[1] J.K. Ahn, K. Imai: J-PARC Proposal E42, Search for the H-dibaryon with a large acceptance hyperon spectrometer; J.K. Ahn, Few-Body Syst. 54 (2013) 387390; J.K. Ahn, JPS Conf. Proc. 17 (2017) 031004; J.K. Ahn, Proc. Sci. (2018) 124, Hadron 2017.

[2] J.K. Ahn, et al., IEEE Trans. Appl. Supercond. 26 (2016) 4002105.

[3] S.H. Kim *et al.*: Nucl. Instrum. Meth.A 940 (2019) 359-370.

[4] T. Gogami *et al.*: Nucl. Instrum. Meth.A 817 (2016) 70-84.

[5] E.H. Bellamy *et al.*: Nucl. Instrum. Meth.A 339 (1994) 468-476.

(ELPH Experiment : #2887)

Three-dimensional phantom production for a multiple-isotope PET

Tomonori Fukuchi[1], Hiromitsu Haba[2], and Hideki Kikunaga[3]

[1]*RIKEN Center for Biosystems Dynamics Research, Kobe, 650-0047*

[2]*RIKEN Nishina Center for Accelerator-Based Science, Wako, 351-0198*

[3]*Research Center for Electron Photon Science, Tohoku University, Sendai, 982-0826*

We have been developing a new type of positron emission tomography (PET), which can detect the prompt γ-ray with the positron-electron annihilation photons, for multiple-tracer imaging. To evaluate the performances of the developing system, we produced a three-dimensional imaging phantom using the photonuclear reaction of ^{nat}Ti(γ,*xn*)^{44}Ti. We performed an imaging experiment with the produced ^{44}Ti phantom using the developing PET system and succeeded in reconstructing three-dimensional image of phantom.

§1. Introduction

Positron emission tomography (PET) imaging is widely used for various objects to obtain a three-dimensional distribution of positron emitting radioisotopes. A conventional PET imaging system cannot identify tracer nuclide, because of the constant energies of positron-electron annihilation photons. Accordingly, we have been developing a new type of PET system, which can identify the tracer nuclide by detecting coincidence γ-ray with annihilation photons [1].

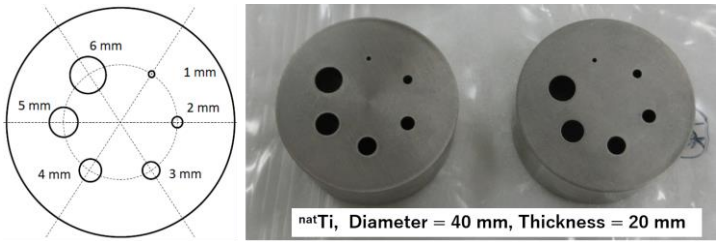

Fig. 1. Configuration and photograph of Ti targets for three-dimensional imaging phantoms.

In order to evaluate the performances of the developing PET system, it is necessary to perform the phantom imaging, which visualize the known radio-tracer distributions. Therefore, we produced a three-dimensional radio-active phantom of ^{44}Ti, which is a long-lived parent nuclide of a positron-γ emitter ^{44}Sc, using the photonuclear reaction.

§2. Three-dimensional phantom production

To produce the three-dimensional phantoms, we prepared ^{nat}Ti targets, which have cylindrical shape with 40-mm in diameters and 20-mm thicknesses with cylindrical holes. Figure 1 shows a configuration and photograph of the

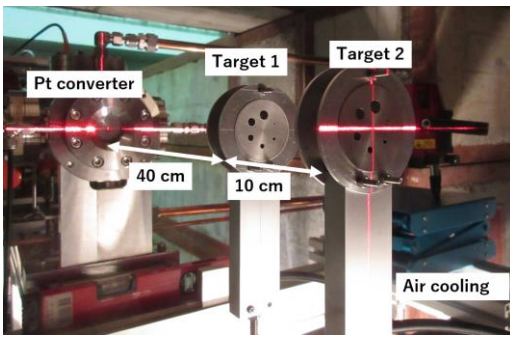

Fig. 2. Target setup for the ^{44}Ti phantom production.

targets. The target setup for the photon irradiation is shown in Fig. 2. The high-energy photon irradiation was performed for 7 hours by the ELPH accelerator with an electron energy of 55.5 MeV, and ^{44}Ti was produced in the ^{nat}Ti(γ, *xn*)^{44}Ti reactions (nat: natural isotopic abundance). Titanium-44 decays into ^{44}Sc with a half-life of 59.1 years, and ^{44}Sc is a positron-γ emitter (γ-ray energy: 1157 keV) with a half-life of 3.85 hours [2]. Although the most of short-lived by-products were attenuated for a few days after the irradiation ^{46}Sc ($T_{1/2}$ = 83.79 days) remaied with ^{44}Ti. The phantom radio-activities of ^{44}Ti and ^{46}Sc in 600 days after production were determined by a HPGe detector as summarized in Table 1.

Table 1. Phantom radio-activities in 600 days after the irradiation.

	Phantom-1	Phantom-2
^{44}Ti	1.25 kBq	0.70 kBq
^{46}Sc	84.8 kBq	48.1 kBq

§3. Imaging experiment

To investigate the performance of multiple-isotope PET system, a 24-hours measurement using the ^{44}Ti phantom (phantom-1) was performed as shown in Fig. 3. From the annihilation photons and the prompt γ-ray coincidence data, three-dimensional phantom image was reconstructed as shown in Fig. 3. Using the ^{44}Ti phantoms, we will perform further experiments for the multiple-isotope imaging in the future.

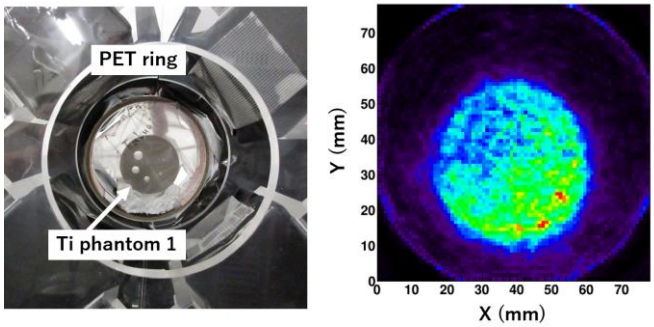

Fig. 3. Photograph of measurement of ^{44}Ti phantom (phantom-1) and reconstructed image.

Acknowledgments

The authors thank to the facility staffs of ELPH in Tohoku University for supplying the high-quality electron beam. This work was supported by JSPS KAKENHI Grant Number JP15H04770

References

[1] T. Fukuchi *et al.*: Med. Phys. **44(6)** (2017) 2257.

[2] National Nuclear Data Center, Brookhaven National Laboratory, http://www.nndc.bnl.gov/.

(ELPH Experiment : #2886, #2907)

RI Production for the synthesis of Promethium Endohedral Metallofullerenes by Photon Activation Method II

K. Akiyama[1], T. Suwa[1], H. Sugiyama[1], S. Kubuki[1], and H. Kikunaga[2]

[1]*Department of Chemistry, Tokyo Metropolitan University, Hachioji, 192.0397*
[2]*Research Center for Electron Photon Science, Tohoku University, Sendai, 982-0826*

To study the stability of $\mathbf{M_2@C_{80}}$ type metallofullerene including **Pm**, the extraction rate of $\mathbf{M_2@C_{80}}$ for **Pm** were investigated for the conventional method and newly developed anaerobic extraction method using TEA/Acetone mixed solvent. Comparison with the conventional method, the extraction rate for TEA/Acetone is found to be about 3 times larger than that for $\mathbf{CS_2}$ solution of the conventional method. These results show that the $\mathbf{M_2@C_{80}}$ for **Pm** is possible to be anaerobic species and that the newly developed method is effective for the extraction of anaerobic metallofullerene species.

§1. Introduction

Endohedral metallofullerenes (EMFs) are known as a clathrate compound and are attracting interest of the expectation for the potential application brought from their unique physical and chemical properties. The large number of studies about the EMFs have been reported, so far. Especially for the EMFs of lanthanide, it has been studied for a variety of encapsulated elements from the dawn of metallofullerene research. However, only metallofullerene of promethium (**Pm**) has been still missing [1]. It is well known that **Pm** is one of the artificial elements belonging to lanthanide elements and do not have any naturally occurred stable isotope. The chemical property of **Pm** is considered to be almost same as those of other neighboring lanthanides, actually most stable oxidation state in water is +3 similar to neighboring element of **Nd**. In general, **Pm** is produced from processing nuclear fuel and neutron irradiation of **Nd** in High Flux Isotope Reactor. However, ^{147}**Pm** produced by these methods is not suitable for the metallofullerene research because of their small γ-ray emission rate and their long half life.

Recently, we reported the production of **Pm** EMFs using ^{143}**Pm** produced by photon activation of natural samarium and also reported that their properties such as oxidation state of **Pm** in fullerene cage and that the major species of **Pm** metallofullerenes were found to be $\mathbf{Pm@C_{82}}$ [2]. On the other hand, the chemical properities of the minor **Pm** metallofullerenes species, such as $\mathbf{M_2@C_{80}}$, were still not investigated.

It is well known that the one of the most famous minor EMF species is $\mathbf{M_2@C_{80}}$ and that this EMF species is second major among those encapsulating light lanthanide elements [1]. However, it has been found that the chemical stability of this EMF species with neutral charge is decreased with incresing of atomic number while that for the anion species is increased [3]. It is possible that Pm may form a stable $\mathbf{M_2@C_{80}}$ fullerene with the highest atomic number among the light lanthanoid.

Although it is impossible to discuss directly about the stability of $\mathbf{M_2@C_{80}}$ with homogeneously encapsulating two promethium atom from experimental data due to the trace amount of Pm,we could disucuss about that of $\mathbf{M_2@C_{80}}$ with heterogeneously encapsulating Pm and another lanthanide atom added as a carrier. Here, we report the results of HPLC analysis of **Pm** EMFs produced by conventional method and also report the quantitative results extracted by newly developed anaerobic fullerene recovery system.

§2. Experimental

2.1 Synthesis of Soot Containig Promethium Endhedral Metallofullerenes

About 1.0 **g** of **Sm** oxide were wrapped by **Al** foil and sealed into quartz tubes. These targets were irradiated by 50 **MeV** photon at Research Center for Electron Photon Science in Tohoku University. Chemically purified ^{143}**Pm** from **Sm** target by prevously reported method [4] was employed for the metallofullerene production. These **Pm** tracer were dissolved into concentrated nitric acid together with about 0.5 **g** of $\mathbf{La_2O_3}$ as a carrier and ^{139}**Ce** radiotracer as a conparator. This solution was heat to dryness and then EtOH was added for dissolving resultant nitrate salts. This EtOH solution was dropped on a porous carbon rod with 10 **mm** diameters and 60 **mm** length to adsorb the nitrate salts and then dried. This porous carbon rod was placed in an electric tubular furnace and sintered at 700 ^{o}**C** under $\mathbf{N_2}$ gas flow. After the sintering, this rod was set into the fullerene generator as an anode for the arc discharge. The promethium EMFs were produced by the arc discharge method [2] with DC 100 **A** under 60 **kPa** of He atmosphere.

2.2 Conventional fullerene extraction method

The produced soot containing **Pm** EMFs was dissolved to $\mathbf{CS_2}$ and then filtered to remove insoluble substance. After filtration, $\mathbf{TiCl_4}$ was added in this solution for the pre-separation of EMFs [6]. This pre-separated EMFs solution was evaporated to dryness and then toluene was added to dissolve fullerene species for the HPLC analysis.

2.3 Anaerobic fullerene recovery system

The soot produced by above mentioned method dissolved to $\mathbf{CS_2}$ were recovered from the fullerene generator by washing the inner wall of this generator. These recovered $\mathbf{CS_2}$ solution were introduced into a glass vessel shown in the figure 1. The $\mathbf{CS_2}$ in the vessel is dried in vacuo and then $\mathbf{N_2}$ gas was introduced into the vessel for replacement to $\mathbf{N_2}$ atmosphere. About 280 **mL** of tetraethylamine/acetone (1 : 3) mixed solution (here after TEA/Acetone) was injected into the vessel from branch sealed with a septum by use of a syringe. This TEA/Acetone solution was refluxed for 8 hours to extract chemically reduced anaerobic metallofullerene species. After the reflux, this solution was filtered to remove insoluble substances such as amorphous carbon. The remained soot on the filter were rinsed by $\mathbf{CS_2}$ to recover remained fullerene species. The γ ray emitted from these solutions were measured by a Ge detector for the quantitative determination.

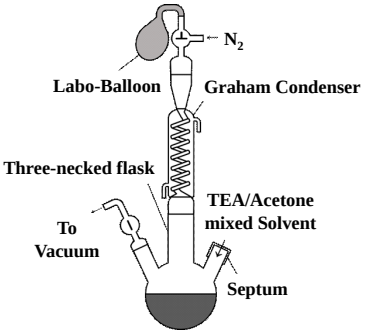

Fig.1. Schematic diagram of a glass vessel for anaerobic extraction of a reduced metallofullerene.

§3. Results and Discussion

3.1 Ectraction of $M_2@C_{80}$ type Pm metallofullerene by Conventional Method

The HPLC retention time of $\mathbf{M_2@C_{80}}$ for La on our Buckyprep column used for HPLC analysis is around 80 minute. The radioactivity of ^{139}**Ce** is observed at HPLC fraction of 81 to 86 minute but not observed other fraction in 75-92 minute. This observed radioactivity is considered due to $\mathbf{M_2@C_{80}}$ species containig ^{139}**Ce** becasue HPLC retention time of these fractions were almost same as that of $\mathbf{M_2@C_{80}}$ for La. On the other hand, observed radioactivity of ^{143}**Pm** is found in the HPLC fraction of 86 to 91 minute and not observed in the HPLC fraction of 81 to 86 minute shown in figure 2. These results suggest that $\mathbf{M_2@C_{80}}$ including ^{143}**Pm** is not stable in the air and not easily extracted by the conventional method.

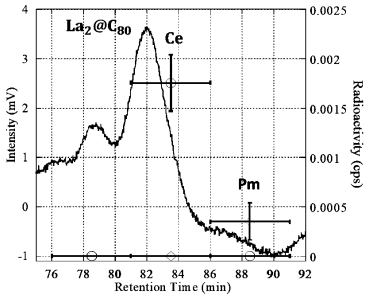

Fig.2. HPLC profile around the retention time of $\mathbf{M_2@C_{80}}$.

3.2 Extraction of $M_2@C_{80}$ type Pm metallofullerene by anaerobic Method

From the results of previous subsection, it is found that it is difficult to extract metallofullerene species which is not stable in the air by the conventional fullerene extraction method because this method exposes metallofullerene species to the air. For the extraction of anaerobic metallofullerene, we tried to develop the anaerobic extraction method for radioactive metallofullerenes. As shown in figure 3, the differences in the extraction process between conventional method and anaerobic method are the insertion of the process using glass vessel shown in figure 1 for the replacement of solvent to TEA/acetone and the reflux in this solvent before the filtration. The ratio of radioactivity in finally obtained solution

to radioactivity used for metallofullerene production is defined as the extraction rate and these rate are indicated in the table 1. The numerical notations given for finaly obtained each solvent sample in the figure 3 correspond to the number indicated in table 1. Comparing these values, it was found that the extraction rate of ^{143}**Pm** metallofullerene in the TEA/acetone solution was about 3 times larger than that of the conventional method. These results show that the $\mathbf{M_2@C_{80}}$ for **Pm** is possible to be anaerobic species and that the newly developed method is effective for the extraction of anaerobic metallofullerene species.

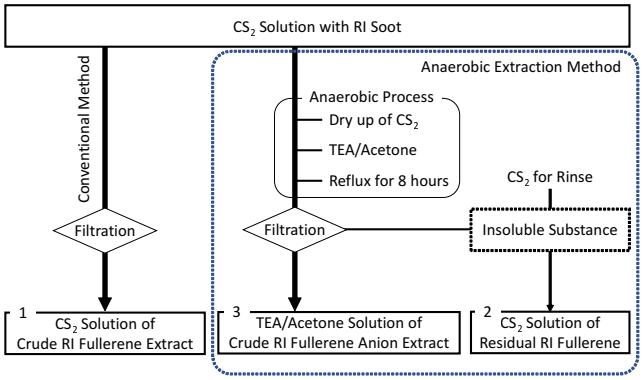

Fig.3. Comparison of conventional method with newly developed anaerobic extraction method.

Table 1. Extraction rate of Pm and Ce metallofullerenes

No.	Extracted in	^{143}**Pm**	^{139}**Ce**
1	$\mathbf{CS_2}$ (Conventional)	0.018 %	0.047 %
2	$\mathbf{CS_2}$ (Anaerobic)	0.016 %	0.0056 %
3	TEA/Acetone (Anaerobic)	0.060 %	0.057 %

Acknowledgment

We deeply thank to the facility staffs of research center for electron photon science at Tohoku University for supplying the high-quality electron beam. And also we thank to Doctor Kyo Tsukada for helping us in the sample irradiation.

References

[1] H. Shinohara: Rep. Prog. Phys. **63** (2000) 843.
[2] K. Akiyama *et al.*: ELPH Annual Rep. (2014) 135.
[3] A. Velloth *et al.*: J. Phys. Chem. C **121** (2017) 18169.
[4] K. Akiyama *et al.*: ELPH Annual Rep. (2015) 112.
[5] K. Akiyama *et al.*: ELPH Annual Rep. (2016) 72.
[6] K. Akiyama *et al.*: ELPH Annual Rep. (2016) 72.

(ELPH Experiment : #2935)

Development of novel silicon sensors with high time and spatial resolution

Taikan Suehara[1], Yuto Deguchi[2], Yuto Uesugi[2], Yu Kato[3], and Ryo Yonamine[4]

[1]*Department of Physics, Faculty of Science, Kyushu University, Fukuoka, 819-0395*
[2]*Department of Physics, Graduate School of Science, Kyushu University, Fukuoka, 819-0395*
[3]*Department of Physics, Graduate School of Science, The University of Tokyo, Tokyo, 113-0033*
[4]*Department of Physics, Graduate School of Science, Tohoku University, Sendai, 980-8578*

Silicon pad sensors with novel functions of higher timing resolution (LGAD: Low Gain Avalanche Detector) and higher position resolution (PSD: Position Sensitive Detector) are studied for an application to Silicon-Tungsten electromagnetic calorimeter for a detector of the International Linear Collider (ILC). Prototype sensors are fabricated, equipped with dedicated ASICs (Application-Specific Integrated Circuits) and tested with a positron beam as well as a radioisotope. The first results of the measurements of timing resolution with LGADs and position reconstruction with PSDs are reported.

§1. Introduction

The International Linear Collider (ILC) is a future electron-positron collider for precise measurements of Higgs bosons and various BSM searches. Silicon-tungsten electromagnetic calorimeter (SiW-ECAL) is one of the candidates to be used in the International Large Detector (ILD) [1], one of the detector concepts for the ILC. We are proposing two types of new silicon sensors, Low Gain Avalanche Detectors (LGADs) and Position Sensitive Detectors (PSDs) to be replaced to the standard silicon pads of SiW-ECAL. LGADs are possible to obtain precise timing information and PSDs are sensitive to hit positions within a cell. With LGADs and PSDs position and timing resolution of the SiW-ECAL can be significantly improved, which should proceed further reach of Higgs and BSMs in the ILC physics program.

LGADs are silicon sensors with the internal avalanche amplification, which have already been proved to realize the timing resolution down to 30 psec [2]. The precise timing information can be primarily utilized to perform particle identification of hadrons by Time-of-Flight (ToF) method, which can be combined with dE/dx information obtained in the Time Projection Chamber, which is the main tracking detector in the ILD.

PSDs are silicon sensors with each cell having an electrode at each corner instead of a simple pad spread over the cell. When the signal charge reaches P^+ pad, the charge is resistively split to electrodes via a resistive layer on the surface. The hit position is reconstructed as the gravity center of signal strengths of the electrodes at the four corners. In contrast to using smaller cells, the position resolution can be improved with minimal increase of the readout channels if we replace the silicon pads with PSDs

in SiW-ECAL.

We prepared samples for both LGADs and PSDs to demonstrate the possibilities to be used for SiW-ECAL and to measure characteristics of the sensors for the optimization. We have conducted measurements with the positron beam provided from ELPH as well as particles from radioisotopes.

§2. Setup of the test beam

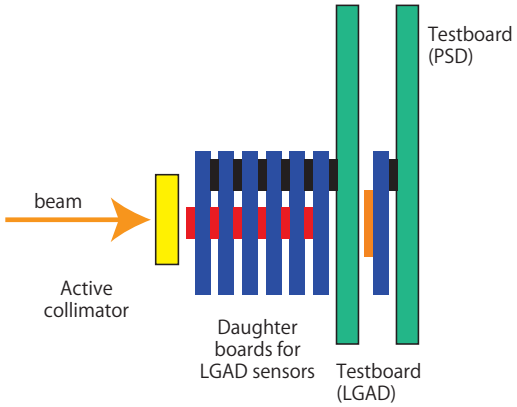

Fig.1. Overview of the setup of LGAD/PSD measurement. The positron beam penetrates up to 6 LGADs and a PSD to obtain concurrent signal.

Figure 1 shows the overview of the setup. The LGADs and PSDs are equipped with testboards of Skiroc2-CMS ASIC (Application-Specific Integrated Circuit). Skiroc2-CMS has 64-channel readout for silicon sensors with precise charge and timing information. The timing jitter is $\sim$30 psec with charge of $>$ 150 fC with dynamic range of ADC $>$ 1000 fC. The timing information is obtained via clock count of 40 MHz and analog 12-bit Time-of-Arrival (ToA), which clips the voltage sweeping within a clock. The non-linearity of ToA and time walk are corrected using measurements with charge injection.

Up to 6 LGADs were stacked with single testboard to obtain correlation of the signal from penetrating beam. The testboards with LGADs and PSDs were synchronized with a common-stop signal. Self-triggering with LGADs were used for the common stop. An active collimator, which is a plastic scintillator with a center hole, placed in front of the sensor stack. The optical readout of the collimator is done by PMT, connected to a remaining channel of the testboard.

§3. Results with the LGADs

The sensors we have tested at the beam is listed in Table 1 [3]. Some sensors are designed as Avalanche Photo-Diodes (APDs) which are used for optical photon measurements with avalanche gain. We recognized those as prototype of LGADs since the basic structure is the same. There are also prototypes of LGADs developed in Hamamatsu (pkg-10 and pkg-20) which were also tested with beam. There are two types of LGADs/APDs, reach-through type and inverse type. The reach-through type has proven performance of timing resolution, but since the amplification region is confined below the readout pads, there is significant inactive area. In contrast, the inverse type has amplification on the bottom of the

Table 1. List of LGADs and APDs tested with beam at ELPH, Tohoku University.

Spec No.	Type	Size	Count #1	Count #2	Count #1&#2	Efficiency
S12023-10A	Reach-through	ϕ1	1002	965	147	14.9%
S2384	Reach-through	ϕ3	4355	5796	1136	22.4%
S8664-10K	Inverse	ϕ1	613	298	4	0.9%
S8664-20K	Inverse	ϕ2	368	185	2	0.7%
S8664-55	Inverse	5×5	3060	2327	96	3.6%
pkg-10	Reach-through	ϕ1	1687	1584	15	0.9%
pkg-20	Reach-through	ϕ1	1956	3010	219	8.8%

sensor, which should result in more uniform response over the surface.

The Table 1 also shows the number of single and coincidence counts with the beam injection. The sensors are placed to be penetrated by the beam, but we have no selection of the angle of the beam so some fraction of the particles can geometrically hit only one sensor, depending on the sensor size. From the table we see coincidence ratio of the inverse APDs are significantly smaller than the reach-through APDs. The possible reason is hit-by-hit fractuation of the gain at the inverse-type APDs, but more investigation is necessary to confirm this.

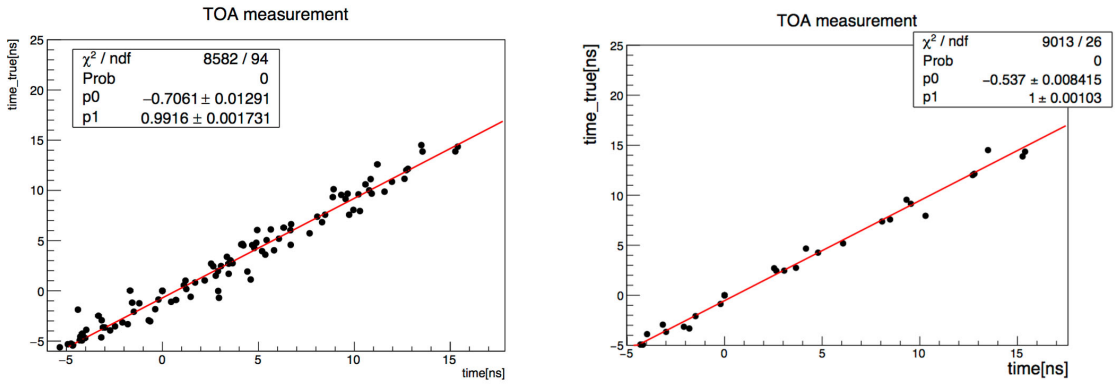

Fig.2. Timing correlation of two APDs (S2384) without selection (left) and with selection of $>$ 100 fC (right).

Timing resolution of reach-through APDs (S2384) were measured with the ToA data of the coincidence events. After the correction of non-linearity and time-walk of the ToA, we see clear correlation between two sensors as shown in Figure 2 (left). Figure 2 (right) shows the correlation of events having $>$ 100 fC of charge to avoid jitter of the electronics. The timing resolution of single sensor was calculated as 385 $\pm$ 94 psec. The result is worse than expected. Possible reason is imperfect correction of ToA since the correction coefficients are obtained with measurements at different places. We will investigate this with further measurements.

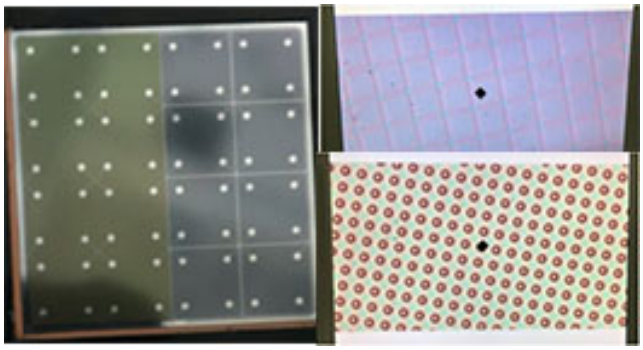

Fig.3. Picture of a PSD (left) and magnified view of resistive P^+ surface (top-right, left-half of the PSD) and resistive layer surface (bottom-right, right-half of the PSD).

§4. Results with the PSDs

We fabricated a few types of PSDs having 4×4 cells, shown in Figure 3. Each cell has an electrode at each corner, having 64 readout channels in total. One of the important parameters of the PSDs is the surface resistance. The PSDs have two types of the resistive layer in each side. One is a resistive P^+ surface, which forms meshes to increase the resistivity. The other is a dedicated resistive layer connected to a dotted P^+ layer, which gives 10-30 times more resistance [4]. The resistivity of the edges of the PSDs is set lower to reduce position distortion. The cell size is 5.5×5.5 mm^2, and the sensor thickness is 650 μm for all the sensors.

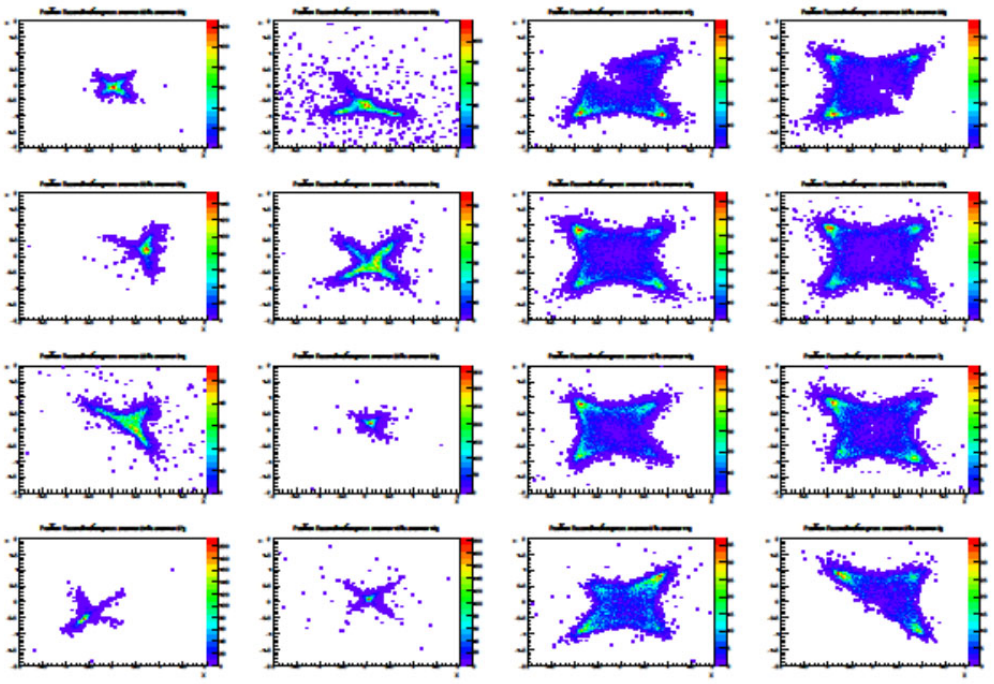

Fig.4. Reconstructed position of each cell with a PSD, with beta radiation from ^{90}Sr.

Figure 4 shows the response of the PSD sensors with a ^{90}Sr radioactive source. The position is

calculated by

$$\boldsymbol{X}_{\rm rec} = \frac{(\mathrm{Q}_0 + \mathrm{Q}_1) - (\mathrm{Q}_2 + \mathrm{Q}_3)}{\mathrm{Q}_0 + \mathrm{Q}_1 + \mathrm{Q}_2 + \mathrm{Q}_3}$$
$$\boldsymbol{Y}_{\rm rec} = \frac{(\mathrm{Q}_0 + \mathrm{Q}_2) - (\mathrm{Q}_1 + \mathrm{Q}_3)}{\mathrm{Q}_0 + \mathrm{Q}_1 + \mathrm{Q}_2 + \mathrm{Q}_3}$$

where $\boldsymbol{X}_{\rm rec}$ and $\boldsymbol{Y}_{\rm rec}$ are the reconstruction position in $\boldsymbol{X}$ and $\boldsymbol{Y}$ axes and $\boldsymbol{Q_i}$ is measured charge at each electrode on the corner. The difference between maximum and minimum $\boldsymbol{X}_{\rm rec}$ ($\boldsymbol{Y}_{\rm rec}$), called "dynamic range" should be -1 to 1 in an ideal case. The figure shows almost maximum dynamic range is obtained with the resistive layer (right side of the figure). The concentration of the events at $\boldsymbol{X}_{\rm rec} = \boldsymbol{Y}_{\rm rec} = \pm 1$ is because of a threshold effect of the trigger on single channel instead of sum of four channels in a same cell, due to the limitation of the electronics.

The PSDs were also irradiated with positron beam, but due to higher environmental noise at beam line it is difficult to reconstruct positions with the obtained results. Further studies are expected with more appropriate electronics and shielding.

§5. Summary

LGADs/APDs and PSDs sensors have been studied for the application to ILD SiW-ECAL. The first measurement of the timing resolution of the APDs with positron beam is obtained as 385 ± 94 psec, which we will try to improve with updated setup. We successfully reconstructed the hit positions on PSDs with good dynamic range using a ^{90}Sr radioactive source. Further studies with positron beam are planned.

Acknowledgments

The test beam experiment was conducted with the support of ELPH, Tohoku University. We appreciate Omega group for the support on the operation of the Skiroc2-CMS chip. This work is partially supported by JSPS KAKENHI Grant Number JP17H05407.

References

[1] T. Behnke, James E. Brau, Philip N. Burrows, M. Peskin, *et al.*, The International Linear Collider Technical Design Report - Volume 4: Detectors, arXiv:1306.6329 (2013).

[2] McCarthy, Thomas G., Upgrade of the ATLAS Liquid Argon Calorimeters for the High-Luminosity LHC, arXiv:1612.07102 (2016).

[3] Y. Deguchi, K. Kawagoe, E. Mestre, R. Mori, T. Suehara, T. Yoshioka, Study of silicon sensors for precise timing measurement, 2020 JINST **15** C05051.

[4] Y. Uesugi, R. Mori, H. Yamashiro, T. Suehara, T. Yoshioka, K. Kawagoe, Study of Position Sensitive Silicon Detector (PSD) for SiW-ECAL at ILC, 2020 JINST **15** C05033.

(ELPH Experiment : #2623, #2640, #2655, #2694, #2710)

Coherent photoproduction of the neutral pion and eta meson on the deuteron

T. Ishikawa[1], H. Fujimura[1*], H. Fukasawa[1], R. Hashimoto[1†], Q. He[1‡], Y. Honda[1], T. Iwata[2], S. Kaida[1], J. Kasagi[1], A. Kawano[4], S. Kuwasaki[1], K. Maeda[3], S. Masumoto[5], M. Miyabe[1], F. Miyahara[1§], K. Mochizuki[1], N. Muramatsu[1], A. Nakamura[1], K. Nawa[1], S. Ogushi[1], Y. Okada[1], K. Okamura[1], Y. Onodera[1], K. Ozawa[6], Y. Sakamoto[4], M. Sato[1], H. Shimizu[1], H. Sugai[1¶], K. Suzuki[1‖], Y. Tajima[2], S. Takahashi[1], Y. Taniguchi[1], Y. Tsuchikawa[1**], H. Yamazaki[1††], R. Yamazaki[1], and H.Y. Yoshida[2]

[1]*Research Center for Electron Photon Science (ELPH), Tohoku University, Sendai 982-0826, Japan*
[2]*Department of Physics, Yamagata University, Yamagata 990-8560, Japan*
[3]*Department of Physics, Tohoku University, Sendai 980-8578, Japan*
[4]*Department of Information Science, Tohoku Gakuin University, Sendai 981-3193, Japan*
[5]*Department of Physics, University of Tokyo, Tokyo 113-0033, Japan*
[6]*Institute of Particle and Nuclear Studies, High Energy Accelerator Research Organization (KEK), Tsukuba 305-0801, Japan*

Coherent photoproduction of the neutral pion (π^0) and eta meson (η) on the deuteron (d), $\gamma d \to \pi^0 \eta d$, has been experimentally studied at incident photon energies ranging from the reaction threshold to 1.15 GeV. The total cross section as a function of the incident energy is higher than the existing theoretical calculation without any final-state interaction (FSI) based on quasi-free $\pi^0\eta$ photoproduction on the nucleon (N) with deuteron coalescence. The calculation reproduces the data below 1 GeV including FSIs (meson scattering and absorption of an additionally produced meson on the spectator nucleon, and many-body interaction of mesons with the final-state deuteron). We have measured the differential

*Present address: Department of Physics, Wakayama Medical University, Wakayama 641-8509, Japan
†Present address: Institute of Materials Structure Science (IMSS), High Energy Accelerator Research Organization (KEK), Tsukuba 305-0801, Japan
‡Present address: Department of Nuclear Science and Engineering, Nanjing University of Aeronautics and Astronautics (NUAA), Nanjing 210016, China
§Present address: Accelerator Laboratory, High Energy Accelerator Research Organization (KEK), Tsukuba 305-0801, Japan
¶Present address: Gunma University Initiative for Advanced Research (GIAR), Maebashi 371-8511, Japan
‖Present address: The Wakasa Wan Energy Research Center, Tsuruga 914-0192, Japan
**Present address: J-PARC Center, Japan Atomic Energy Agency (JAEA), Tokai 319-1195, Japan
††Present address: Radiation Science Center, High Energy Accelerator Research Organization (KEK), Tokai 319-1195, Japan

cross sections $d\sigma/dM_{\pi\eta}$, $d\sigma/dM_{\pi d}$, $d\sigma/dM_{\eta d}$, and $d\sigma/d\Omega_d$ in the γd center-of-mass frame for the first time. The measured angular distributions of deuteron emission do not show strongly backward-peaking behavior predicted by the calculation, as well as that in the $\gamma d \to \pi^0\pi^0 d$ reaction. This suggests a different reaction mechanism from the calculations, and a possible mechanism would be a sequential reaction $\gamma d \to \mathcal{D}_{\rm IV} \to \pi^0\mathcal{D}_{\rm IS} \to \pi^0\eta d$ and/or $\gamma d \to \mathcal{D}_{\rm IV} \to \eta\mathcal{D}_{\rm IV} \to \pi^0\eta d$ with an isoscalar dibaryon $\mathcal{D}_{\rm IS}$ and an isovector dibaryon $\mathcal{D}_{\rm IV}$. At the highest incident energy, an enhancement is observed near the ηd threshold. The spin-parity of this state is found to be 1^-, which corresponds to an S-wave ηd and/or S-wave $N(940)1/2^+$ and $N(1535)1/2^-$.

§1. Introduction

Coherent simultaneous photoproduction of the neutral pion (π^0) and eta meson (η) on the deuteron $\gamma d \to \pi^0\eta d$ has a unique feature for studying properties of hadron structures and interactions. Owing to absence of a Δ-Kroll-Ruderman term and a meson-pole term, a minor effects can be observed such as distortion of cross sections by the final-state interactions (FSIs), and sequential dibaryon production in the intermediate states.

§2. Experiment

Meson photoproduction experiments with an electromagnetic calorimeter complex FOREST [1] were carried out from May 2008 to May 2010 at the Research Center for Electron Photon Science (ELPH), Tohoku University, Japan [2]. Bremsstrahlung photons were used from the circulating 1.2-GeV electrons in the STretcher booster (STB) ring [3]. The photon energy was tagged with a photon tagging counter STB-Tagger II [4]. The energies of the tagged photon beam ranged from 740 to 1150 MeV. The final-state particles were detected with the FOREST detector. The trigger condition of the DAQ system was made for detecting more than one final-state particle coincident with a photon-tagging signal. In the analysis stage , the events containing four neutral particles and a charged particle were selected. The $\gamma d \to \pi^0\eta d$ event selection was made finally by applying a kinematic fit with six constraints: the energy and three-momentum conservation, the invariant mass of two photons out of four being the π^0 mass, and the invariant mass of the other two photons being the η mass.

§3. Cross sections

The total and differential cross sections were measured for the $\gamma d \to \pi^0\eta d$ reaction at the incident energy ranging from the reaction threshold to 1.15 GeV. The analysis of the $\gamma d \to \pi^0\eta d$ reaction was similar to that of the $\gamma d \to \pi^0\pi^0 d$ reaction described in Ref. [5]. The total cross section as a function of γd center-of-mass system $W_{\gamma d}$ does not show a resonance-like behavior. The existing theoretical calculation without any final-state interaction (FSI) based on quasi-free $\pi^0\eta$ photoproduction underestimates the data [6]. The calculation reproduces the data below 1 GeV including meson scattering and absorption of an additionally produced meson on the spectator nucleon [6], and many-body interaction of mesons with the final-state deuteron.

We have measured the differential cross sections $d\sigma/dM_{\pi\eta}$, $d\sigma/dM_{\pi d}$, $d\sigma/dM_{\eta d}$, and $d\sigma/d\Omega_d$ in the γd center-of-mass frame for the first time. Similarly to the $\gamma d \to \pi^0\pi^0 d$ reaction, the angular distribution of deuteron emission is rather flat, and the kinematic condition for the obtained data completely differs from the calculation, suggesting a manifestation of dibaryons also in the $\gamma d \to \pi^0\eta d$ reaction. A possible mechanism would be a sequential reaction $\gamma d \to \mathcal{D}_{\rm IV} \to \pi^0\mathcal{D}_{\rm IS} \to \pi^0\eta d$ and/or $\gamma d \to \mathcal{D}_{\rm IV} \to \eta\mathcal{D}_{\rm IV} \to \pi^0\eta d$ with an isoscalar dibaryon $\mathcal{D}_{\rm IS}$ and an isovector dibaryon $\mathcal{D}_{\rm IV}$. In the observed reaction, both the two nucleons obviously participate before emitting π^0 and η.

The $d\sigma/dM_{\eta d}$ shows a strong enhancement near the ηd threshold at all the incident energies. The S-wave ηd decay of $\mathcal{D}_{\rm IS}$ must be dominant, giving a spin-parity of 1^- for $\mathcal{D}_{\rm IS}$. since a prominent peak near the threshold can be produced if and only if $L = 0$. We confirm the spin-parity of this state from angular distributions of π^0 and η obtained for the events from $M_{\eta d} < 2.47$ GeV. The spin-parity of 1^- corresponds not only to an S-wave ηd state but also an S-wave $N(940)1/2^+$ and $N(1535)1/2^-$ state. Additionally, the real part of the ηd scattering length is determined so that it reproduces the measured $d\sigma/dM_{\eta d}$ distributions. We cannot determine its sign but obtain an absolute value of 1.2 ± 0.2 fm which is a half of the theoretical estimation by Fix *et al* [7].

§4. Summary

We have measured and analyzed the $\gamma d \to \pi^0\eta d$ reaction. The total cross section as a function of γd center-of-mass system $W_{\gamma d}$ is reproduced below 1 GeV by the existing calculation including meson scattering and absorption of an additionally produced meson on the spectator nucleon [6], and many-body interaction of mesons with the final-state deuteron. We also investigate the properties of the threshold enhancement in the $d\sigma/dM_{\eta d}$, and its spin-parity is found to be 1^-. Since the data analysis has been finalized, and the corresponding paper will be submitted soon. Details of the analysis and discussion will be given in the forthcoming arXiv preprint.

Acknowledgment

The authors express gratitude to the ELPH accelerator staff for stable operation of the accelerators in the FOREST experiments. They acknowledge Mr. Kazue Matsuda, Mr. Ken'ichi Nanbu, and Mr. Ikuro Nagasawa for their technical assistance in the FOREST experiments. They also thank Prof. Mikhail Egorov for the theoretical calculations of the cross sections. This work was supported in part by the Ministry of Education, Culture, Sports, Science and Technology, Japan (MEXT) and Japan Society for the Promotion of Science (JSPS) through Grants-in-Aid for Specially Promoted Research No. 19002003, for Scientific Research (A) Nos. 24244022 and 16H02188, for Scientific Research (B) Nos. 17340063 and 19H01902, for Scientific Research (C) No. 26400287, and for Scientific Research on Innovative Areas Nos. 19H05141 and 19H05181.

References

[1] T. Ishikawa *et al.*: Nucl. Instrum. Meth. A **832** (2016) 108.

[2] T. Ishikawa *et al.*: JPS Conf. Proc. **10** (2016) 031001;
T. Ishikawa *et al.*: Phys. Rev. C **101** (2020) 052201 (R).

[3] F. Hinode *et al.*: Proc. of 21st IEEE Particle Accelerator Conference (PAC) (2005) 2458.

[4] T. Ishikawa *et al.*: Nucl. Instrum. Meth. A **622** (2010) 1;
T. Ishikawa *et al.*: Nucl. Instrum. Meth. A **811** (2016) 124;
Y. Matsumura *et al.*: Nucl. Instrum. Meth. A **902** (2018) 103;
Y. Obara *et al.*: Nucl. Instrum. Meth. A **922** (2019) 108.

[5] T. Ishikawa *et al.*, Phys. Lett. B **772** (2017) 398; *ibid.* **789** (2019) 413.

[6] M. Egorov: Phys. Rev. C **101** (2020) 065205.

[7] A. Fix and O. Kolesnikov: Phys. Rev. C **97** (2018) 044001.

Neutron-neutron scattering length from positive pion photoproduction

T. Ishikawa[1], S.X. Nakamura[2,3], and T. Sato[4]

[1]*Research Center for Electron Photon Science (ELPH), Tohoku University, Sendai 982-0826, Japan*
[2]*State Key Laboratory of Particle Detection and Electronics, University of Science and Technology of China, Hefei 230036, China*
[3]*Department of Modern Physics, University of Science and Technology of China, Hefei 230026, China*
[4]*Research Center for Nuclear Physics (RCNP), Osaka University, Ibaraki 567-0047, Japan*

We have considered the possibility of extracting the neutron-neutron scattering length a_{nn} to investigate charge symmetry breaking from the final-state interaction in positive pion photoproduction. Details are described in a preprint submitted to arXiv [S.X. Nakamura, T. Ishikawa, and T. Sato, arXiv: 2003.02497 (2020)].

§1. Charge symmetry breaking

Charge symmetry (CS) is an important concept for describing many facets of nuclear physics: observables are hardly changed when all protons and neutrons are replaced with neutrons and protons, respectively. CS corresponds to invariance under the interchange of u and d quarks, and CS breaking (CSB) takes place owing to differences of u and d masses and electromagnetic effects. Recently, an unexpectedly large difference in the excitation energies is observed between the ${}^{4}_{\Lambda}$He and ${}^{4}_{\Lambda}$H mirror hypernuclei [1, 2]. CSB possibly occurs more strongly in hypernuclei than in oridnary nuclei. The full understanding of CSB still remains an open issue in nuclear physics. To reveal the cause of the CSB, it is important to investigate the low-energy nn and pp scatterings as well as between Λn and Λp scatterings.

§2. Positive pion photoproduction

We have considered the possibility of extracting the neutron-neutron scattering length a_{nn} to investigate CSB from the final-state interaction (FSI) in positive pion photoproduction, the $\gamma d \to \pi^+ nn$ reaction. What we have to do is to measure the pion momentum and its direction precisely at a fixed incident photon energy. An experimental advantage of this reaction is that we can avoid the neutron detection and uncertainty of its efficiency. A kinematic condition with an incident photon energy of 250 MeV and pion emission angle of 0° is suitable for this purpose The differential cross section $d^2\sigma/dM_{nn}/d\Omega_\pi$ is sensitive to the value of a_{nn} below $M_{nn} = 2M_n + 0.5$ MeV where M_{nn} and M_n denote the nn invariant

mass and neutron mass, respectively. It is found that $d^2\sigma/dM_{nn}/d\Omega_\pi$ with 2% error, resolved into M_{nn} bins of 0.04 MeV (corresponding to p_π bins of 0.05 MeV/c), can determine a_{nn} at a precision of $\pm$0.21 fm with a systematic uncertainty of 0.03 fm.

§3. Positive pion electroproduction

High momentum resolutions, at the order better of 10^{-3} or better, are required for the incident photon beam and for the emitted positive pion to determine a_{nn} precisely. These conditions can be achieved by utilizing virtual photons of very low Q^2 from electron scattering at the Mainz MAMI A1 facility [3]. The triple differential cross section for the $(e, e'\pi)$ reaction can be described in the following form (omitting the M_{nn} differentiation) for the unpolarized photon beam and unpolarized target:

$$\frac{d^3\sigma^{ed}}{dE_{e'}\, d\Omega_{e'}\, d\Omega_\pi} = \Gamma_\gamma \left\{ \frac{d\sigma_{\rm T}^{\gamma d}}{d\Omega_\pi} + \epsilon_{\rm L} \frac{d\sigma_{\rm L}^{\gamma d}}{d\Omega_\pi} + \sqrt{2\epsilon_{\rm L}\,(1+\epsilon)} \frac{d\sigma_{\rm LT}^{\gamma d}}{d\Omega_\pi} \cos\phi_\pi + \epsilon \frac{d\sigma_{\rm TT}^{\gamma d}}{d\Omega_\pi} \cos 2\phi_\pi \right\}, \quad (1)$$

where $\sigma_{\rm T}$, $\sigma_{\rm L}$, $\sigma_{\rm LT}$, and $\sigma_{\rm TT}$ are the transverse, longitudinal, longitudinal-transverse interference, and transverse-transverse interference cross sections for $\gamma^* d \to \pi^+ nn$ in the laboratory frame, respectively [4, 5] with a virtual photon flux Γ_γ. The $\sigma_{\rm T}$ corresponds to the cross section for the real photon beam at $Q^2 = 0$, which should be extracted from electroproduction. The $\sigma_{\rm LT}$ and $\sigma_{\rm TT}$ terms vanish when the pion is detected at $\theta_\pi = 0^\circ$ with respect to the virtual photon direction. No condition satisfies that the $\sigma_{\rm L}$ term is negligibly small among the available beam energies and spectrometer settings. We propose a method to separate $\sigma_{\rm T}$ and $\sigma_{\rm L}$ by taking advantage of the linear $\epsilon_{\rm L}$ dependence like a Rosenbluth separation.

§4. Summary

We discussed the possibility of extracting the low-energy neutron-neutron scattering length a_{nn} from $\gamma d \to \pi^+ nn$ cross-section data. High momentum resolutions are required for the photon beam and emitted positive pion, and they can be achieved with an electron scattering experiment at the Mainz MAMI A1facility. The transverse cross section, corresponding to the real photon cross section, can be separated from the electroproduction cross sections at different ϵ_L values but the same $Q^2 \sim 0$ (an almost-real photon condition). Details of our consideration are described in Ref. [6]

Acknowledgment

This work was supported in part by the Japan Society for the Promotion of Science (JSPS) through Grants-in-Aid for Scientific Research (B) No. 19H01902, and for Scientific Research on Innovative Areas Nos. 19H05141 and 19H05181.

References

[1] T.O. Yamamoto et al. (J-PARC E13 collaboration): Phys. Rev. Lett. **115** (2015) 222501.

[2] A. Esser et al. (A1 collaboration at MAMI): Phys. Rev. Lett. **114** (2015) 232501.

[3] K.I. Blomqvist *et al.*: Nucl. Instrum. Meth. A **403** (1998) 263.

[4] T. de Forest: Nucl. Phys. A **392** (1983) 232.

[5] P.J. Mulders: Phys. Rept. **185** (1990) 83.

[6] S.X. Nakamura, T. Ishikawa, and T. Sato: arXiv: 2003.02497 (2020).

Measure of the equality of two distributions

T. Ishikawa[1]

[1]*Research Center for Electron Photon Science (ELPH), Tohoku University, Sendai 982-0826, Japan*

The χ^2 value is used as a quality of the fit when we fit a function to the data using the least-squares approximation. In this report, we discuss a measure of the equality of the two distributions based on Ref. [1].

§1. Standard deviation of a set of values

The standard deviation is a measure of the amount of variation of a set of values in statistics. Suppose we have a set of values x_1, x_2, ..., x_n, and the amount of them is n. The average μ of them is

$$\mu = \frac{\sum_{i=1}^{n} x_i}{\sum_{i=1}^{n} 1} = \frac{1}{n}\sum_{i=1}^{n} x_i \tag{1}$$

and the standard deviation σ is defined by

$$\sigma^2 = \frac{\sum_{i=1}^{n} (x_i - \mu)^2}{\sum_{i=1}^{n} 1} = \frac{1}{n}\sum_{i=1}^{n} (x_i - \mu)^2 = \left(\frac{1}{n}\sum_{i=1}^{n} x_i^2\right) - \mu^2. \tag{2}$$

It should be noted that physicists often use the term root mean square (rms) for σ, and the correct rms value $x_{\rm rms}$ is given in the equation

$$x_{\rm rms}^2 = \frac{1}{n}\left(\sum_{i=1}^{n} x_i^2\right) = \mu^2 + \sigma^2. \tag{3}$$

§2. Standard deviation of a continuous function

In §1, we have discussed the average and standard deviation for a set of values. Here, we discuss those for a continuous function $y = f(x)$ defined in the domain $[x_{\rm min}, x_{\rm max})$. The average $\langle f \rangle$ can be easily estimated as

$$\langle f \rangle = \frac{\int_{x_{\rm min}}^{x_{\rm max}} f(x)\,dx}{\int_{x_{\rm min}}^{x_{\rm max}} 1\,dx} = \frac{1}{x_{\rm max} - x_{\rm min}}\int_{x_{\rm min}}^{x_{\rm max}} f(x)\,dx. \tag{4}$$

In comparison to Eq. (1), x_i and $\sum_{i=1}^{n}$ are replaced with $f(x)$ and $\int_{x_{\min}}^{x_{\max}} dx$, respectively. The standard deviation σ_f is given in the eqation

$$\sigma_f^2 = \frac{\displaystyle\int_{x_{\min}}^{x_{\max}} \Big\{ f(x) - \langle f \rangle \Big\}^2 dx}{\displaystyle\int_{x_{\min}}^{x_{\max}} 1\, dx} = \frac{1}{x_{\max} - x_{\min}} \int_{x_{\min}}^{x_{\max}} \Big\{ f(x) - \langle f \rangle \Big\}^2 dx$$
$$= \frac{1}{x_{\max} - x_{\min}} \int_{x_{\min}}^{x_{\max}} \Big\{ f(x) \Big\}^2 dx - \langle f \rangle^2. \tag{5}$$

The first term of the right-hand side in Eq. (5) corresponds to the rms value of $f(x)$.

§3. Equality of two sets of values

We discuss here the equality of two sets of values (or two histograms with the same number of bins) x_i^1 and x_i^2 for $i = 1,\ 2,\ \ldots,\ n$. The standard deviation

$$\sigma^2 = \frac{\displaystyle\sum_{i=1}^{n} x_i^2}{\displaystyle\sum_{i=1}^{n} 1} = \frac{1}{n} \sum_{i=1}^{n} x_i^2 \tag{6}$$

can be used as a measure of the equality when we do not have to make an additional overall normalization. When the equality of the shapes for the two sets is concern and overall normalization can be made, the minimum σ, given by

$$\sigma^2 = \frac{1}{n} \sum_{i=1}^{n} \left(x_i^2 - c x_i^1 \right)^2, \tag{7}$$

corresponds to a measure of the equality. The σ value depends on the normalization factor c:

$$\sigma^2 = \left\{ \frac{1}{n} \sum_{i=1}^{n} \left(x_i^1 \right)^2 \right\} c^2 - 2 \left\{ \frac{1}{n} \sum_{i=1}^{n} x_i^1 x_i^2 \right\} c + \left\{ \frac{1}{n} \sum_{i=1}^{n} \left(x_i^2 \right)^2 \right\}, \tag{8}$$

and the minimum σ is provided when

$$\frac{\partial \sigma^2}{\partial c} = 0. \tag{9}$$

Thus, the normalization factor c for the minimum σ can be directly calculated as

$$c = \frac{\left\{ \dfrac{1}{n} \displaystyle\sum_{i=1}^{n} x_i^1 x_i^2 \right\}}{\left\{ \dfrac{1}{n} \displaystyle\sum_{i=1}^{n} \left(x_i^1 \right)^2 \right\}}. \tag{10}$$

The minimum σ^2 is obtained by substituting this c to Eq. (7):

$$\sigma^2 \big|_{\min} = \left\{ \frac{1}{n} \sum_{i=1}^{n} \left(x_i^2 \right)^2 \right\} - \frac{\left\{ \dfrac{1}{n} \displaystyle\sum_{i=1}^{n} x_i^1 x_i^2 \right\}^2}{\left\{ \dfrac{1}{n} \displaystyle\sum_{i=1}^{n} \left(x_i^1 \right)^2 \right\}}. \tag{11}$$

This $\left| \sigma^2 \right|_{\min}$ corresponds to the measure of the equality of the two sets x_i^1 and x_i^2 when overall normalization can be made freely.

When x_i^1 and x_i^2 have uncertainties δx_i^1 and δx_i^2, respectively, the minimum value of χ^2, given by

$$\chi^2 = \sum_{i=1}^{n} \frac{\left(x_i^2 - c x_i^1\right)^2}{\left(\delta x_i^2\right)^2 + \left(c\delta x_i^1\right)^2}, \tag{12}$$

should be used instead of the minimum σ^2 in Eq. (7). The normalization factor c is obtained from the condition $\partial\chi^2/\partial c = 0$ in principle, but it requires complicated calculations. When x_i^1 does not have an uncertainty or $\delta x_i^1 = 0$ for all the is, $n\,\sigma^2\big|_{\rm min}$ calculated in Eq.(11) can be used as the measure of the equality by replacing x_i^1 and x_i^2 with $x_i^1/\delta x_i^2$ and $x_i^2/\delta x_i^2$, respectively.

§4. Equality of two continuous functions

Finally, we discuss the equality of two continuous functions $f_1(x)$ and $f_2(x)$ defined in the domain $[x_{\rm min}, x_{\rm max})$. The standard deviation

$$\sigma_f^2 = \frac{\displaystyle\int_{x_{\rm min}}^{x_{\rm max}} \Big\{f(x)\Big\}^2\,dx}{\displaystyle\int_{x_{\rm min}}^{x_{\rm max}} 1\,dx} = \frac{1}{x_{\rm max} - x_{\rm min}} \int_{x_{\rm min}}^{x_{\rm max}} \Big\{f(x)\Big\}^2\,dx \tag{13}$$

can be used as a measure of the equality when we do not have to make an additional overall normalization. When the equality of the shapes for the two sets is concern and overall normalization can be made, the minimum σ, given by

$$\sigma_f^2 = \frac{1}{x_{\rm max} - x_{\rm min}} \int_{x_{\rm min}}^{x_{\rm max}} \Big\{f_2(x) - c f_1(x)\Big\}^2\,dx \tag{14}$$

corresponds to a measure of the equality. The σ value depends on the normalization factor c:

$$\sigma_f^2 = \langle f_1^2\rangle c^2 - 2\langle f_1 f_2\rangle c + \langle f_2^2\rangle \tag{15}$$

with

$$\begin{aligned}
\langle f_1^2\rangle &= \frac{1}{x_{\rm max} - x_{\rm min}} \int_{x_{\rm min}}^{x_{\rm max}} \Big\{f_1(x)\Big\}^2\,dx, \\
\langle f_1 f_2\rangle &= \frac{1}{x_{\rm max} - x_{\rm min}} \int_{x_{\rm min}}^{x_{\rm max}} f_1(x) f_2(x)\,dx, \text{ and} \\
\langle f_2^2\rangle &= \frac{1}{x_{\rm max} - x_{\rm min}} \int_{x_{\rm min}}^{x_{\rm max}} \Big\{f_2(x)\Big\}^2\,dx.
\end{aligned} \tag{16}$$

The minimum σ_f is provided when

$$\frac{\partial\sigma_f^2}{\partial c} = 0. \tag{17}$$

The optimum normalization to minimize σ_f^2 is given by

$$c = \frac{\langle f_1 f_2\rangle}{\langle f_1^2\rangle}, \tag{18}$$

and the mimimum σ_f^2 is ca;culated by

$$\sigma_f^2\big|_{\rm min} = \langle f_2^2\rangle - \frac{\langle f_1 f_2\rangle^2}{\langle f_1^2\rangle}. \tag{19}$$

When $f_1(x)$ and $f_2(x)$ have uncertainties $\delta f_1(x)$ and $\delta f_2(x)$, respectively, the minimum value of χ^2_f, given by

$$\chi^2_f = \int_{x_{\min}}^{x_{\max}} \frac{\Big\{ f_2(x) - c f_1(x) \Big\}^2}{\Big\{ \delta f_2(x) \Big\}^2 + \Big\{ c \delta f_1(x) \Big\}^2} dx, \tag{20}$$

should be used instead of the minimum σ^2_f in Eq. (14). The normalization factor c is obtained from the condition $\partial \chi^2 / \partial c = 0$ in principle, but it requires complicated calculations. When $f_1(x)$ does not have an uncertainty or $\delta f_1(x) = 0$ over the domain, $n\, \sigma^2_f \Big|_{\min}$ calculated in Eq. (19) can be used as a measure of the equality by replacing $f_1(x)$ and $f_2(x)$ with $f_1(x)/\delta f_2(x)$ and $f_2(x)/\delta f_2(x)$, respectively.

Acknowledgment

This work was supported in part by the Japan Society for the Promotion of Science (JSPS) through Grants-in-Aid for Scientific Research (B) No. 19H01902, and for Scientific Research on Innovative Areas Nos. 19H05141 and 19H05181.

References

[1] T. Ishikawa, Internal GeV-γ Analysis Note HD No. 437$\mathcal{P}$ **(2020)**.

(ELPH Experiment : #2844, #2882, #2894, #2924)

Current status of the FOREST/BLC experiments at ELPH

T. Ishikawa[1], K. Aoki[2], H. Fujioka[3], Y. Honda[1], T. Hotta[4], K. Itahashi[5], H. Kanda[4], H. Kawai[6], K. Maeda[7], Y. Matsumura[1], M. Miyabe[1], S. Miyata[8], N. Muramatsu[1], H. Ohnishi[1], K. Ozawa[2], Y. Sada[1], H. Shimizu[1], M. Tabata[6], A.O. Tokiyasu[1], and Y. Tsuchikawa[9] for the FOREST/BLC collaboration

[1]*Research Center for Electron Photon Science (ELPH), Tohoku University, Sendai 982-0826, Japan*
[2]*Institute of Particle and Nuclear Studies, High Energy Accelerator Research Organization (KEK), Tsukuba 305-0801, Japan*
[3]*Department of Physics, Tokyo Institute of Technology, Tokyo 152-8551, Japan*
[4]*Research Center for Nuclear Physics (RCNP), Osaka University, Ibaraki 567-0047, Japan*
[5]*Nishina Center for Accelerator-Based Science, RIKEN, Wako 351-0198, Japan*
[6]*Department of Physics, Chiba University, Chiba 263-8522, Japan*
[7]*Department of Physics, Tohoku University, Sendai 980-8578, Japan*
[8]*Department of Physics, University of Tokyo, Tokyo 113-0033, Japan*
[9]*J-PARC Center, Japan Atomic Energy Agency (JAEA), Tokai 319-1195, Japan*

The FOREST/BLC experiments are conducted to determine low-energy S-wave ηn scattering parameters using the $\gamma d \to p\eta n$ reaction. The photon beam with energies around 940 MeV can give the recoilless condition of produced η mesons by detecting the protons at 0°. The effects of the final-state ηn interaction must be enhanced due to the small relative momentum between the η meson and the residual neutron in this kinematics. In this year, the physics data were collected from April 8 to May 6 in 2019. In this report, a brief summary of the current status of the FOREST/BLC experiment and collected data are described.

§1. Introduction

The nucleon resonance $N(1535)S_{11}$ (N^*) is an interesting object, which can be an S-wave ηN molecule-like state and/or the chiral partner of the nucleon N. Recently, the internal structure of a hadron has been intensively discussed in terms of the compositeness X, which is an overlap with the two-body scattering state [1]. The X can be given by the two-body low-energy scattering parameters for the S-wave bound states and resonances in the threshold energy region [2]. The value of $X_{\eta N} = 0.04 + i0.37$ fm obtained from the current knowledge of the ηN-scattering amplitude suggests a three-quark state [3]. However, ηN scattering is not well known yet due to the difficulties in realizing scattering experiments because of the neutral and unstable nature of η (in general, it is difficult to obtain the low-energy scattering parameters between a neutral meson and nucleon [4]). The reliability of the deduced $X_{\eta N}$ and corresponding structure of N^* remains questionable.

The $a_{\eta N}$ values have been extracted by many theoretical analyses from the differential and total cross sections for the $\pi N \to \pi N$, $\pi N \to \eta N$, $\gamma N \to \pi N$, and $\gamma N \to \eta N$ reactions. Currently, the estimated $a_{\eta N}$ values are highly model dependent. While the values of Im$[a_{\eta N}]$ are confined into a narrow range from 0.2 to 0.3 fm, and those of Re$[a_{\eta N}]$ are scattered in a wide range from 0.2 to 1.1 fm [8]. This uncertainty comes from the fact that the existing experimental data used for extracting $a_{\eta N}$ do not enhance the effect of the ηN-scattering ($\eta N \to \eta N$) amplitude. We propose the $\gamma d \to \eta pn$ reaction to determine $a_{\eta N}$ at a certain kinematics, which enhances the ηN scattering effect.

The incident photon bombards the quasi-free proton in the deuteron and produces a virtual η meson with a very low momentum. Events are selected in which the incident energy is approximately 0.94 GeV and the proton is detected at 0°. The kinematics for these events satisfies the recoilless condition of the produced η mesons. Thus, low-energy ηn scattering is expected to take place in this condition, where the pn and ηp rescattering effects are suppressed owing to their large relative momenta ($\sim$ 0.94 GeV). The sensitivity to the Re$[a_{\eta n}]$ and Re$[r_{\eta n}]$ values are investigated and summarized in Ref. [7] by using a model based on a dynamical coupled-channel meson-baryon scattering analysis [9, 10].

§2. Experimental setup

The $\gamma d \to p\eta n$ reaction is measured at the Research Center for Electron Photon Science (ELPH), Tohoku University, Japan [11] with the FOREST electromagnetic calorimeter system [12] together with an additional forward charged-particle spectrometer called BLC [13]. The incident photon energy ranges from 0.82 to 1.26 GeV [15] for the circulating energy of 1.32 GeV in the electron synchrotron called the booster storage (BST) ring [16]. The details of the FOREST detector including the liquid deuterium target are described elsewhere [14]. The forward scattered proton is momentum-analyzed with the BLC spectrometer behind FOREST. The trajectory of a charged particle is measured with 2 planar drift chambers (DCs), and the time of flight is measured with 14 plastic scintillator (PS) hodoscopes (PSH+). An additional e/π separation is made using 10 SF5 lead-glass Cherenkov counters (LGCs). The experimental setup has been fixed since November in 2017. In this year, the physics data were collected in a period: April 8 to May 6 (2019A) in 2019.

The BLC magnet was excited every time at normal operation in this fiscal year with a coil current of 1400 A. The magnetic flux B_y at the center was monitored with a nuclear magnetic resonance (NMR) probe during the experiments, and B_y = 716.0 mT was adjusted by changing the coil current. Fig. 1 shows the magnetic flux B_y at the center for the 2019A period.

§3. Collected data

The physics data with the deuterium and hydrogen targets were collected in the 2019A period. The BST ring was operated with a circulating energy of 1.32 GeV, a current of approximately 20 mA. The data collections were basically stable during the period. The injector linac suddenly died twice owing to the current/voltage over at the beginning of the period. DC power supply modules became out of order three times for the septum magnet. The beam was recovered by replacing a module with a new one. Table 1

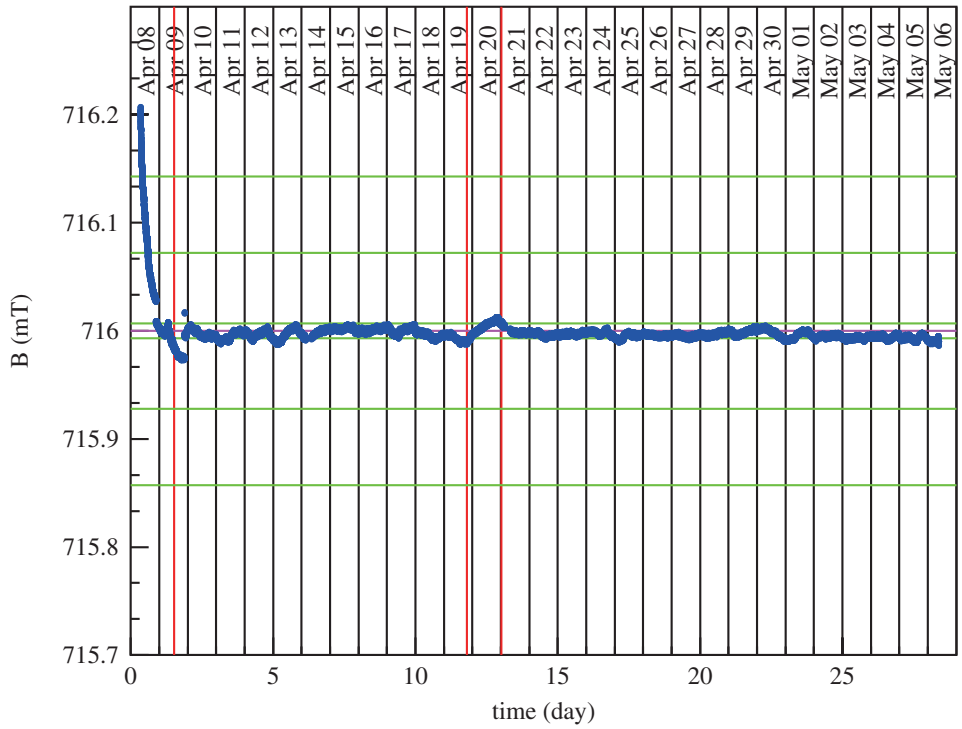

Fig.1. Long-term variation of the magnetic flux at the BLC center measured with NMR in 2019A. The horizontal axis represents the number of days from 0:00am on April 08 in 2019, and the vertical shows the magnetic flux in mT. the red vertical lines correspond to the start timings of collecting the hydrogen, empty, and deuterium targets. The horizontal green lines show the $\pm 0.001\%$、$\pm 0.01\%$、$\pm 0.02\%$ variation from the set value of 716.00 mT.

summarizes the number of spills and events of the collected data in this fiscal year (2018). The statistics for each of the hydrogen and deuterium data was 1.5 times higher than that for the 2009D period. The data analysis is on-going to perform the precise energy and timing calibrations of the STB-Tagger II, FOREST, and BLC detectors. The preliminary data are presented in Ref. [6].

Table 1. Numbers of spills and events collected in this fiscal year (2019). The circulating electron energy of the BST ring was 1.3 GeV. The targets used were liquid hydrogen, deuterium, and empty.

period	hydrogen		deuterium		empty	
	#spills	#events	#spills	#events	#spills	#events
2019A	45.48 k	749.54 M	76.26 k	1, 388.36 M	8.96 k	121.26 M

Acknowledgment

The authors express gratitude to the ELPH accelerator staff for stable operation of the accelerators for testing the AC detector. They acknowledge Mr. Ken'ichi Nanbu, and Mr. Ikuro Nagasawa for their technical assistance. This work was supported in part by the Japan Society for the Promotion of Science (JSPS) through Grants-in-Aid for Scientific Research (B) No. 19H01902, and for Scientific Research on

Innovative Areas Nos. 19H05141 and 19H05181.

References

[1] S. Weinberg: Phys. Rev. **137** (1965) B672.

[2] T. Hyodo: Phys. Rev. Lett. **111** (2013) 132002.

[3] T. Sekihara, T. Arai, J. Yamagata-Sekihara, S. Yasui: Phys. Rev. C **93** (2016) 035204.

[4] T. Ishikawa *et al.*: Phys. Rev. C **101** (2020) 052201 (R).

[5] T. Ishikawa *et al.*: JPS Conf. Proc. **13** (2016) 020031.

[6] T. Ishikawa *et al.*: Acta Phys. Polon. B **48** (2017) 1801.

[7] S.X. Nakamura, H. Kamano, T. Ishikawa: Phys. Rev. C **96** (2017) 042201 (R).

[8] Q. Haider, L.C. Liu: Int. J. Mod. Phys. E **24**, 1530009 (2015); and references therein.

[9] A. Matsuyama, T. Sato, T.-S.H. Lee: Phys. Rep. **439** (2007) 193.

[10] H. Kamano *et al.*: Phys. Rev. C **88** (2013) 035209.

[11] H. Hama: AAPPS Bulletin **30** (2020) 41.

[12] T. Ishikawa *et al.*: Phys. Lett. B **772** (2017) 398;
T. Ishikawa *et al.*: Phys. Lett. B **789** (2019) 413;
T. Ishikawa *et al.*: PoS (Hadron2013) 095;
Y. Tsuchikawa *et al.*: JPS Conf. Proc. **17** (2017) 062007;
T. Ishikawa *et al.*: PoS (INPC2016) 267.

[13] T. Ishikawa *et al.*: Acta. Phys. Polon. B **48** (2017) 1801;
T. Ishikawa *et al.*: JPS Conf. Proc. **10** (2016) 031001;
T. Ishikawa *et al.*: JPS Conf. Proc. **13** (2017) 020031;

[14] T. Ishikawa *et al.*: Nucl. Instrum. Meth. A **832** (2016) 108.

[15] T. Ishikawa *et al.*: Nucl. Instrum. Meth. A **622** (2010) 1;
T. Ishikawa *et al.*: Nucl. Instrum. Meth. A **811** (2016) 124;
Y. Matsumura *et al.*: Nucl. Instrum. Meth. A **902** (2018) 103;
Y. Obara *et al.*: Nucl. Instrum. Meth. A **932** (2019) 108.

[16] F. Hinode *et al.*: J. Phys. Conf. Ser. **425** (2013) 072011.

(ELPH Experiment : #2925)

Study on the variation of efficiency and time resolution depending on the electrode material of Resistive Plate Chamber

J. Takahashi[1], H. Ohnishi[1], M. Miyabe[1], A. O. Tokiyasu[1], Y. Sada[1], C. Yoshida[1], H. Saito[1], M. Turuta[1], R. Nishikawa[1], and T. Nobata[1]

[1]*Research Center for Electron Photon Science, Tohoku University, Sendai, 982-0826*

We are developing a resistive plate chamber(RPC) for the E50 experiment at J-PARC [1]. The electrode material used to supply HV on to the detector is not available on the market to date. Therefore, it is mandatory to find a substitute for the electrode to construct next-generation RPC. We successfully identified an electrode candidate and constructed an RPC by using the new electrode.

In this paper, we describe the results of the test experiments at the positron beamline of ELPH, Tohoku University.

§1. Introduction

One of the hot topics in hadron physics is to reveal effective degrees of freedom (DoF) to describe a hadron. These days, we believe there is a di-quark cluster that emerged as new degrees of freedom in hadrons other than constituent quarks, which is expected to appear in baryons. However, it is quite difficult to find it in a normal baryon. Because a mass of constituent quarks in a normal baryon is almost equal, therefore it cannot be identified di-quark structure among those three constituent quarks in a baryon.

The powerful and effective way to shed light on the cluster inside a baryon is, indeed, the spectroscopy of baryons which contained at least one heavy quark inside, e.g., charm or bottom quark. One of the important interactions between constituent quarks in hadron is color-magnetic interaction, which is inversely proportional to the product of masses of two quarks. In the case of a baryon with one heavy quark in it, such as a charmed baryon, the interaction between heavy quark-light quark gets to be weakened relative to the interaction between light quarks because of the nature of color-magnetic interaction. Thus cluster of two light quark structures will be enhanced effectively. Therefore unique charmed baryon mass spectrum in excited charmed baryon spectrum will be expected.

The J-PARC E50 experiment is focusing to reveal the di-quark cluster in charmed baryons. The E50 experiment will measure both production cross-section and decay products of charmed baryon in high-momentum pi-p reaction via missing-mass and invariant mass technique.

Figure1 shows a schematic view of the J-PARC E50 spectrometer system [2]. We are developing the detector which is labeled as ”internal ToF Wall” in the figure. The main purpose of the detector is to separate low-energy ($\sim$1 GeV) π and K via a time-of-flight method. The time-resolution required for the

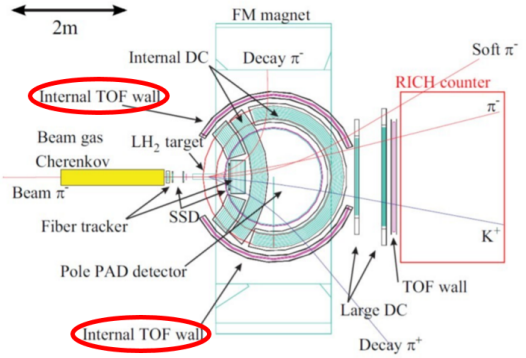

Fig.1. Spectrometer system of E50 experiment

detector is evaluated to be within 100 ps. In addition, the detector is placed inside the dipole magnet, therefore the detector must work properly under the existence of a high magnetic field. Based on the consideration above, we decided to construct the ToF detector by using the Resistive Plate Chamber technique, which recently developed for a large volume with a high timing-resolution ToF detector.

§2. Resistive Plate Chamber (RPC)

RPC is a gas-based detector that mainly used for a Time of Flight (ToF) measurement. The typical structure is shown in Fig.2. Fig.2(Left) shows a single stuck structure and Fig.2(Right) shows a double stuck structure of RPC. The single stuck detector is relatively easy to construct, however, the double stuck detector shows good timing and efficiency performance. Because the signal readout from the central read-out(R/O) pad is summed up signals of the top and bottom part of the detector. Therefore, the signal of the detector is nearly doubled compared with a single stack structure.

We constructed RPCs for ToF measurement for LEPS2 experiment at SPring-8 [3]. Based on this experience, we decide to construct RPCs for the E50 experiment. However, one problem raised. We used the high-resistance tape for the electrode to supply High voltage to the detector. For LEPS2-RPC, we used the carbon-tape called T-9145 from ESD EMI Engineering Co., Ltd., [4]. Unfortunatelly, the tape is no longer available on the market. Therefore we need to find a substitute for the tape used for LPES2-RPC to construct new RPCs for the E50 experiment.

§3. Resistive Tape

The tape used for the electrodes of the RPC must be high resistance. If the resistance of electrodes is low, the signal generated by RPC will be diffused. This increases the rate of crosstalk and reduces the charge on the output signal. On the other hand, if the resistance is too high, the rate tolerance will be partially reduced. Table.1 shows a list of high-resistance tape that has actually been used to construct prototype RPC and tested with cosmic rays. Fig.3 shows RPCs made using these tapes. As a result of the cosmic ray test, detectors constructed with low resistivity tapes were noisy, and the signal could not be seen. Only one candidate remained with the cosmic ray test. That is MK-APT of Tanimura Co., Ltd.,

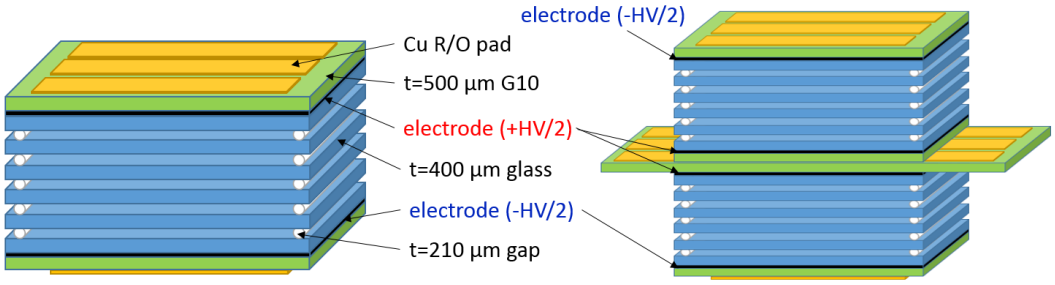

Fig.2. The typical structure of RPC. The left is called single-stack RPC and the right is called double-stack RPC. Double-stack is a structure in which two single-stack are stacked.

[5]. For the detailed investigation, we decided to perform the RPC beam test by using MK-APT as a high-voltage electrode of the detector.

Tape	Resistance [Ω]	Price [JPY/m]	Signal
T-9145	1.5×10^7	10000	Can see
ASB-110	1.3×10^4	13000	Noisy
ASB-121	7.5×10^3	8800	Noisy
MK-APT	2.0×10^8	1000	Can see
TW-CPT	6.2×10^5	500	Can't see
SDT1005	6.0×10^3	6000	Noisy

Table. 1. List of high-resistance tapes used for RPC

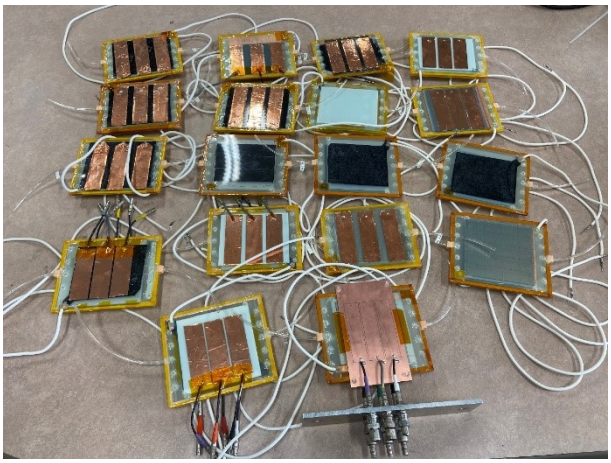

Fig.3. Puroduced RPC

§4. Test Experiment with positron beam at GeV-γ experimental hall

The test experiment is performed with a positron beam at the GeV-γ experimental hall. The γ-ray from the BST ring is converted to the electron-positron pairs in the 200 μm-thick tungsten installed in front of the Tag-X magnet. The converted positrons' momentum is selected by Tag-X magnet and transported to the test experimental area. The experimental setup is shown in Fig.3. The momentum of the positrons used in the test experiment was 671 MeV/c. The positron's typical intensity is about 2000 Hz with 60x60/cm^2, a covered region of trigger counters, Trigger1, and Trigger2. The test detector is installed as a first detector of the setup to eliminate the beam position's energy loss and multiple-scattering. Two first scintillator counters, which required H2431 PMTs on both end, are installed just after the Trigger1 to generate the system's reference timing.

We tested three single-stack RPCs and a double-stack RPC using ordinally carbon tape, *i.e.*, T-9145, and two single-stack RPCs using MK-APT.

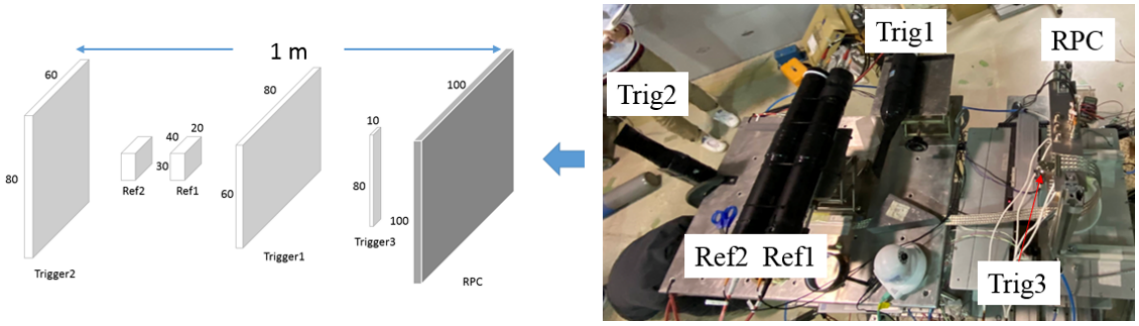

Fig.4. Schematic view (left) and photo (right) of experimental setup

§5. Results and Discussion

Fig.5 shows detector efficiency as a function of the applied voltage. Three blue curves show the results from a single stack detector with T-9145. The blue curve shows results from the double stuck detector with T9145. The red one is the results of a single stuck detector with MK-APT. The efficiency for all RPCs has reached a plateau, ∼90 % when the applied voltage is 16 kV. However, it is instantly noticed that the detector constructed with MK-APT needs to apply ∼13% more high-voltage to reach efficiency plateau.

In this test, we construct two single stuck RPCs with MK-APT. One RPC is properly working during the beam test, which is shown in the Fig5. However, the other one never worked. A detailed investigation to find the difference between those two has been performed, and finally, we found that the resistance of MK-APT changed during the production process of RPC. Therefore, we need further study on the properties of MK-APT itself and optimize the production process.

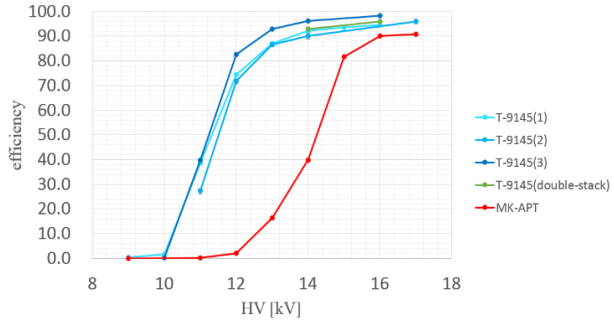

Fig.5. Detector efficiency as a function of applied voltage.

Next, we will evaluate the time resolution of detectors. Since the signal charge output from single-stack RPC was small, the time resolution could not be evaluated. Therefore, we will only evaluate the time resolution for double-stack RPC. The time resolution of RPC is derived using three detectors, Reference1, Refference2, and RPC. Fig.6 shows the distribution of the time difference between Refference1 and RPC vs. output charge of the RPC(ADC). The time-resolution is evaluated after time-work correction(slewing correction), shown as the most right figure in Fig.6. The time difference between each detector after slewing correction are shown in Fig.7. The intrinsic time resolution of the RPC derived

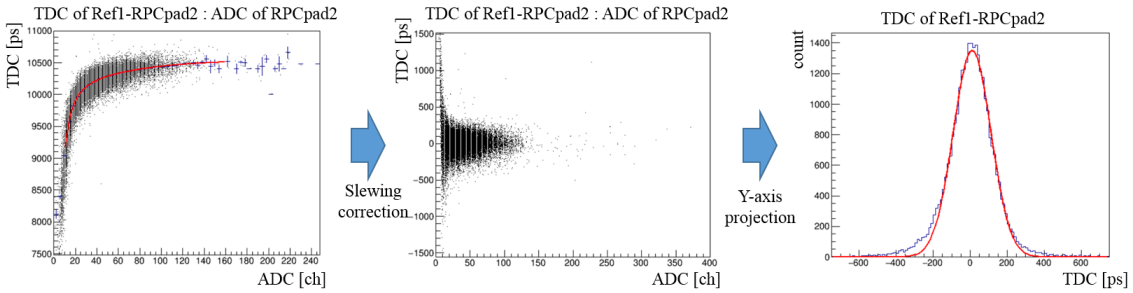

Fig.6. Distribution of the time difference between Refference1 and RPC vs. ADC of the RPC, and state of slewing correction.

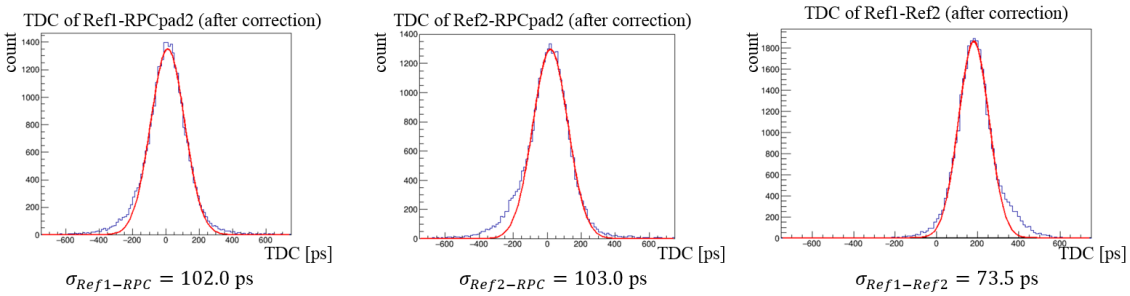

Fig.7. Time difference after slewing correction of Refference1 and RPC (left), Refference2 and RPC (center), Refference1 and Refference2 (right).

from Fig.7 was 88 ps.It turns out that the experimental system can measure a time resolution of 90 ps. Immediately in the future, we will manufacture a double-stuck RPC using MK-APT and measure the time resolution.

§6. Summury

We are developing a resistive plate chamber(RPC) for the E50 experiment at J-PARC. The electrode material used to supply HV on to the detector is not available on the market to date. Thus, we need to search for high-resistance tapes that can be used for RPC electrodes. After the evaluation process with cosmic ray, we found one promising candidate, which can be used for RPC production. The performance test experiment has been performed at the ELPH GeV-gamma beamline. On the test experiment, we were comparing the detector performance with the detector constructed with the ordinal electrode (T-9145) and with the new candidate MK-APT. The detection efficiency of RPC using MK-APT reached 90 % at the applied voltage of 16 kV. However, we need 13% more HV need to supply to the detector with MK-APT. Time resolution of RPC using MK-APT could not be measured. In the future, we will make a double-stuck RPC using MK-APT and compare it with the time resolution.of that using T-9145.

Acknowledgments

We are grateful to the all staff members of ELPH for their extensive efforts on the successful operation of the facility. This work is partly supported by the MEXT Grants-in-Aid for Sientific Research on Innovative Areas "Clustering as a window on the hierarchical structure of quantum systema" Group-A02(18H05402).

References

[1] J-PARC E50 proposal, see http://j-parc.jp/reseacher/Hadron/en/Proposal_e.html

[2] Y.Komatsu JPS Conf. Proc. 26(2019) 022029

[3] K. Watanabe ***et al.*** Nucl. Instrum. Meth. A 925(2019)188

[4] https://www.esd-emi.com

[5] https://www.tanimura.biz/catalog/antistatic_cl_pettape.html

(ELPH Experiment : #2926)

Performance Evaluations of Resistive Plate Chamber with R1234ze as eco-friendly gas

Ryota NISHIKAWA[1*], Kazuya NOBATA[1*], Junpei TAKAHASHI[1*], and Hiroaki OHNISHI[1*]

[1]*Research Center for Electron Photon Science, Tohoku University, Sendai, 982-0826*

Resistive Plate Chamber (RPC) is one of the most popular detectors for Time-of-flight measurement. However, the gas used for the detectors is known to have high global warming power. Thus we need to find a substitute with a more eco-friendly one. One of the candidates is the gas called R1234ze, which has $\sim$ thousand times lower global warming power than R134a. In this report, the RPC performance evaluation results with R1234ze gas will be presented instead of R134a.

§1. Introduction

Resistive Plate Chamber (RPC) is one of the most attractive technologies for Time-of-Flight (TOF) measurement. These days, many nuclear and high energy physics experiments used RPC as their ToF detector for three reasons as follows. First of all, RPC has a good time resolution of about 50 ps and close to 100% detection efficiency. Second, the large size of the detector can easily be constructed at a low cost. Lastly, the detector works perfectly under a high magnetic field environment.

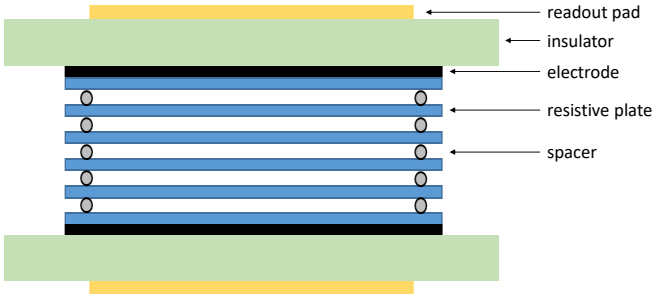

Fig.1. The schematic view of the multi-gap RPC

Figure 1 shows a schematic view of the RPC structure. The detector was composed of multiple resistive plates, which kept a gap between plates by spacers. The typical size of the gap is an order of a few hundred μm. We are using the fishing line as a spacer. Gaps are filled with detector gas, a mixture

*Present address: Research Center for Electron Photon Science, Tohoku University, Sendai, 982-0826

of R134a(1,1,1,2-Tetrauoroethane/CH2FCF3), iso-C4H10, and SF6. This gas mixture is commonly used as a detector gas worldwide. The high voltage is applied to electrodes, which are placed most outside of the resistive plate. The electric field generated by the applied high voltage is reached as ∼10 kV/mm. Once a charged particle passes through the detector, the gas between the gap will be ionized and start to instantly multiplicate electrons due to the high electric field. Soon after, developed electric signals are induced to the readout pad placed most outside of the detector. There are two types of operation modes. One is a streamer mode, which makes a large signal. We expect to have high detection efficiency in this operation mode. However, only poor timing resolution is obtained,*i.e.*, ∼1 ns. This operation mode is suitable for the RPC used as a trigger counter. The other operation mode is the avalanche mode operation. In this operation mode, a good time resolution of the detector is achievable, *i.e.*, ∼50 ps. However, the signal generated from the detector is so small. Thus a high-performance pre-amplifier is needed to be equipped on the detector.

Global warming is one of the most serious problems for human beings. To reduce the warming speed on earth, the reduction of global warming gas usage is agreed international wide. The Global Warming Potential (GWP) is an indicator to evaluate the badness of the gas used, which is normalized with the warming power of CO2. The gas mixture of (R134a : iC4H10 : SF6 = 90 : 5 : 5.) are used widely for RPC. GWP of this gas mixture is estimated to be 2,427. Thus, nowadays, gas using for RPC is indeed categorized as a global warming gas. RPC operation with non- or less GWP gas mixture is one of the great challenges for RPC development.

Recently, R1234ze (trans-1,3,3,3-Tetrauoropropene/C2H2FCF3) has been used as a replacement for R134a, which is widely used for refrigerant of an air conditioner. The GWP of R1234ze is expected to be 1. Therefore, we may have a chance to operate RPC with low GWP gas by changing RPC's main gas from R134a to R1234ze.

This report will present the difference in RPC performance by changing the mixture of gas content.

§2. Gas mixture

The GWP of the gas with a different mixture of content and fraction is summarized in Table1. In case if we replaced R134a with R1234ze, we could reduce the GWP by half.

Table. 1. Mixture rate and GWP

R134a:iC_4H_{10}:SF_6 (GWP)	R1234ze:iC_4H_{10}:SF_6 (GWP)
90:5:5 (2,427)	90:5:5 (1,141)
95:5:0 (1,359)	95:5:0 (1)
90:10:0 (1,287)	90:10:0 (1)
80:20:0 (1,145)	80:20:0 (2)
	95:0:5 (1,141)

§3. RPC used for the test experiment

For this experiment, RPC with five gaps has been constructed. To make gaps, the fishing line is used as a spacer, whose diameter is 0.260mm. As resistive plates, thin glass plates are used. The size of a glass plate is 100mmx100mmx0.4mm. On both sides of RPC, 3 readout pads are placed, whose size is 20mm×80mm.

§4. Test setup

The test experiment is performed with a positron beam at Gev-gamma experimental hall. Bremsstrahlung gamma-ray is delivered to the Gev-gamma experimental hall, and converted to electron-positron pair by a thin metal foil as a converter. A positron with a momentum of 600 MeV/c has been selected via Tag-X magnet and delivered to the positron beamline. Figure 2 shows a schematic view of the test experiment setup. The beam first hit on the test detector, and events are triggered by the coincidence signal from two scintillator counters, *i.e.*, Trig1 and Trig2. The signal from Trig3, which is a very narrow scintillator counter, is used offline analysis to ensure the positron hit on a readout pad on RPC.

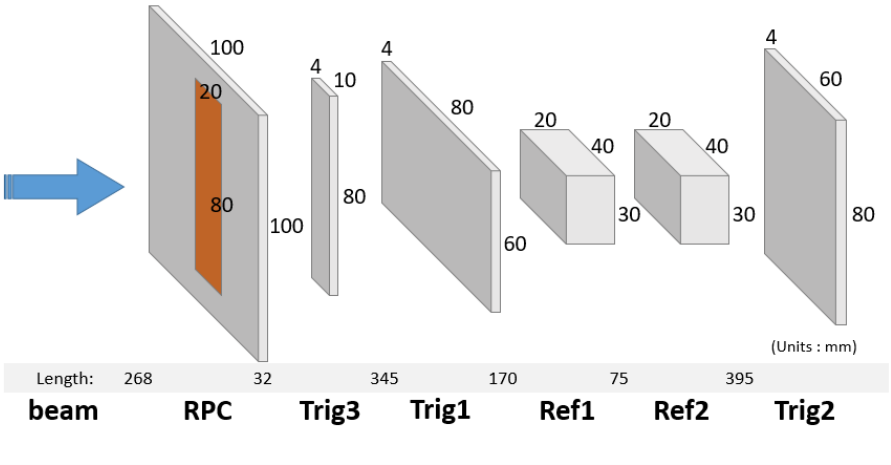

Fig.2. The schimatic view of the test experimental setup

§5. Result and discussion

Figure 3 shows a typical crrelation between pulse hight and timing measurement by the test chamber with a standard gas mixture. The difference between the left and the right figure is its applied high voltage to the chamber. Once we increase applied voltage, the single cluster distribution which is shown in the left figure split into two parts. The one which has lower ADC is understood as a signal from avalanche mode operation. The other one which has high ADC value is from streamer mode operation. For the ToF detector, we need to minimize the fraction of the event detected with the streamer mode operation. Thus, we defined the streamer fraction as a number of events generated via streamer mode operation, with respect to the total number of events.

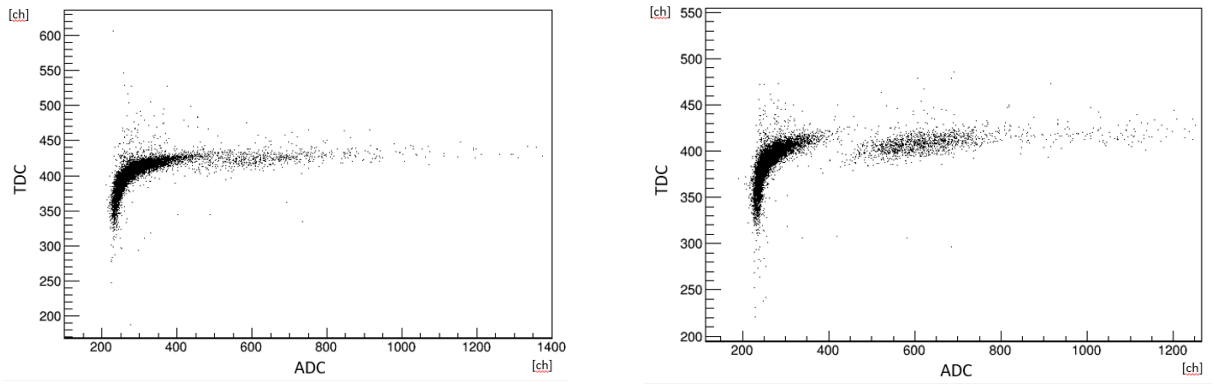

Fig.3. Correlation plot between ADC and TDC

The definition of efficiency(Eff) is as follows.

$$\text{Eff} = \frac{\boldsymbol{Trig}1 \otimes \boldsymbol{Trig}2 \otimes \boldsymbol{Trig}3 \otimes \boldsymbol{RPC}(\text{withTDC valid hit})}{\boldsymbol{Trig}1 \otimes \boldsymbol{Trig}2 \otimes \boldsymbol{Trig}3} \quad (1)$$

Where $\boldsymbol{RPC}$(withTDC valid hit) is that TDC value is not overflowed, *i.e.*, TDC $\neq$ 4095.

Figure 4 shows detector efficiency(shown as a solid circle) and streamer fraction(shown as a solid diamond) as a function of the applied high voltage by using R134a as a based gas. The efficiency reached more than 95% when we applied more than 13.5 kV to the detector. For the case of R134a based gas, efficiency is not sensitive by changing mixed fraction for other gases. The streamer fraction is at most 10% with the high voltage $\sim$ 17 kV. On the other hand, if the detector operated with R1234ze based gas, both efficiency and streamer fraction are susceptible by changing the gas mixture fraction. Moreover, detector efficiency does not reach the efficiency plateau with H.V. =17 kV, which is the maximum voltage we can apply for this test experiment. One of the reasons why the efficiency of the R1234ze based operation is lower than R341a based operation is that the produced charge is smaller in R1234ze than R134a. Need more study about the signal charge depending on the gas mixture. R1234ze based gas can be used as a detector gas, however, we need to apply at least about 30% more H.V. than R134a based gas detector. Further studies are needed to make a solid conclusion.

Figure 5 shows the efficiency of the detector operation with R1234ze based gas. The left side is adding only 5% of iC4H10, and the right is adding 5% SF6. For the gas with 5% iC4H10, we repeated measurement three times and got almost consistent results. The situation is also the same for the gas with 5% SF6. It is interesting to note that the gas with 5% iC4H10 shows higher efficiency than the gas with 5% SF6. The difference can be interpreted as the produced signals can be quenched by SF6 more than iC4H10.

§6. Summury

To date, RPC is known to be a commonly used detector for Time-of-flight measurement. However, because the gas used for RPC is categolized as Global warming gas, detector gas for RPC need to be replaced by concerning on the global warming.

We tested RPC operation with an eco-friendly gas mixture and found promising results. The detec-

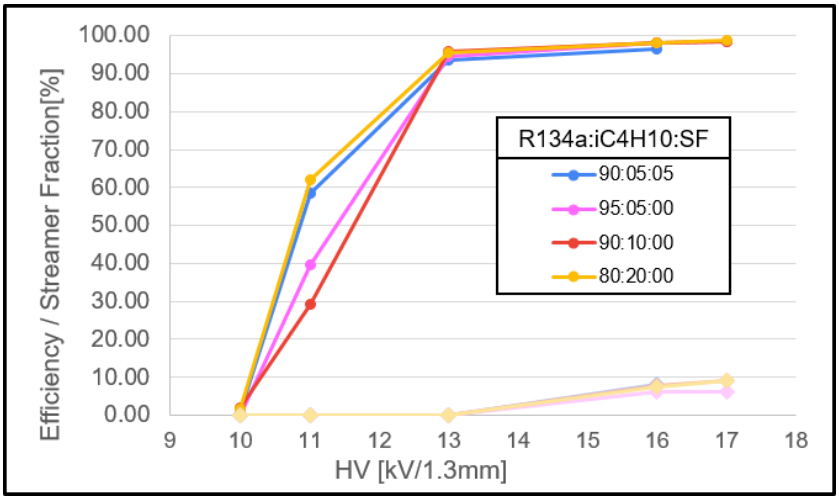

Fig.4. Efficiency Streamer Fraction curve by changing applied HV

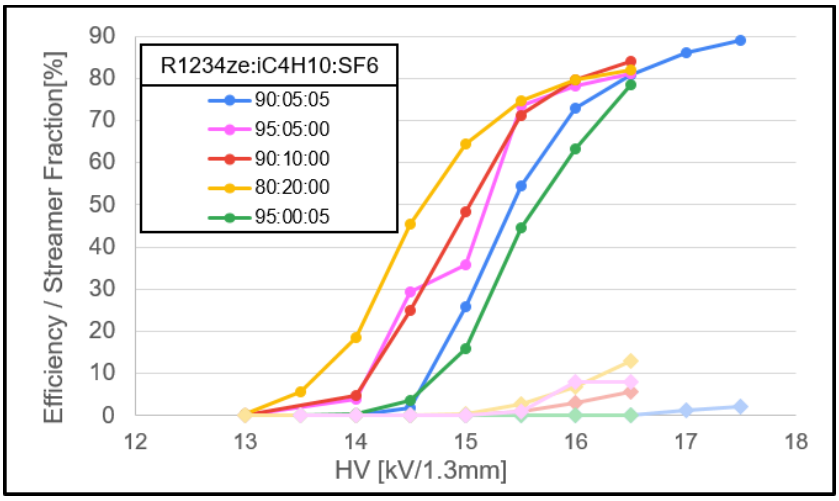

Fig.5. Efficiency Streamer Fraction curve by changing applied HV

tor shows close to 90% efficiency with the best gas mix fraction (R1234ze: iC4H10: SF6 = 90: 5: 5.) with H.V.=17kV. However, the efficiency curve shows that the efficiency did not seem to get in the maximum plateau region. Moreover, the H.V. 17 kV is about 30% higher H.V. than that of R134a operation. Besides, the time resolution for the detector is not tested. Further studies are needed to make a solid conclusion.

Acknowledgment

We are grateful to the all staff members of ELPH for their extensive efforts on the successful operation of the facility. This work is partly supported by the MEXT Grants-in-Aid for Scientific Research on Innovative Areas “Clustering as a window on the hierarchical structure of quantum systems” Group-A02 (18H05402).

References

[1]https://www.jccca.org/chart/chart01_02.html

[2]https://www.jsrae.or.jp/committee/jisedai_R/H30_ProgressR_WG3.pdf

[3]http://www.mihama.com/products/refri/r1234ze.html

(ELPH Experiment : #2916, #2927)

The performance study of the aerogel Cherenkov counter for the LEPS2-solenoid experiment

C. Yoshida[1], A.O. Tokiyasu[1], H. Ohnishi[1], T. Ishikawa[1], M. Miyabe[1], H. Saito[1], J. Takahashi[1], and M. Tsuruta[1]

[1]*Research Center for Electron Photon Science, Tohoku University, Sendai, 982-0826*

We have developed an aerogel Cherenkov counter (AC), which separate a pion and a kaon in the momentum region 1 - 2 GeV/c, for the hadron photoproduction experiment at SPring-8. We measured the reflector dependence and the incident position dependence using a positron beam and estimated the pion detection efficiency and kaon misidentification (misID) probability. We decided to use aluminized mylar for the AC reflector and determined the final design of the AC.

§1. Introduction

We plan to perform the hadron photoproduction experiment at the LEPS2 beamline in SPring-8. The aim of this experiment is to investigate the mechanism of the exotic hadrons, such as penta-quark Θ^+, $\Lambda(1405)$, the K^-pp bound state. Aerogel Cherenkov counter (AC) is one of the key detectors of the LEPS2 solenoid system, and distinguish kaon and pion with high momentum larger than 1 GeV/c. The requirements of AC are as follows.

- to cover the region within a polar angle between 30 to 40 degrees with respect to the beam direction.
- to have pion detection efficiency more than 95%
- to be installed in narrow space ($\sim$ 10 cm)
- to be operated in the magnetic field ($\sim$ 1 T)
- the material budget should be minimized

Considering these requirements above, we designed the prototype detector using aerogel which refractive index is 1.03 as a radiator. For the photon detector, we will use 3 inch fine-mesh Photomultiplier Tube (PMT) to ensure good photon detection performance under the high magnetic field. For the reflector inside the counter, we have multiple choices, i.e., Enhanced Specular Reflector (ESR) or Aluminized mylar. We evaluated the reflector dependence of the pion detection efficiency (efficiency) and kaon misidentification probablity (misID) of the prototype at the #2916 experiment. We constructed 3 type of AC boxes (box1 : ESR, box2 : Aluminized mylar & ESR, box3 : Aluminized mylar) and compared their efficiency and misID. The final version of the detector is shown in Fig.1. At the #2927 experiment, we evaluated the incident position dependence of efficiency and misID precisely. In this report, we show the results of these two test experiments.

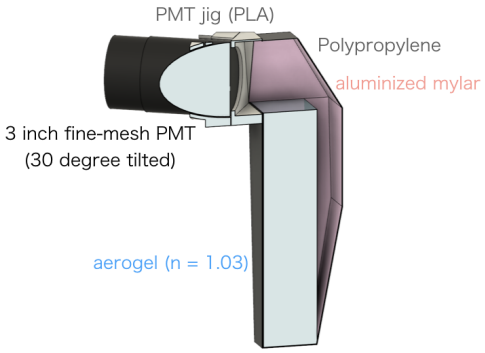

Fig.1. Cross section view of the AC

§2. Experimental Setup

The test experiments #2916 and #2927 were performed at the 30-degree positron beamline in the GeV-γ experimental hall. The setup is shown in Fig.2. 600 MeV positron was used for these experiments. Trigger 1 and Trigger 2 are plastic scintillators. Those size was 10 $\times$ 50 $\times$ 5 $\times$ mm (width $\times$ height $\times$ thickness). They were installed upstream and downstream of AC, respectively. Trigger signal for data taking was produced with the coincidence signal of Trigger1 and Trigger2. We measured the Cherenkov light signal detected with PMT by changing the beam hit position on the AC to study the incident beam position dependence on its performance.

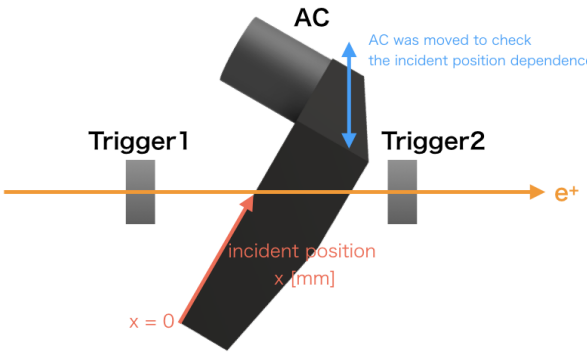

Fig.2. Top view of the setup

§3. Results

3.1 ELPH experiment : #2916

Fig.3 shows the typical charge distribution from the AC when the beam hit on 200 mm from the edge of the AC box. The efficiency and misID probability have been evaluated from the charge distribution of the AC with and without the Cherenkov radiator. The definition of efficiency and misID are as follows.

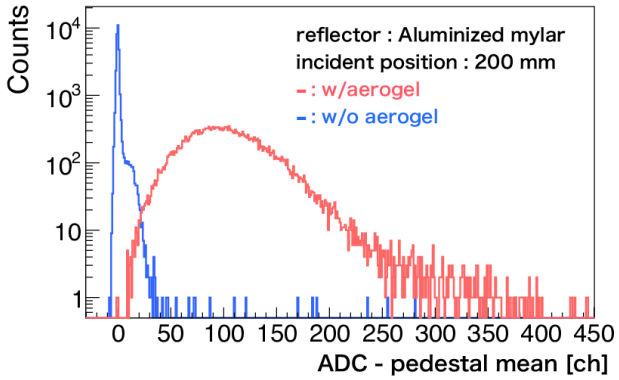

Fig.3. Charge distribution when Aluminized mylar box with incident position 200 mm from the edge of the AC box. Red line is that with aerogel and blue line is that without aerogel.

$$\text{efficiency (w/ aerogel in the AC box)} = \frac{\text{Counts (ADC ch} > \text{threshold)}}{\text{Counts (Trigger)}}$$

$$\text{misID (w/o aerogel in the AC box)} = \frac{\text{Counts (ADC ch} > \text{threshold)}}{\text{Counts (Trigger)}}$$

The threshold value of the above evaluation has determined where the efficiency of the detector exceeds more than 95% at the beam hit position more than 50 mm from the AC box's edge for each AC box. The threshold values in ADC ch are 42 ch, 22 ch and 4 ch for box1, box2 and box, respectively. The incident position dependence of efficiency (red line) and misID (blue line) for each AC are shown in Fig.4. According to Fig.4, the highest misID values are 41%, 12% and 10% for box1, box2 and box3 respectively. From these results, we decided to use aluminized mylar for the AC reflector.

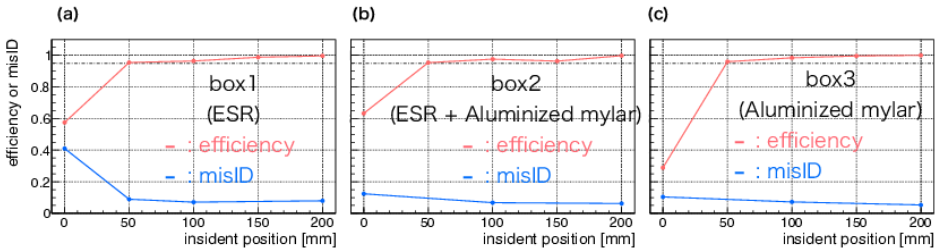

Fig.4. The incident position dependence of efficiency (red line) and misID (blue line) for (a) box1, (b) box2 and (c) box3.

3.2 ELPH experiment : #2927

We evaluated the efficiency and misID of the final version AC box in the same way to #2916. The incident position dependence of efficiency (red dot) and misID (blue dot) are shown in Fig.5. We found that the requirements are satisfied when an incident position is larger than 100 mm.

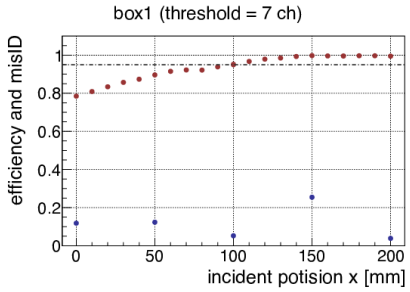

Fig.5. The incident position dependence of efficiency (red dot) and misID (blue dot).

§4. Summary

We evaluated the performance of the aerogel Cherenkov counter (AC) for LEPS2 experiment. At the test experiment #2916, we estimated the reflector dependence of the pion detection efficiency and kaon misID probability. As a result, aluminized mylar is adopted as a reflector for AC. The detector performance with the final configuration had been performed as #2927. In this test experiment, the incident position dependence of the detector was evaluated. We found that the requirements are satisfied when an incident position is larger than 100 mm. Based on the series of experimental results, construction of the AC detectors for LEPS2 was underway.

Acknowledgment

We are grateful to the all staff members of ELPH for their extensive efforts on the successful operation of the facility. This work is partly supported by the MEXT Grants-in-Aid for Scientific Research on Innovative Areas ”Clustering as a window on the hierarchical structure of quantum system” GroupA02(18H05402).

Status of LEPS2-solenoid experiment in 2019

Atsushi Tokiyasu[1], Yuta Sada[1], and LEPS2 collaboration

[1]*Research Center for Electron Photon Science, Tohoku University, Sendai, 982-0826*

The LEPS2-solenoid experiment at SPring-8 is aiming to investigate the hadron photoproduction mechanism. LEPS2 spectrometer system is under preparation; Detectors and data acquisition system are developed, and the performance check of each detector is on-going. In 2019, some new detectors were installed in the spectrometer, and the data with nuclear target was taken for the purpose of the detector calibration. We plan to continue the calibration of the detectors by using the liquid hydrogen target in FY2020.

§1. Overview of LEPS2-solenoid experiment

The LEPS2-solenoid experiment is aiming to study the hadron photoproduction mechanism at SPring-8. A high intensity γ beam by Backward Compton Scattering is used to search for exotic hadron systems like penta-quark Θ^+, the K^-pp bound state, and so on. In addtion, we will investigate the production mechanism of hadrons precisely. We constructed LEPS2 spectrometer system to detect the particles produced from the target. The overview of the LEPS2 spectrometer system is shown in Fig. 1. The LEPS2 spectrometer system is composed of Start Counter(SC), Time Projection Chamber(TPC), Drift Chambers(DCs), Aerogel Cherenkov Counter (AC1, AC2), Resistive Plate Chamber (RPC), and Barrel-γ. These detectors are installed inside solenoid magnet with the strength of 1T, and used to detect both of charged particles and γs from the hadron reactions.

§2. Progress in FY2019

Following the previous year, we continued taking the data for the detector calibration by using a nuclear target made of copper or polyethylene . One of the main progresses in FY2019 is the success at reading all 6 sectors of TPC. We took the calibration data. The tracks were reconstructed, the postion resolution and the drift speed were obtained. The drift speed of TPC was found to be 50 % of nominal value. We investigaed the reson, and found the problem in the drift cage. The broken part of TPC will be repaired, and the calibration data will be taken ealry in FY2020.

In addition, we installed three new detectors in the spectrometer system; Start Counter (Fig. 2-(a)), Barrel RPC (Fig. 2-(b)), Barrel γ (Fig. 2-(b)), 4 th Drift Chamber (Fig. 2-(d)), Aerogel Cherenkov Counter (Fig. 2-(e)), We evaluated the performance of the newly installed detectors. As for the start counter, the time resolution was measured to be approximately 150 ps. This value is enough to separate the RF siganals which are used as the start timing (Fig.3). These results were reported in 75 th JPS

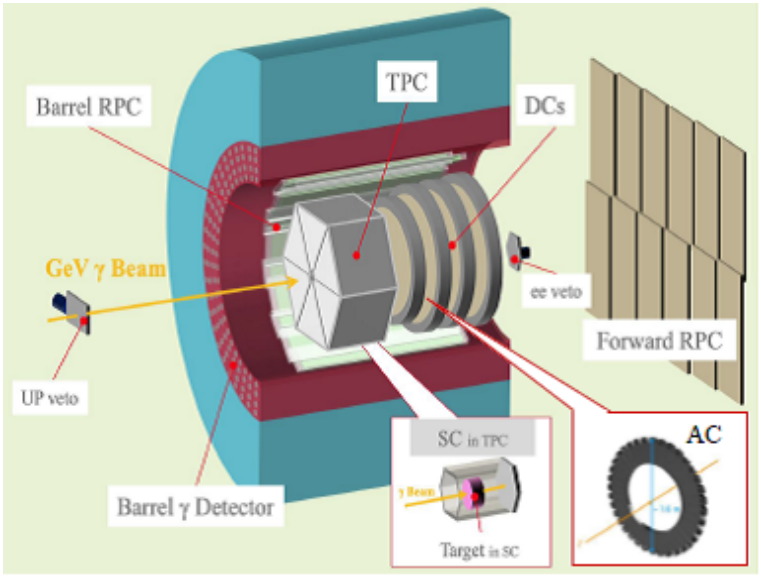

Fig.1. LEPS2 spectrometer system

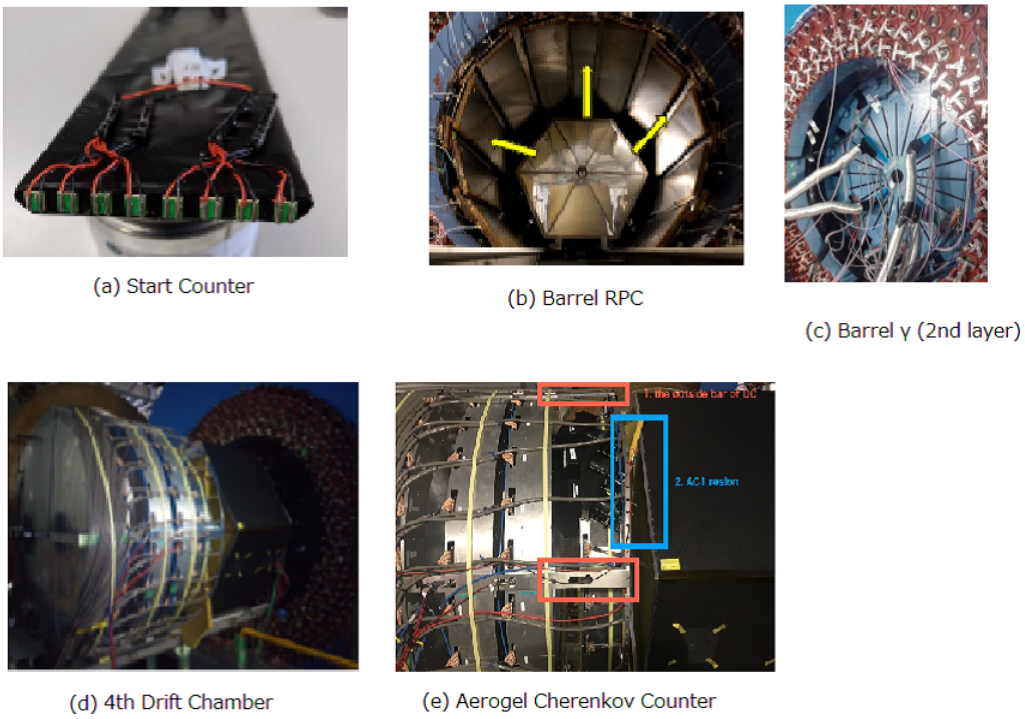

Fig.2. Pictures of newly installed detectors

meeting [1]. As for the Barrel-γ, we prepared the 2nd layer of the calorimeter of 4 layers in total. The

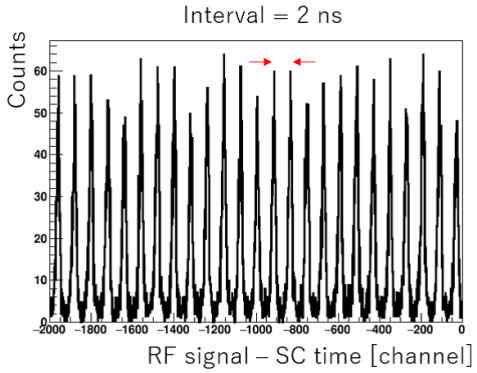

Fig.3. RF signals measured by Start Counter

radiation length is $6.48X_0$. 96 photomultipliers were attached to the end of the calorimenter. The charge information and timing information of the signals were taken together with other detectors of the LEPS2 spectormeter system. The occupancy plots for each layers are shown in Fig. 4. Some channels were found to be broken. Replacement of photomultipliers are on-going. After this work, we will perform the gain tuning for each photmultiplier. The performance of Aerogel Cherenkov Counter was checked by using

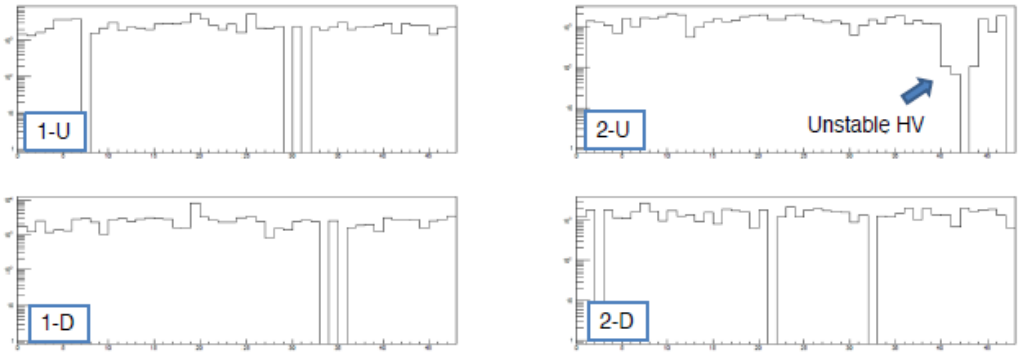

Fig.4. Occupancy plots for Barrel-γ

positron beam at ELPH (Exp No. 2916, 2927). The design was fixed, and three modules were installed in the LEPS2 spectrometer system. The callibration data was taken and the coincidence analysis with other detectors are on-going to evaluate the pariticle identification potential .

§3. Transmission measurement

We measured the transmission of photon-beam at LEPS2 in autumn in 2019. The setup is shown in Fig.5. From upstrteam, an upveto counter to reject the beam halo, a converter to produce e+ e- pair, a start counter to produce the data taking trigger, the beam profile monitor and a Lead Glass calorimeter to measure the photon energy were installed on the LEPS2 beam line. By taking ratio between the

counts of tagger signal and the Lead glass, the value of transmission was obtained. The measured value of transmission is approximately 75 %, which is consistent with the caluclated values. In addition to that, we found that the energy dependance of transmission appear unless the expander condtions are optimized. The simpler detector system is under construction, and will be installed upstream the beam dump in FY2020. This system will be used to check the long-term stability of the photon beam during taking the physics data. These results were reported in the 75 th JPS meeting [3].

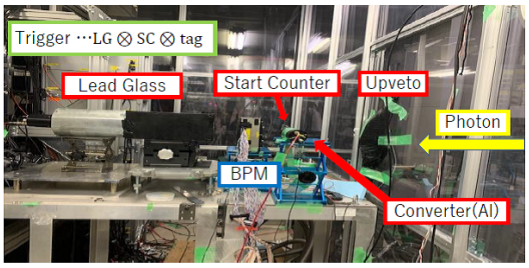

Fig.5. Setup for the transmission measurement

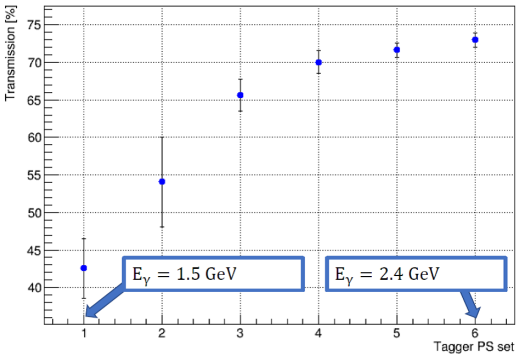

Fig.6. Transmission v.s. Photon Energy

§4. Plans for FY 2020

We will install all main detectors and prepare the data acquisition system in the spectrometer in FY2020. The detector calibration run is shceduled by using liquid hydrogen target. For the stable data acquisition, we develop the beam monitor system now. It will also be installed in FY2020. After taking data for the detector calibration, we start taking physics data.

References

[1] R. Mizuta *et al.*: “Paformance study of trigger counter for LEPS2 spectrometer at SPring-8 ”, JPS Meeting, 19th Mar. 2020, Nagoya Univ.

[2] C. Yoshida *et al.*: “Development of an aerogel Cherenkov counter for the LEPS2 solenoid experiment at SPring-8”, JPS Meeting, 9th Sep. 2019, Yamagata Univ.

[3] H. Saito *et al.*: “Measurement of the transmission at the LEPS2 beamline”, JPS Meeting, 19th Mar. 2020, Nagoya Univ.

Studies for nuclear medium modification of the η' meson mass at the SPring-8 BGOegg experiment

N. Muramatsu[1], N. Tomida[2], Y. Matsumura[2], J.K. Ahn[3], W.C. Chang[4], J.Y. Chen[5], M.L. Chu[4], S. Daté[2], T. Gogami[6], H. Goto[2], H. Hamano[2], T. Hashimoto[2], Q.H. He[7], K. Hicks[8], T. Hiraiwa[9], Y. Honda[1], T. Hotta[2], H. Ikuno[2], Y. Inoue[1], T. Ishikawa[1], I. Jaegle[10], J.M. Jo[3], Y. Kasamatsu[2], H. Katsuragawa[2], S. Kido[1], Y. Kon[2], T. Maruyama[11], S. Masumoto[12], K. Miki[13], M. Miyabe[1], K. Mizutani[10], H. Nagahiro[14,2], T. Nakamura[13], T. Nakano[2], T. Nam[2], T.N.T. Ngan[15], M. Niiyama[16], Y. Nozawa[17], Y. Ohashi[2], H. Ohkuma[2], H. Ohnishi[1], T. Ohta[17], M. Oka[2], M. Okabe[1], K. Ozawa[18], C. Rangacharyulu[19], S.Y. Ryu[2], Y. Sada[1], T. Shibukawa[12], H. Shimizu[1], R. Shirai[1], K. Shiraishi[1], E.A. Strokovsky[20,2], Y. Sugaya[2], M. Sumihama[13,2], S. Suzuki[21], S. Tanaka[2], Y. Taniguchi[1], A. Tokiyasu[1], Y. Tsuchikawa[22], T. Ueda[1], H. Yamazaki[23], R. Yamazaki[1], Y. Yanai[2], T. Yorita[2], C. Yoshida[1], and M. Yosoi[2]

[1]*Research Center for Electron Photon Science, Tohoku University, Sendai, Miyagi 982-0826, Japan*
[2]*Research Center for Nuclear Physics, Osaka University, Ibaraki, Osaka 567-0047, Japan*
[3]*Department of Physics, Korea University, Seoul 02841, Republic of Korea*
[4]*Institute of Physics, Academia Sinica, Taipei 11529, Taiwan*
[5]*National Synchrotron Radiation Research Center, Hsinchu 30076, Taiwan*
[6]*Department of Physics, Kyoto University, Kyoto 606-8502, Japan*
[7]*Department of Nuclear Science & Engineering, College of Material Science and Technology, Nanjing University of Aeronautics and Astronautics, Nanjing 210016, China*
[8]*Department of Physics and Astronomy, Ohio University, Athens, OH 45701, USA*
[9]*RIKEN SPring-8 Center, Sayo, Hyogo 679-5148, Japan*
[10]*Thomas Jefferson National Accelerator Facility, Newport News, Virginia 23606, USA*
[11]*College of Bioresource Sciences, Nihon University, Fujisawa, Kanagawa 252-8510, Japan*
[12]*Department of Physics, University of Tokyo, Tokyo 113-0033, Japan*
[13]*Department of Education, Gifu University, Gifu 501-1193, Japan*
[14]*Department of Physics, Nara Women's University, Nara 630-8506, Japan*
[15]*Nuclear Physics Department, University of Science, Vietnam National University, Ho Chi Minh City, Vietnam*
[16]*Department of Physics, Kyoto Sangyo University, Kyoto 603-8555, Japan*
[17]*Department of Radiology, The University of Tokyo Hospital, Tokyo 113-8655, Japan*
[18]*Institute of Particle and Nuclear Studies, High Energy Accelerator Research Organization (KEK), Tsukuba, Ibaraki 305-0801, Japan*
[19]*Department of Physics and Engineering Physics, University of Saskatchewan, Saskatoon, SK S7N 5E2, Canada*
[20]*Laboratory of High Energy Physics, Joint Institute for Nuclear Research, Dubna, Moscow Region, 142281, Russia*
[21]*Japan Synchrotron Radiation Research Institute (SPring-8), Sayo, Hyogo 679-5198, Japan*
[22]*J-PARC Center, Japan Atomic Energy Agency, Tokai, Ibaraki 319-1195, Japan*
[23]*Radiation Science Center, High Energy Accelerator Research Organization (KEK), Tokai, Ibaraki 319-1195, Japan*

§1. Introduction

The BGOegg experiment, studying the nature of hadrons through the photoproduction of them, is carried out at the SPring-8 LEPS2 beamline, where a linearly polarized photon beam is available in the energy range of $1.3 - 2.4$ GeV. We have constructed a large acceptance electromagnetic calorimeter, called "BGOegg", and set it up with several charged-particle detectors at the LEPS2 experimental building. The BGOegg calorimeter covers a polar angle range from 24° to 144° with 1320 $Bi_4Ge_3O_{12}$ (BGO) crystals, providing the world-best energy resolution of 1.3% for a 1-GeV γ ray. In the experimental programs using a liquid hydrogen target, excited baryon resonances are searched for in the s-channel of neutral-meson photoproduction processes. So far, differential cross sections and photon beam asymmetries have been measured for the photoproduction of π^0, η, and ω mesons, which finally decay into a few γ's [1, 2].

As main physics programs of the BGOegg experiment, we also study nuclear medium modification of the η'-meson mass by using a 20-mm-thick carbon target. Spontaneous breaking of the chiral symmetry is considered to be partially restored at the nuclear density, and an η' mass reduction of $40 - 150$ MeV is predicted by several hadron models with effective QCD Lagrangians [3–5]. In order to search for signals of the η' mass reduction, we have proceeded with two independent analyses: In one method, nuclear bound states of η' mesons have been searched for by a missing mass spectroscopy with forward high-momentum protons. If the reduction of the η' mass is large inside a nucleus, such a bound state can be formed with a large optical potential. In contrast, the other analysis has performed direct measurement of a $\gamma\gamma$ invariant mass spectrum from the η' decays inside a nucleus. This method is sensitive to the case of a smaller mass reduction.

§2. Search for η' bound nuclei

The search for the η' bound nuclei was conducted in the $^{12}C(\gamma, p)$ reaction by detecting a forward proton at the resistive plate chamber (RPC) wall, which was located 12.5 m downstream of the carbon target with a polar angle coverage up to 6.8° [6]. The time-of-flight of a charged track was measured with a time resolution of $60 - 90$ ps, and translated to a momentum by assuming the detected track should be a proton. If η' bound signals exist, they must appear below the production threshold in the proton missing mass spectrum. Because there remain a lot of background events in such a spectrum, the BGOegg experiment has, for the first time, required the simultaneous detection of conversion signals by bound η' mesons and nucleons (N's), namely the reaction $\eta' N \to \eta N$, followed by the $\eta \to \gamma\gamma$ decay.

Black dots in Fig. 1 show the excitation energies $E_{ex} - E_0$ (missing masses relative to the η' production threshold) and η emission angles $\cos(\eta)$ (polar angles in the Lab frame) of the real data events after requiring the dection of an η meson, decaying into $\gamma\gamma$, and a slow proton (p_s) at the BGOegg calorimeter. Unfortunately, this sample was still dominated by backgrounds mainly due to the η photoproduction, where the secondary interactions of primary products made additional slow protons. Therefore, we further developed kinematical cuts by requiring the back-to-back nature of the η and p_s pair, omitting boosted events with very forward production of either η or p_s, and so on. Here the cut conditions were

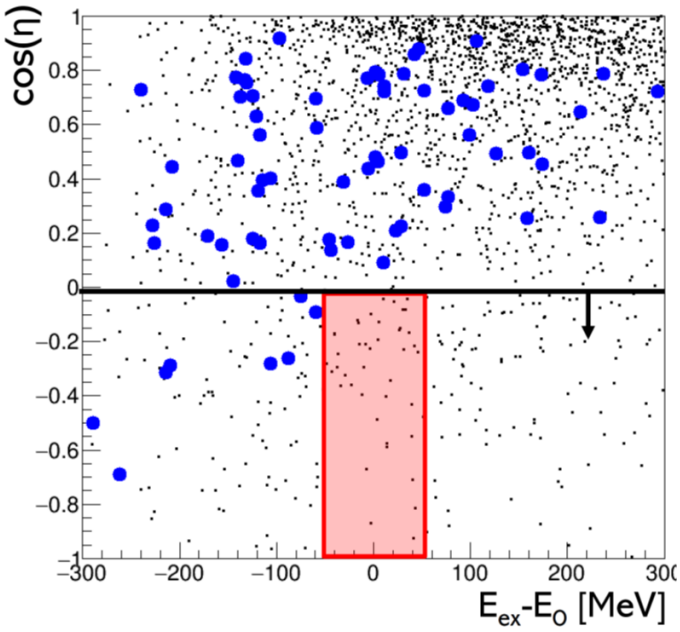

Fig.1. A two-dimensional plot of the η polar angle versus the excitation energy for signal samples of the η' bound nuclei search [7]. The red shaded area indicates a signal search region.

optimized without examining the predetermined signal region, indicated by a red shaded area in Fig. 1. Finally, only events shown by blue circles survived after applying the kinematical cuts, and no events were observed in the signal region. Based on this fact, we determined an upper limit for the production of η' bound nuclei with an η-p_s pair to be 2.2 nb/sr (90% confidence level) at the opening angles $\cos(\eta p_s) < -0.9$.

We comapared this upper limit of the production cross section with a theoretical calculation using distorted wave impulse approximation (DWIA) and assumption of a few optical-potential values [8]. In the process of the comparison, we normalized the theoretical calculation by using the observed amount of quasi-free η' photoproduction events. This was essential to remove ambiguities in the DWIA calculation. As a result, we have obtained an indication that a large optical potential (V_0) is not favored because a branching fraction of the one-nucleon absorption process (the $\eta' N \rightarrow \eta N$ conversion) is unnaturally limited below 24% in the case of $V_0 = -100$ MeV.

§3. Direct measurement of the η' mass spectrum

In the BGOegg experiment, an alternative analysis method to obtain a hint of the η'-mass reduction at the nuclear density was also adopted by measuring a distibution of $\gamma\gamma$ invariant masses ($M_{\gamma\gamma}$'s), calculated from the energies and hit positions of two γ-rays at the BGOegg calorimeter [9]. A γ-ray hit was reconstructed by clustering neighboring BGO crystals with energy deposit and by confirming no charge hit at a corresponding inner hodoscope. Overlap of two particle hits in a reconstructed cluster was identified based on the properties related to a cluster shape and shower-energy distribution. No hits except for the two γ-rays and a charged track, which may be a proton, were allowed to select the final

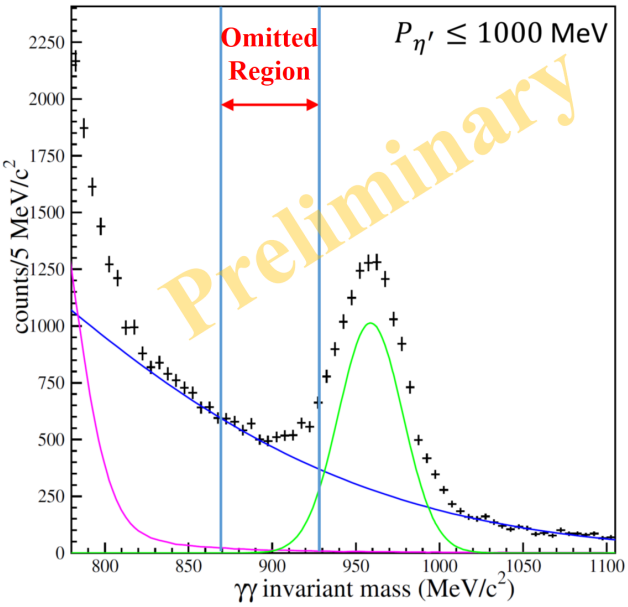

Fig.2. A spectrum of $\gamma\gamma$ invariant mass for the momentum range below 1 GeV/c in the carbon target data [10]. Background functions are fitted by using the data points outside the vertical blue lines.

sample.

Figure 2 shows a preliminary result of the $\gamma\gamma$ invariant mass spectrum in the case that the momentum of a $\gamma\gamma$ system is required to be lower than 1 GeV/c. This condition was introduced to increase a fraction of the decays inside a nucleus, and determined by a simulation so that a statistical significance of possible signals should be most enhanced. Background functions to be fitted were prepared for the photoproduction processes of quasi-free η' mesons (the green line), multiple π^0 mesons (the blue line), and ω mesons (the purple line), as shown in Fig. 2. The latter two processes become backgrounds when one or a few γ-rays escape from the forward acceptance hole of the BGOegg calorimeter ($\theta < 24^\circ$). Justification of these functions were carefully examined by using the real data and the MC simulation.

While background-function fits to the higher-momentum sample ($P_{\eta'} > 1$ GeV/c) and the liquid-hydrogen-target sample show reasonable χ^2 values, the same fitting method for the lower-momentum sample ($P_{\eta'} < 1$ GeV/c) returns a larger χ^2 value. Therefore, we fitted the background functions not by using the data points in a mass range, where an increase of events was seen. In the case of Fig. 2, a range of $870 < M_{\gamma\gamma} < 930$ MeV/c^2 was omitted from the fit, and a statistical significance of the excess over a sum of the fitted background functions was estimated to be 3.6σ in the omitted mass range. Such a significance is also being obtained by a χ^2 difference test, which compares two fits: one using only background functions and the other using the same background functions and a signal function, simulated by taking into account a density distribution inside a nucleus. Although it is hard to conclude the existence of η'-mass reduction due to the insufficient statistics, an amount of the reduction can be anyway evaluated from a fit with the signal function which provides the maximum significance. A mass value of the possible excess does not contradict the first result from the η' bound nuclei search, which

indicates the optical potential does not exceed about 100 MeV. Now various systematic uncertainties for the spectral line shape of the reconstructed η' mass are also being examined.

§4. Prospect

We are going to confirm the two analysis results by an additional data, which has been collected with a carbon target and whose statistics is similar to the analyzed data. In addition, we plan the next-phase BGOegg experiment with the setup dedicated to the direct measurement of the $\gamma\gamma$ spectrum with a target made of copper, whose nuclear radius is 1.8 times larger than that of carbon, and a forward γ detector, composed of 252 PWO crystals and covering the acceptance hole of the BGOegg calorimeter. Backgrounds from multiple meson photoproduction will be more than one order of magnitude reduced by almost the 4π coverage of electromagnetic calorimeters. A sensitivity of signal detection is expected to increase significantly.

References

[1] N. Muramatsu *et al.*: Phys. Rev. C **100** (2019) 055202.

[2] N. Muramatsu *et al.*: Phys. Rev. C **102** (2020) 025201.

[3] H. Nagahiro, M. Takizawa, and S. Hirenzaki: Phys. Rev. C **74** (2006) 045203.

[4] S. Sakai and D. Jido: Phys. Rev. C **88** (2013) 064906.

[5] S.D. Bass and A.W. Thomas: Phys. Lett. B **634** (2006) 368.

[6] N. Tomida, N. Muramatsu, M. Niiyama *et al.*: Phys. Rev. Lett. **124** (2020) 202501.

[7] N. Tomida: 5th CLUSTER Workshop, 25 Sep 2020.

[8] H. Nagahiro: J. Phys. Soc. Jpn. Conf. Proc. **13** (2017) 010010.

[9] Y. Matsumura, H. Shimizu, N. Muramatsu *et al.*: 75th JPS meeting (2020) 17aK15-2.

[10] Y. Matsumura: Doctoral Thesis (in preparation), Tohoku Univ.

3D magnetic field mesurement of SCRIT electron spectrometer

H. Wauke[1], H. Honda[1], T. Suda[1], D. Taki[1], and K. Tsukada[1,2]

[1]*Research Center for Electron Photon Science, Tohoku University, Sendai, 982-0826*
[2]*Institute for Chemical Research, Kyoto University, Uji, 611-0011*

The 3D magnetic field measurement of the SCRIT electron spectrometer was performed with accuracy of $\Delta B/B \sim 10^{-3}$ in November 2019, aiming at improving the momentum resolution of the spectrometer. The measured magnetic field distributions are similar to these of the calculated ones and their differences were found to be $\sim 10^{-3}$ T. The electron scattering experiments using carbon targets were performed to compare the momentum resolutions derived using the calculated maps and the measured ones.

§1. Introduction

The SCRIT (Self–Confining Radioactive–isotope Ion Target) [1, 2] electron scattering facility has been built at RIKEN RI beam factory for electron scattering off unstable nuclei. WiSES (Window–frame Spectrometer for Electron Scattering) is an electron spectrometer for the SCRIT experiment. WiSES consists of a dipole magnet, two drift chambers placed at the entrance and exit of the magnet, a helium bag installed between the two drift chambers to reduce the multiple scattering effect, and two scintillation counters for trigger generation. The solid angle of the spectrometer is about 80 msr, covering a wide range of scattering angles, i.e. from 30° to 60°. The WiSES gap has a size of 1700 (width) × 290 (height) × 1400 (depth) mm^3 to obtain high statistics for low luminosity. A momentum resolution of $\Delta p/p \sim 10^{-3}$ is required to separate elastic and inelastic scattering with WiSES for an electron energy in the range of 150–300 MeV. The momentum resolution evaluated in past elastic scattering experiments was found not to reach the design value. One possible season is that the map calculated using OPERA3D to reconstruct the trajectories of the scattered electrons does not reproduced the WiSES magnetic field with enough accuracy. In this paper, the results of the 3D magnetic field measurement of the magnet and the performance study of the WiSES are reported.

§2. 3D magnetic field measurement

The 3D magnetic field measurement of WiSES with the measured accuracy $\Delta B/B \sim 10^{-3}$ was carried out. The magnetic field strength was 0.4–0.8 T, which corresponds to the experiments with the electron beam energy of 150–300 MeV. Figure 1 shows the 3D magnetic field measurement system. A probe head made from three Hall probes and a 3D driving device consisting of three electric sliders that move in a large measurement area (500 (width) × 300 (height) × 850(depth) mm^3) were developed. The

probe head can be measure three magnetic field components simultaneously. The measurement resolution of these probes is about 10^{-6} T. The 3D driving device was controlled by the LabVIEW program to be measured in steps of at ~10 mm intervals. The program also reads the field values from the Hall probes and the absolute magnetic field of the WiSES magnet is continuously normalized by using nuclear magnetic resonance (NMR).

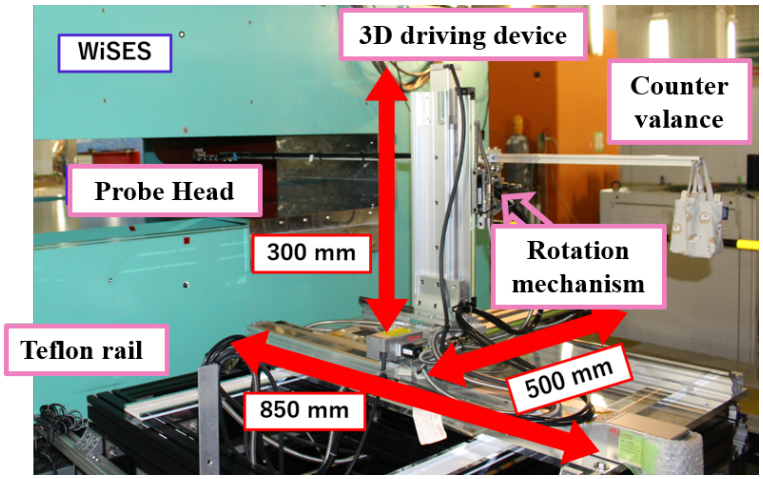

Fig.1. The 3D magnetic field measurement of WiSES system.

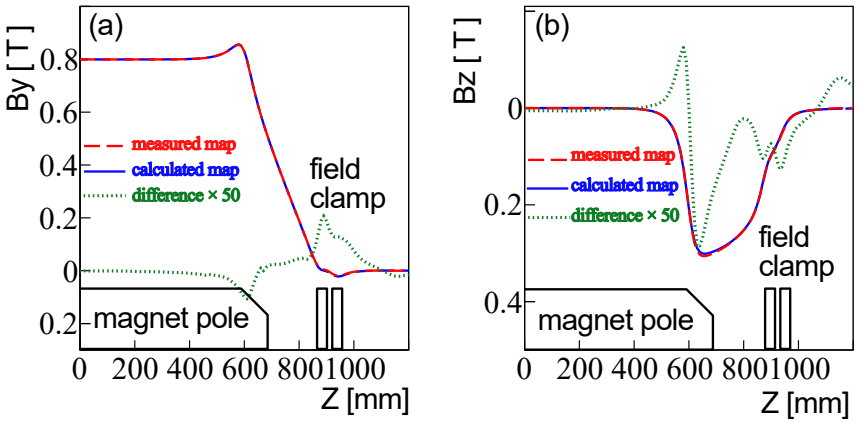

Fig.2. Comparison between the measured map and the calculated one near the magnetic pole. The strength of the magnetic field was 0.8 T. (a) shows vertical component B_y and (b) shows horizontal component of the fringing field B_z. The red line is the measured map, blue line is the calculated one, and green line shows 50 times the difference between the two maps.

Figure 2 shows the vertical component B_y and the horizontal component of the fringing field B_z of the measured map and the calculated one. The structure of the measured magnetic field agrees will to the calculated one even at about 1 cm from the magnet pole. Over the entire measurement area, their differences are order of ~10^{-3} T. Similar results were obtained for other magnetic field strengths.

§3. Performance study

In November 2019, it was investigated by electron scattering with carbon targets whether the differences of the calculated maps and the measured ones affects the momentum resolution. The momentum resolution is obtained from the width of the elastic scattering peak observed in the experiments. The resolution was obtained using the measured maps and the calculated maps.

Figure 3 shows the result, ϕ is the azimuth angle of the scattered electrons as viewed from the target. At three electron energies, namely 150, 200 and 300 MeV, the momentum resolutions obtained from the measured map in this study agree well with those that obtained from the calculated one.

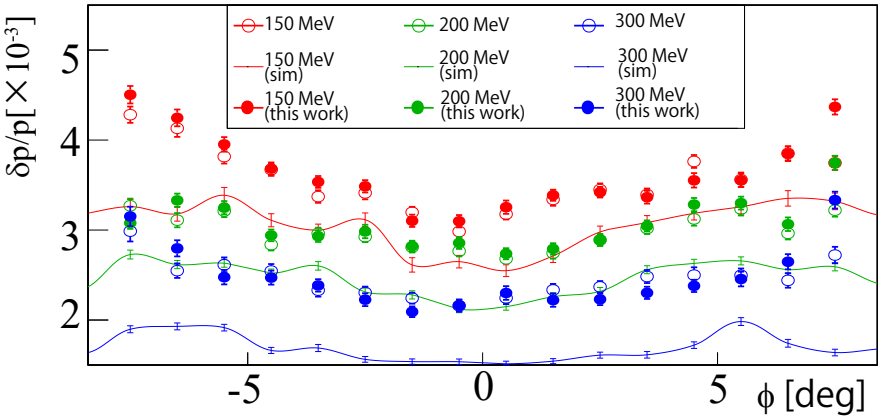

Fig.3. Comparison of the momentum resolution between the measured map and the calculated one. The solid lines show the simulation results, the open circles show the results obtained with the calculation map, and the filled circles show the results obtained with the measured map. Red indicates the results with 150 MeV, green indicates the results with 200 MeV, and blue indicates the results with 300 MeV.

§4. Conclusion and future

WiSES is an electronic spectrometer for SCRIT experiments. In order to improve the momentum resolution of WiSES, the 3D magnetic field distributions with the magnetic field strengths corresponding to the energy (150–300 MeV) used in the experiment was measured. As a result, the structure of the magnetic field distributions measured at the magnetic field strength of 0.4–0.8 T were similar to the calculated ones, with the differences of 10^{-3} T over the entire measurement area. An electron scattering experiment using carbon targets was conducted to confirm the effect of the momentum resolution due to the above differences, but there were almost no differences from the ones obtained from the simulation.

Further study to account for the difference of the WiSES momentum resolution between the simulated and experimental values is still ongoing.

References

[1] M. Wakasugi *et al.,* Phys. Rev. Lett. **100**, 164801 (2008).

[2] K. Tsukada *et al.,* ELPH Annual Report 2014 Vol. 5, Tohoku University, 125 (2014).

[3] K. Tsukada *et al.,* ELPH Annual Report 2018 Vol. 7, Tohoku University, 81 (2018).

(ELPH Experiment : #2879)

The position and profile measurement of the positron beam line at ELPH

M. Miyabe[1], M. Okabe[1], Y. Sada[1], H. Saito[1], J. Takahashi[1], M. Tsuruta[1], C. Yoshida[1], and GeV-γ group[1]

[1]*Research Center for Electron Photon Science, Tohoku University, Sendai, 982-0826, Japan*

In the GeV-γ experimental hall of Research Center for the Electron PHoton Science (ELPH), The positrons and electrons, which are produced at a metal plate in front of the bending magnet $\mathcal{R}$TAGX by bremsstrahlung photon beam generated from the electron storage ring, are provided at three beamlines. The positron beamline is guided in the 30 degree direction from the $\mathcal{R}$TAGX dipole magnet. It is used for detector performance evaluation experiments with 50 MeV to 800 MeV positron. Positron beamline is suspected that the beam is slightly downward with respect to the reference height of the GeV-γ Experimental hall, and past experimental results show a similar tendency. We don't understand why the beam direction is not horizontal, but the direction of the gamma beam or the alignment of the $\mathcal{R}$TAGX magnet are considered as a possibility. In this experiment, the beam profile is measured at two points on the positron beamline and the orbit of the positron beam was measured.

§1. Introduction

The positrons and electrons, which are produced at a gold or tungsten or brass plate as a converter in front of the bending magnet $\mathcal{R}$TAGX by the photon beam, are provided at three beamlines in the GeV-γ experimental hall. The generated positrons are momentum-analyzed by the $\mathcal{R}$TAGX dipole magnet and guided in the 30 degree direction with respect to the photon beamline. The momentum of positrons is selected by the current of $\mathcal{R}$TAGX and transported to the beamline. The positron beam is used for detector performance evaluation experiments. In addition, the triplet quadrupole magnets RFQ for positron beamline is installed to focus the beam. Especially, it is effective when using a low-energy positron beam.

From the results of some experiments, the positron beam direction is slightly downward with respect to the reference height of the GeV-γ experimental hall. The purpose of this experiment is to accurately measure the beam trajectory. We don't understand the reason why the beam direction is not horizontal, but the direction of the gamma beam, the alignment of the $\mathcal{R}$TAGX magnet, etc. are considered as a cause. In this experiment, a new position detector using scintirating fibers and MPPCs was manufactured. By measuring the beam shape at two points on the beamline at the same time, the shape and direction of the positron beam at each point can be measured. We investigate a cause from results of these measurement. In addition, the new position detector is used as an online beam monitor for shared-use at a positron beamline.

§2. Experimental setup and results

The experiment was carried out in June 2019 at the positron beamline in the GeV-γ experiment hall at Research Center for Electron PHoton Science (ELPH). Initially we planned to install two beam profile monitors (BPM) for beam shape measurement at two locations on the beamline and measure the beam trajectory at the same time. Unfortunately, when the newly created νBPM consisting of 50 channels of 1 mm square fiber is installed in the positron beamline, Since the NIM-EASIROC used for readout signals did not work due to the noise, simultaneous measurement at two points was abandoned. In this report, only one BPM (eBPM) was installed at two different places on the positron beamline. The beam orbits were obtained by the twice measurement by different setup. The experimental setup is shown in Figures 1 and 2.

The eBPM is consisted of 32 channels of 3 mm square scintirating fibers and two layers. eBPM detects

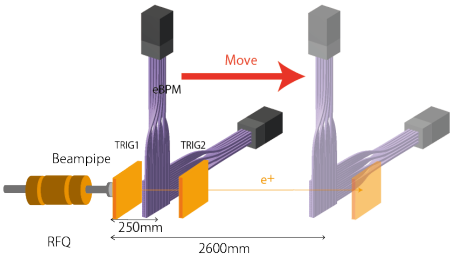

Fig.1. Schematic drawings of the experimental setup.

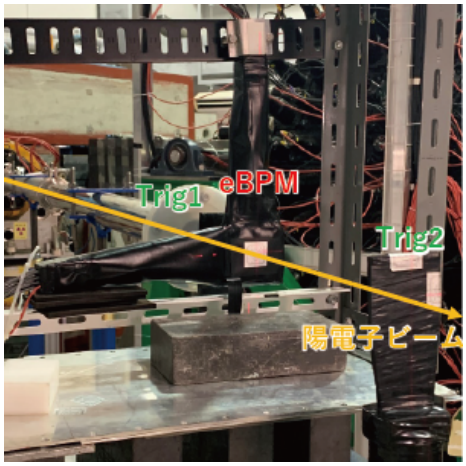

Fig.2. Experimental setup photograph from downstream.

the position of each x and y positron beam. 5 mm thick plastic scintillators were installed at upstream and downstream of eBPM (TRIG1,TRIG2). (TRIG1, TRIG2) generated the trigger signal with eBPM . Positron beam momentum was selected while changing the current value of $\mathcal{R}$TAGX from 100 A to 400 A The beam position and shape were measured at two points, 250 mm and 2600 mm, from the beam pipe of the positron beamline. Figure 3 shows The beam shape when the current value of $\mathcal{R}$TAGX is 300 A. The obtained beam shape is projected on each of the x and y axes and fitted with a Gaussian distribution. The center value ($\mu_{x,y}$) and width ($\sigma_{x,y}$) of the beam were shown in Fig. 4. Tables 1 and 2 show a list of the center values and widths of the beams obtained for each $\mathcal{R}$TAGX current value. Figure 5 shows the orbit of the positron beam. Obtained results show that the beam center shifts in the + x and + y directions as the current value increases. It was also found that the width of the beam was the maximum value (σ_x,

σ_y) = (25.3, 18.9) mm at 2600 mm downstream.

Table 1. center value and width of the positron beam at 250 mm downstream from beam pipe

$\mathcal{R}$TAGX current [A]	μ_x	σ_x	μ_y	σ_y
100	2.2	18.3	0.0	10.1
230	2.5	16.4	0.7	9.5
300	3.2	16.0	1.1	9.2
400	4.5	15.9	1.6	9.1

Table 2. center value and width of the positron beam at 2600 mm downstream from beam pipe

$\mathcal{R}$TAGX current [A]	μ_x	σ_x	μ_y	σ_y
100	3.5	25.3	-0.97	18.9
230	4.4	24.5	0.67	14.4
300	5.2	23.0	0.91	13.5
400	8.2	22.9	2.3	12.6

§3. Summary

This time, the beam profile measurement of the positron beamline at Research Center for Electron PHoton Science, Tohoku University. At first, it was planned to measure the beam shape at two points on the beam line at the same time, but the prepared detector did not work correctly, therefore, the similar detector eBPM was used to measure two points independently. As a result, it was found that the positron beam size spreads up to about 25 mm at the downstream. Also, we found that the center of the orbit deviates depending on $\mathcal{R}$TAGX current value. In the Next experiment, we improve the νBPM readout system and perform the simultaneous measurement at two locations on the positron beamline. And we also measure the effect of the RFQ magnet. (Adopted ELPH#2932).

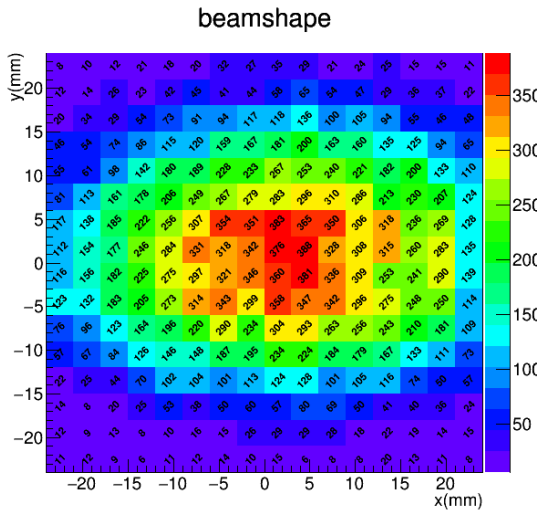

Fig.3. positron beam shape at 250mm downstream from beam pipe with $\mathcal{R}$TAGX current is 300 A

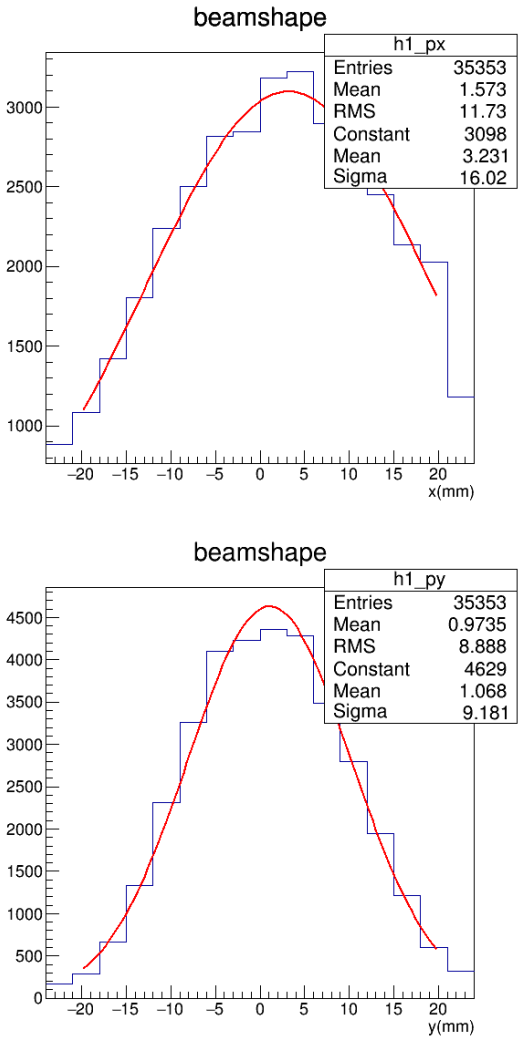

Fig.4. X (upper) and Y (lower) direction projected beam shape

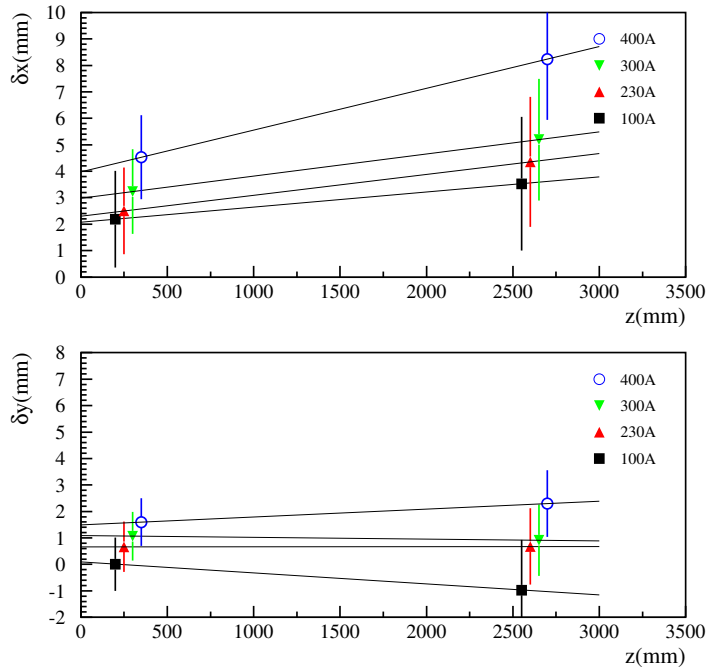

Fig.5. Obtained trajectory of the positron beam. center value and width in x direction (upper), y direction (lower). Error bar shows the 10 times value of the width.

(ELPH Experiment : #2919, #2936)

Development of a spectrometer for ULQ2 experiment

Y. Honda[1], T. Aoyagi[1], C. Legris[1], T. Goke[1], K. Ishizaki[1], H. Kikunaga[1], Y. Maeda[2], S. Miura[1], M. Miyabe[1], T. Muto[1], K. Namba[1], K. Nanbu[1], S. Sasaki[3], T. Suda[1], K. Takahashi[1], S. Takayama[1], D. Taki[1], T. Tamae[1], A. O. Tokiyasu[1], K. Tsukada[4], N. Tsukamoto[3], H. Wauke[1], and Z. Hang[2]

[1]*Research Center for Electron Photon Science (ELPH), Tohoku University, Sendai, 982-0826, Japan*

[2]*Faculty of Engineering, University of Miyazaki, Miyazaki, 889-2192, Japan*

[3]*Department of Physics, Tohoku University, Sendai, 980-8578, Japan*

[4]*, Institute for Chemical Research, Kyoto University, Uji, 611-0011, Japan*

Proton charge radius has a serious inconsistency since 2010. ULQ2 (Ultra Low Q^2) experiment aims to determine the proton radius with low-energy electron scattering as small model dependence as possible. We have developed a new spectrometer for the ULQ2 experiment. The spectrometer is designed to measure momentum and scattering angle of electrons from a position on the focal plane detector due to a difficulty of a tracking of a low-energy electron. The designed spectrometer satisfies experimental requests such as momentum resolution, angular resolution, and acceptance. The spectrometer has been constructed in the first experimental hall of ELPH in March 2019 . A commissioning of the spectrometer and beam line are planed in 2020.

§1. Introduction

Proton charge radius has a serious inconsistency since 2010. Until 2020, the proton charge radius was thought to be 0.8775(51) fm [1], based on the measurements with electron scattering and hydrogen spectroscopy. However, the radius measured with muonic hydrogen spectroscopy was reported as 0.84184(67) fm [2] which is 7σ smaller from the previously accepted result. That is called proton radius puzzle. Until now, the radius has been newly measured with hydrogen spectroscopy and electron scattering, but the result is divided into around 0.84 and 0.88 fm. [3–6] The puzzle is getting more confused.

ULQ2 (Ultra Low Q^2) experiment is aiming at determining the proton radius with the electron scattering with removing model dependence as much as possible. The features of the ULQ2 experiment are as follows : absolute cross section measurement with high accuracy of 10^{-3}, measurement at low momentum transfer region of $0.0003 \geq Q^2 \geq 0.008$ (GeV/c)^2, and experimental separation of charge and magnetic form factor (Rosenbluth separation). In this report, we report on a development of a spectrometer for the ULQ2 experiment.

§2. Spectrometer development

We have developed a new spectrometer for ULQ2 experiment. The spectrometer is designed to measure momentum and scattering angle of electrons from a position on the focal plane detector due to a difficulty of a tracking of a low-energy electron. Due to the limitation of the space and budget, the spectrometer has a simple configuration consisting of a dipole magnet and focal plane detectors. A two dimensional position sensitive detector is installed on the focal plane of the dipole magnet, and the momentum and scattering angle are determined from the detected position instead of the tracking. From the experimental request, we aimed for momentum resolution of $\sigma_p/p \leq 10^{-3}$, scattering angle resolution of $\sigma_\theta \leq 5$ mrad, and acceptance solid angle of $\Omega \geq 10$ mSr.

We used Orbit4 [7] to design the spectrometer. We calculated magnet shape which maximizes resolutions and acceptance under conditions that the distance between target and entrance of the magnet L_1 is 500 mm, curvature of radius ρ is 500 mm, bending angle θ_b is 90°, and gap of the pole piece d is 70 mm. The calculated transfer matrices are summarized in table 1.

Table 1. Summary of the transfer matrix of the spectrometer

	x	ϕ	δ	xx	xϕ	xδ	$\phi\phi$	$\phi\delta$
x	-0.31127	0.00001	0.59764	-0.16839	0.14443	2.85170	-0.00147	1.68857
ϕ	-5.27612	-3.22143	0.19172	11.37759	3.34719	0.46984	-1.65686	-0.61295
	$\delta\delta$	yy	yθ	$\theta\theta$	xxx	xxϕ	xxδ	x$\phi\phi$
x	-0.35319	-0.34478	-0.47833	-0.32271	-35.67131	-63.05219	4.25015	-35.82395
ϕ	-0.62332	-0.40122	-3.50290	1.34522	-91.54606	-80.28996	6.33960	-25.54731
	x$\phi\delta$	x$\delta\delta$	xyy	xyθ	x$\theta\theta$	$\phi\phi\phi$	$\phi\phi\delta$	$\phi\delta\delta$
x	10.19699	-1.95559	-24.38432	7.68791	-2.26485	-6.58477	4.35684	-0.88163
ϕ	6.24398	-5.01064	550.34503	557.04736	117.57027	-3.89761	0.99549	-3.37141
	ϕyy	ϕyθ	$\phi\theta\theta$	$\delta\delta\delta$	δyy	δyθ	$\delta\theta\theta$	
x	2.91029	20.65081	2.49754	0.33039	-0.70422	-5.04930	-1.16769	
ϕ	150.26016	118.15029	14.07843	0.15148	45.53897	39.45752	18.25986	
	y	θ	yx	yϕ	yδ	θx	$\theta\phi$	$\theta\delta$
y	-1.99660	0.85339	48.29457	8.53570	4.72331	14.90802	-0.00066	2.96383
θ	-3.15227	0.84649	62.24168	10.44631	5.31752	17.40900	-0.84716	4.40906

After the Orbit4 calculation, we check the consistency of the transfer matrix from Orbit4 and from electron's trajectory calculation with magnetic field calculated by TOSCA [8]. As a result of that, we found small inconsistency of $(y|\theta)$ which is mainly controlled by the angle of the entrance and exit of the magnet, β. Therefore, we make smaller the angle of the entrance by 8° so that the $(y|\phi)$ from the trajectory calculation is the same as one from Orbit4. The difference seems to be due to the fact that the shape of the fringing magnetic field is not completely introduced. Finally, we got the spectrometer's configuration as shown in table 2.

The shape of the entrance and exit of the magnet is designed to maximize the resolutions and acceptance. Figure 2 shows the lay-out of the spectrometer. The shape of the entrance and exit of the

Table 2. Summary of the configuration of the spectrometer

Target to Entrance	L_1 500 mm			
Magnet	ρ 500 mm	θ_b 90°	d 70 mm	
Entrance shape	a_1 -856.77	a_2 0	β 51.267°	l 36.2 mm
Exit shape	a_1 404.23	a_2 79514	β 37.495°	l -34.4 mm
Exit to Detector	L_2 440 mm			

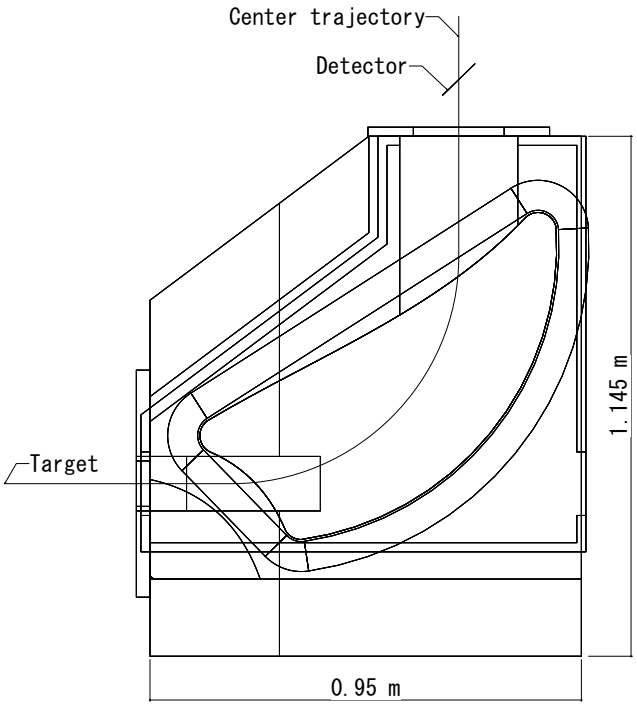

Fig.1. Lay-out of the spectrometer.

magnet is written as,

$$\begin{pmatrix} x' \\ y' \end{pmatrix} = \begin{pmatrix} \cos(\theta_b+\beta) & -\sin(\theta_b+\beta) \\ \sin(\theta_b+\beta) & \cos(\theta_b+\beta) \end{pmatrix} \begin{pmatrix} x \\ y \end{pmatrix} + \rho \begin{pmatrix} \cos\theta_b - 1 \\ \sin\theta_b \end{pmatrix} + l \begin{pmatrix} -\sin(\alpha+\beta) \\ \cos(\alpha+\beta) \end{pmatrix} \quad (1)$$

Here,

$$y = \frac{a_1}{\rho}x^2 + \frac{a_2}{\rho^2}x^3, \quad (2)$$

$$\alpha = \begin{cases} 0 & (\text{entrance}) \\ \theta_b & (\text{exit}). \end{cases} \quad (3)$$

The entrance and exit of the magnet have large angle with respect to the center trajectory to control $(y|\theta)$ by focusing and defocusing the electrons with fringing field. It improves the Ω and σ_θ about twice.

The second and third function shape of the pole piece controls a part of the transfer matrices such as $(x|\phi\phi)$, $(y|\theta\phi)$, $(x|\phi\phi\phi)$ and $(x|\phi\phi\delta)$ to archive smaller σ_p and σ_θ. Performance of the spectrometer was estimated with simulation, and summarized in table 3.

Table 3. Design parameter of the spectrometer

Maximum center momentum (MeV/c)	75
Maximum induction (T)	0.5
Momentum acceptance (%)	11
Horizontal angular acceptance (mrad)	$\pm$ 50
Vertical angular acceptance (mrad)	$\pm$ 50
Solid angle (mSr)	10
Scattering angle range ($^\circ$)	$30 - 150$
Angle of focal plane ($^\circ$)	44.2
Dispersion to magnification (mm/%)	8.34
Momentum resolution	8×10^{-4}
Angular resolution (mrad)	5

§3. Conclusion and future

In simulation, the spectrometer satisfies the experimental requests as summarized in table 3. The spectrometer has been constructed in the first experimental hall of ELPH in March 2019 . A commissioning of the spectrometer and beam line are planed in 2020.

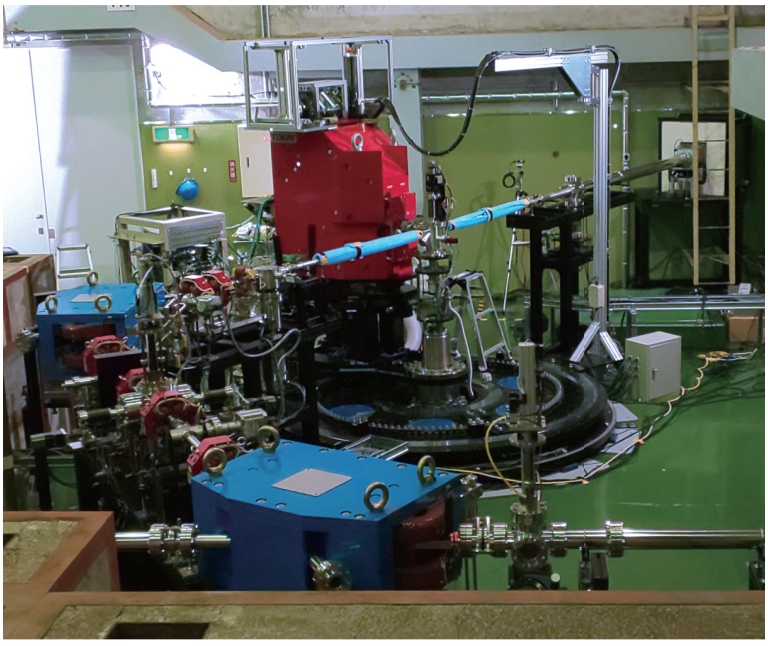

Fig.2. Picture of the spectrometer and ULQ2 beam line.

Acknowledgments

This work was supported in part by JSPS KAKENHI Grants Nos. 16H06340, and 18K13553.

References

[1] P. J. Mohr, B. N. Taylor, and D. B. Newell, Rev. Mod. Phys., vol. 84, no. 4, pp. 1527–1605, Nov. 2012.

[2] R. Pohl et al., Nature, vol. 466, no. 7303, pp. 213–216, 2010.

[3] A. Grinin et al., Science (80-.)., vol. 370, no. November 3, pp. 1061–1066, 2020.

[4] W. Xiong et al., Nature, vol. 575, no. June, pp. 147–151, 2019.

[5] H. Fleurbaey et al., Phys. Rev. Lett., vol. 183001, pp. 1–5, 2018.

[6] N. Kolachevsky et al., AIP Conf. Proc., vol. 1936, 2018.

[7] S. Morinobu, User manual of program "Orbit4", Private communication.

[8] OPERA 3D (TOSCA) https://www.3ds.com/products-services/simulia/products/opera/.

(ELPH Experiment : #2844, #2882, #2894, #2924, #2934)

Development of a silica aerogel Cherenkov detector for π/K separation fitted to the FOREST/BLC experiment

T. Yuzawa[1], Y. Emoto[1], K. Fujihara[1], T. Ishikawa[2], R. Kanai[1], H. Kawai[1], S. Kimata[1], S. Kimura[1], A. Kobayashi[1], M. Miyabe[2], K. Okuhata[1], and M. Tabata[1] for the FOREST/BLC collaboration

[1]*Department of Physics, Chiba University, Chiba 263-8522, Japan*
[2]*Research Center for Electron Photon Science (ELPH), Tohoku University, Sendai 982-0826, Japan*

We are developing a silica aerogel Cherenkov (AC) detector for π/K separation fitted to the FOREST/BLC experiment. We have used 8 silica aerogel blocks to construct an AC radiator with a size of $200 \times 200 \times 30$ mm^3. The refractive indices (n) of aerogel used are 1.12 and 1.09. The PMTs, Hamamatsu H3178-60, are connected to the AC radiator through an air gap. We have investigated the performance of the developed prototype and actual AC detectors three times using 600-MeV/c positrons at ELPH. Using a mirror-type reflector is found to be advantageous over a diffuser-type one for guiding a Cherenkov light to the PMTs. The distance of the air gap between the AC radiator and the PMT windows should be less than 30 mm to get enough light yield. The developed AC detector with $n = 1.12$ satisfies high separation power between π and K in the FOREST/BLC experiment for studying Λn interaction.

§1. Λn interaction

Charge symmetry (CS) is an important concept for describing many facets of nuclear physics: observables are hardly changed when all protons and neutrons are replaced with neutrons and protons, respectively. CS corresponds to invariance under the interchange of u and d quarks, and CS breaking (CSB) takes place owing to differences of u and d masses and electromagnetic effects. Recently, an unexpectedly large difference in the excitation energies is observed between the ${}^{4}_{\Lambda}$He and ${}^{4}_{\Lambda}$H mirror hypernuclei [1, 2]. CSB possibly occurs more strongly in hypernuclei than in ordinary nuclei. The full understanding of CSB still remains an open issue in nuclear physics. To reveal the cause of CSB, it is important to investigate the low-energy Λn and Λp scatterings.

How can we get the low-energy scattering parameters? The best way is to perform scattering experiments at low energies. Unfortunately, ΛN scattering experiments are difficult to be realized owing to the unstable nature of the Λ hyperon. In such a case, the final-state interaction (FSI) is often utilized alternatively. When more than two particles are generated in the final state, the relative momentum (or the invariant mass) distribution of the two particles are distorted near the threshold. The low-energy Λp scattering parameters have been determined by fitting the Λp invariant mass spectrum in the $pp \to K^+\Lambda p$ reaction and total cross section of the free Λp scattering simultaneously [3]. The scat-

tering length and effective range are $-2.43^{+0.16}_{-0.25}$ fm and $+2.21^{+0.16}_{-0.36}$ fm for the spin-singlet state, and those are $-1.56^{+0.19}_{-0.22}$ and $+3.7^{+0.6}_{-0.6}$ fm for the spin-triplet state. Currently, we do not have information on Λn scattering separately from Λp scattering although some constraints are provided from the detailed studies of the structures of hypernuclei.

A possible way to extract the Λn scattering parameters is K^+ photoproduction on the deuteron [4–7]. The quasi-free K^+ photoproduction on the bound proton $\gamma p \to K^+\Lambda$ is the corresponding elementary process, and the produced Λ is likely to interact with the spectator neutron at a specific kinematics. When we detect K^+s at extremely forward angles, distortion by the Λn FSI enhances the event yield at the highest K^+ momentum region (near the Λn threshold region in the Λn invariant mass distribution) [8–20].

The FOREST/BLC experiment [21] primarily aims at determination of the low-energy ηN scattering parameters by using the $\gamma d \to \eta pn$ reaction at a specific kinematics for investigating the internal structure of the nucleon resonance $N(1535)1/2^-$, which is speculated to be the chiral partner of the nucleon [22, 23]. The kinematics is similar to the $\gamma d \to K^+\Lambda n$ reaction for investigating the Λn interaction. In $\gamma d \to \eta pn$, the forward going protons are momentum-analyzed with particle identification using the BLC spectrometer, and η mesons are identified by two photons detected with the FOREST detector [24].

What we have to do is momentum analysis of the forward going K^+s with particle identification in $\gamma d \to K^+\Lambda n$ since K^+ must be associated with hyperon (Λ, Σ^0, or Σ^-) production. The Λn invariant mass can be calculated as the $d(\gamma, K^+)$ missing mass in $\gamma d \to K^+\Lambda n$. Basically, $\gamma d \to K^+\Lambda n$ can be separated from $\gamma d \to K^+\Sigma^0 n$ and $\gamma d \to K^+\Sigma^- p$ by detecting daughter particles $\pi^- p$ or $\pi^0 n$ from the Λ decay without any additional photon from the Σ^0 decay. Even if the daughter particles form the Λ decay are not detected, mis-identification of hyperons does not affect the low-mass region in the $d(\gamma, K^+)$ missing mass, where the Λn FSI enhances the event yield, in $\gamma d \to K^+\Sigma^0 n$ and $\gamma d \to K^+\Sigma^- p$. In this regard, to measure the singles K^+ momentum distribution at a fixed incident photon energy is of primary importance for investigating the Λn interaction.

Positrons, pions, kaons, and protons are detected with the BLC spectrometer. Most of the detected particles are positrons converted by pair production from the incident untagged and tagged photons. Additionally, much more positive pions are expected to be produced than kaons. It is important to increase the quality of K^+ identification for measuring the singles momentum distribution where we do not require daughter-particle detection from hyperons. Therefore, we have developed a silica aerogel Cherenkov counter for π/K separation fitted to the FOREST/BLC experiment.

§2. Silica Aerogel Cherenkov dectector

In the FOREST/BLC experiment, the forward spectrometer is placed behind the large-solid angle FOREST electromagnetic calorimeter. The forward spectrometer consists of a dipole magnet called BLC, 2 planar drift chambers (DCs) for the trajectory measurement, 14 plastic scintillators (PSs) for the time-of-flight measurement, and SF5 lead-glass Cherenkov counter for e/π separation. Fig. 1 shows the

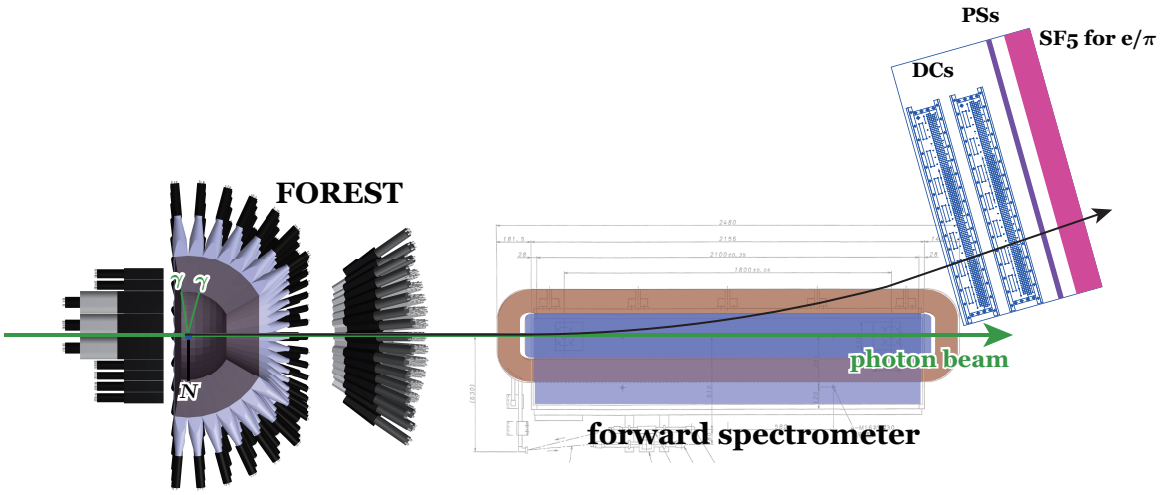

Fig.1. Experimental setup for the FOREST/BLC experiment. The momentum and time of flight of a charged particle emitted at 0° are measured through a bending magnet called BLC behind the FOREST detector. The trajectory is measured with two planar drift chambers (DCs), and the time of flight is measured with hodoscope comprised of 14 plastic scintillators (PSs). Additional e^+/π^+ separation is made using SF5 lead-glass Cherenkov counters.

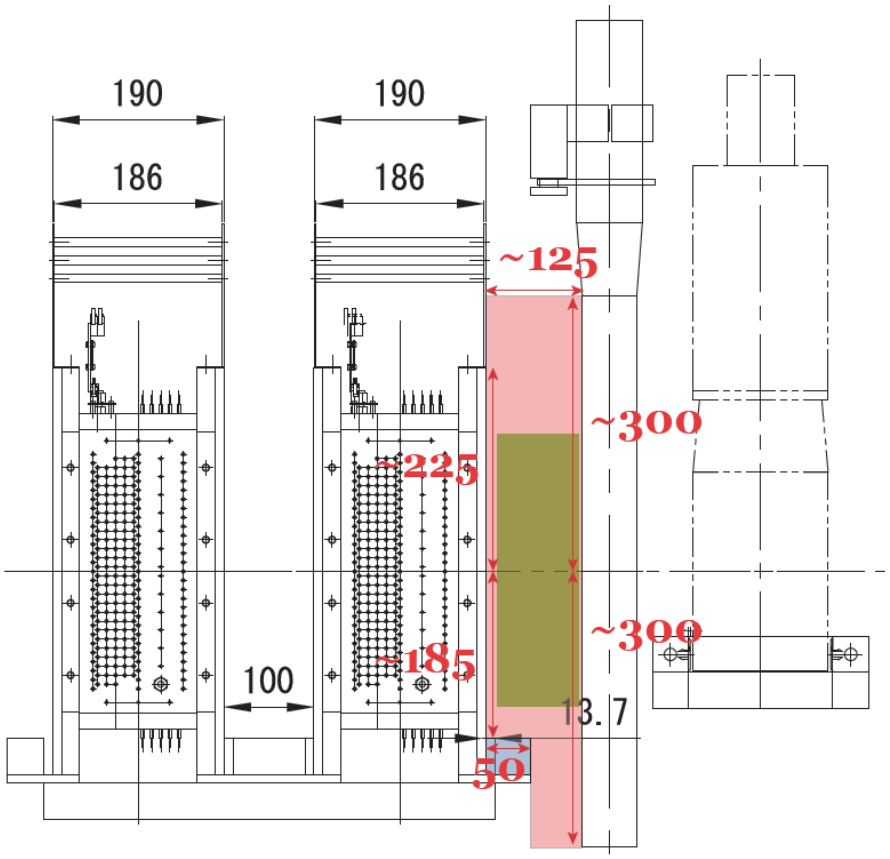

Fig.2. Cross sectional view of the detector placement for the BLC spectrometer. The distance is approximately 125 mm between the rear face of the downstream DC and front face of PSs.

experimental setup for the FOREST/BLC experiment. Not to disturb the trajectory measurement of a charged particle, we plan to place a detector system for π/K separation in the space between the rear face of the downstream DC and front face of PSs.

Since the maximum momentum of K^+ emitted at 0° in $\gamma d \to K^+ \Lambda n$ is approximately 1.0 GeV/c, we consider a detector made up of silica aerogel with a refractive index of 1.12, in which a Cherenkov light is not emitted by 1.0-GeV/c kaons but it is emitted by pions with the same momentum. In this regard, we have started to develop a silica aerogel Cherenkov (AC) detector for π/K separation. We have decided the effective area of the detector is a square with a side of 200 mm, and to use 1.5-inch photomultiplier tubes (PMTs), Hamamatsu H3168-60. To avoid the placement of thick material within the effective area of the BLC spectrometer for the momentum analysis of charges particles, the photocathode window of a PMT should be placed with a distance of 230 $\sim$ 250 mm from the horizontal plane including the central course of the photon beam. Fig. 2 shows the cross sectional view of the detector placement for the BLC spectrometer. The distance is approximately 125 mm between the rear face of the downstream DC and front face of PSs. It should be noted that the entrance and exit windows made of Mylar film in DC blister owing to the pressure difference inside and outside DC. We have required that the detector thickness is less than 90 mm. To get enough light yield, we have used two layers of 15-mm thick aerogel blocks, namely 30 mm thick in total.

§3. Beam tests

We have tested prototype and actual AC detectors three times using 600-MeV/c positron beams [25] at the Research Center for Electron Photon Science (ELPH), Tohoku University [26]. Here, we briefly describe the results from these beam tests.

3.1 Diffuser or mirror

The first beam test aimed at comparison of reflector types, diffuser or mirror, for guiding a Cherenkov light to the PMT windows. Fig. 3 shows the schematic view of the prototype AC detectors tested in the first beam test. We have adopted three layers of PTFE-film sheets as a diffuser-type reflector, and each sheet measures 80 μm in thickness. We have adopted a layer of aluminized PET-film sheet with a thickness of 12 μm as a mirror-type reflector. To collect Cherenkov photons effectively from 500-MeV/c π^+s, additional two planar mirrors are placed at the center with a tilting angle of 55° with respect to the central plane. The distance of an air gap was fixed at 50 mm between the edge of the radiator and PMT windows for both the prototype detectors. The silica aerogel radiator measured a square of 200 $\times$ 200 mm^2, and a thickness of 30 mm. Since a size of a single block of the silica aerogel was approximately 100 $\times$ 100 $\times$ 15 mm^3, we piled up eight blocks to construct the silica aerogel radiator. Fig. 4 shows the placement of silica aerogel blocks and photo of them.

The performances of the prototype AC detectors were investigated using a 600-MeV/c positron beam at ELPH. The impact position of a positron was determined with two plastic scintillators placed at $\sim$ 300-mm upstream and downstream of a prototype detector on the beamline. Each plastic scintillator

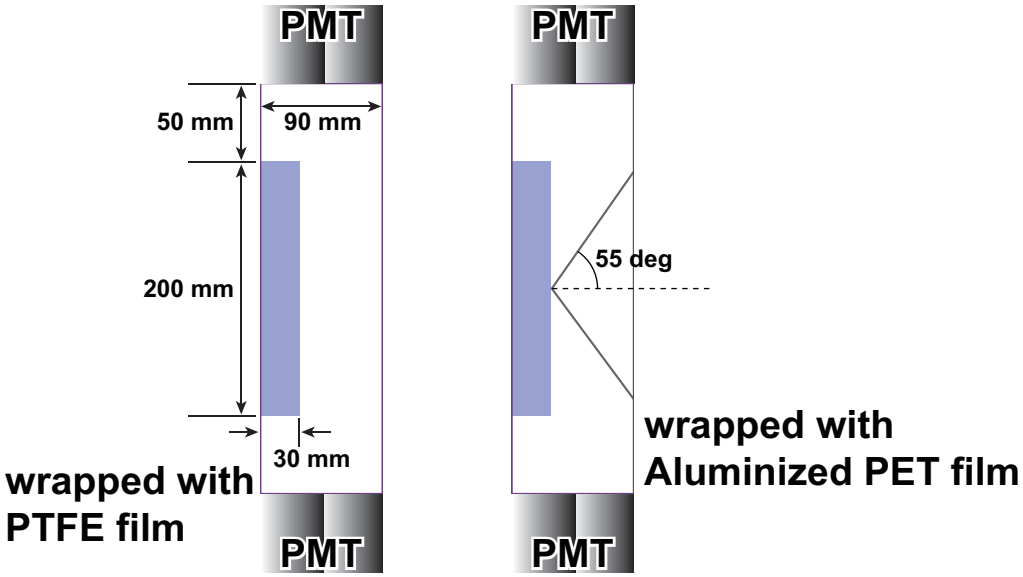

Fig.3. Schematic view of the prototype AC detectors tested in the first beam test.

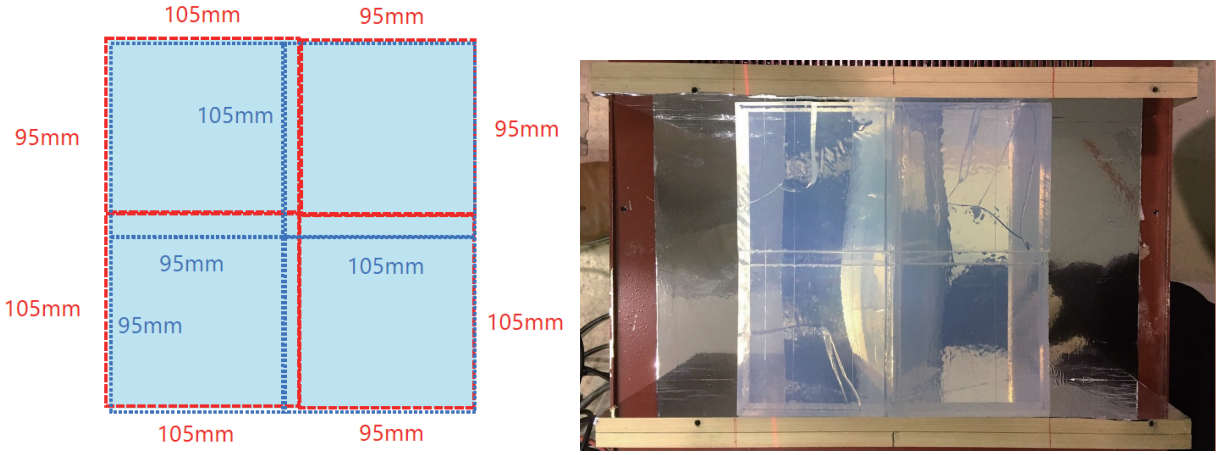

Fig.4. Placement of silica aerogel blocks to construct the Cherenkov radiator with a size of 200 × 200 × 30 mm^3 (left), and photo of them (right).

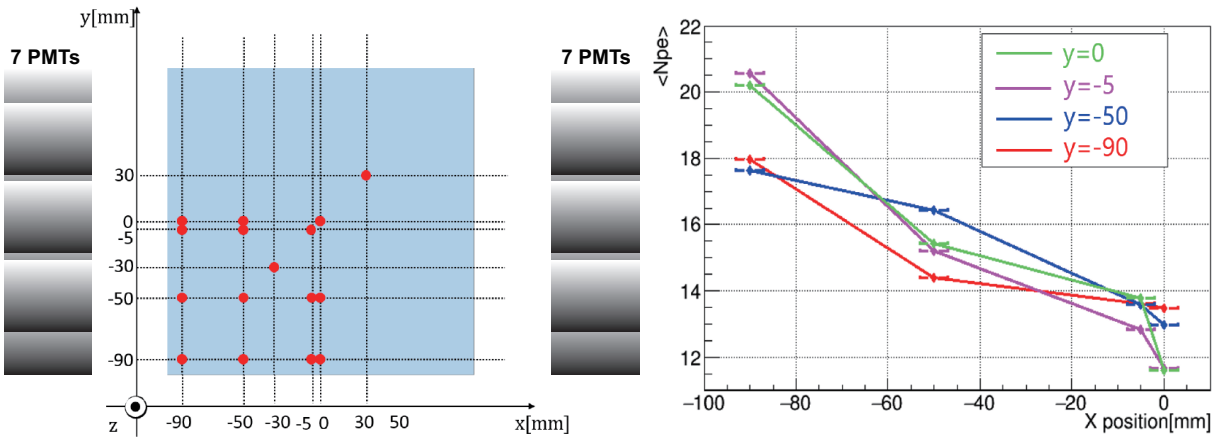

Fig.5. Impact positions of positron beams (left) and light yield as a function of the X position (corresponding to the distance from the PMT windows) for the mirror-type prototype detector (right).

measures a size of $5 \times 5 \times 5$ mm^3. During the beam test, the prototype detectors are rotated by 90° with respect to the beam axis. The X, Y, and Z axes are defined to give the position corresponding to the distance from the PMT windows, that orthogonal to it in the effective area of the silica aerogel radiator, and depth, respectively. Fig. 5 shows the impact positions of positrons and light yield as a function of the X position for the mirror-type prototype detector. The light yields highly depend on the X position, and similar light yields are obtained for different Y positions for the same X.

A finite light yields were obtained even if the radiator was not placed. The light yields were 11.7 and 0.7 photoelectrons (pe) with and without the radiator, respectively, at the center for the mirror-type detector. Those were 13.0 and 2.8 pe at the ceter for the diffuser-type. The intrinsic light yield from the radiator was slightly larger for the mirror-type. Table 1 summarizes the mis-identification probability and efficiency for several threshold values for the mirror- and diffuser-type prototype detectors. Here, the mis-identification probability is defined as a probability for responding even if the radiator is not placed, giving the probability that a kaon is erroneously recognized as a pion. To get high efficiency and low mis-identification probability simultaneously, the mirror-type detector was found to be much advantageous.

Table 1. Mis-identification probability and efficiency for several threshold values. The mis-identification shows a probability for responding even if the radiator is not placed, and #pe stands for the number of photoelectrons.

threshold (#pe)	mirror type		diffuser type	
	mis-identification	efficiency	mis-identification	efficiency
1.5	7.5%	98.8%	48.3%	99.9%
2.0	4.3%	98.2%	37.4%	99.8%
5.0	0.4%	87.9%	5.9%	96.6%
5.5	0.3%	85.3%	4.4%	95.4%

3.2 2nd beam test

The second beam test aimed at increasing the light yield in the mirror-type detector. We have reduced the air-gap distance from 50 to 30 mm. Owing to the space for the PMT placement as shown in Fig. 2, only 4 PMTs can be placed in the lower side. Thus, the position and tilting angle of the central tilted mirror were modified, or an additional mirror was introduced. Fig. 6 shows the schematic view of the prototype AC detectors tested in the second beam test. Although the available space for the PMT placement in the bottom is downstream side, the beam test was performed with placing PMTs in the opposite upstream side as shown in Fig. 6. Thus, the results did not make sense from the modifications of the position and tilting angle of the central tilted mirror and introduction of an additional mirror. However, the light yield obtained from the PMTs in a side was found to be a (linear) function of the distance from the PMT windows by combining the results from the first and second beam tests. It is important to minimize the air-gap distance for maximizing the light yield. The threshold value of 5 pe was expected to give an efficiency higher than 99% for the air-gap distance $20 \sim 30$ mm even if we did

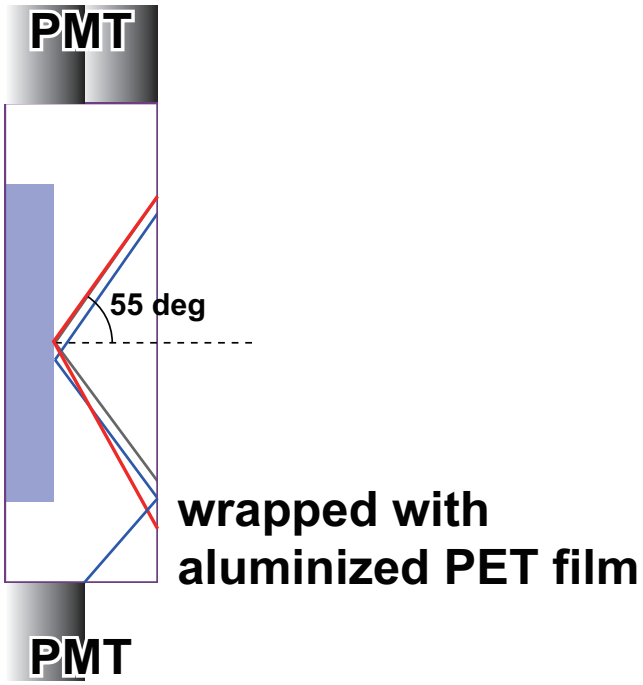

Fig.6. Schematic view of the prototype AC detector tested in the second beam test. The position and tilting angle of the central tilted mirror are modified (red), or an additional mirror is introduced (blue).

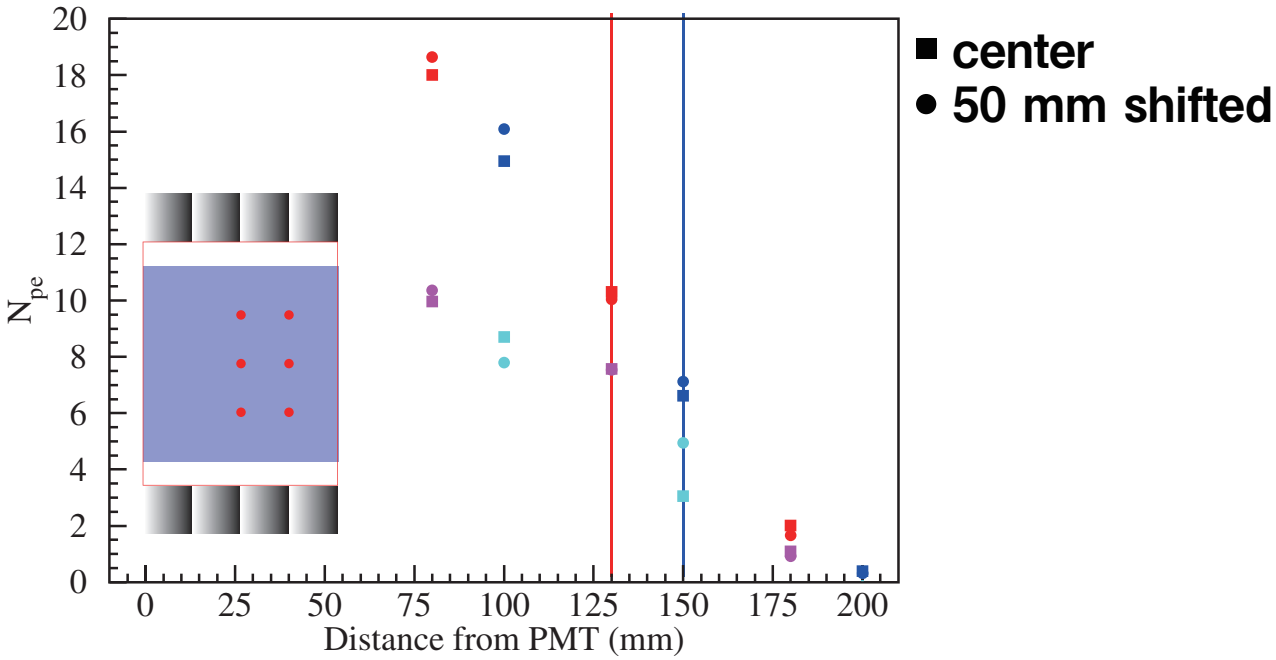

Fig.7. Light yield as a function of the PMT windows. The light yields are almost the same for different Y positions. The blue and cyan markers are obtained in the first beam test, and the red and magenta in the second. Each of the vertical lines corresponds to the data positron beam is injected at the center between the top and bottom PMT windows. The blue and red markers represent the light yields obtained from 7 PMTs, and cyan and magenta represent those from 4 PMTs.

not modify the position and tilting angle of the central tilted mirror or introduce an additional mirror.

3.3 3rd beam test

Since an efficiency is expected to be higher than 99% with an air-gap distance of 20 $\sim$ 30 mm and threshold value of 5 pe, we have constructed the AC detector to be used in the FOREST/BLC experiment. We investigate the performance of this actual detector in the third beam test. Fig. 8(left) shows a photo of the AC detector. To reduce the material through which charged particles pass, each of the tilted mirrors plays a role as a wall. The 7 PMTs are connected in the upper side, and 4 PMTs are connected in the lower downstream side. The air-gap distance was fixed at 30 mm. The silica aerogel radiator was mounted on a dummy block, and supported by threads. The dummy block was a silica aerogel with a size of 40 $\times$ 25 mm^3 and a refractive index of 1.03. Fig. 8(upper right) shows a photo of the dummy block and supporting threads for the radiator placement. All the silica aerogel blocks to be used in the radiator were replaced with new ones without any cracks. Since the transparency is much higher for a low refractive index aerogel than a higher one, we used four silica aerogel blocks with a refractive index

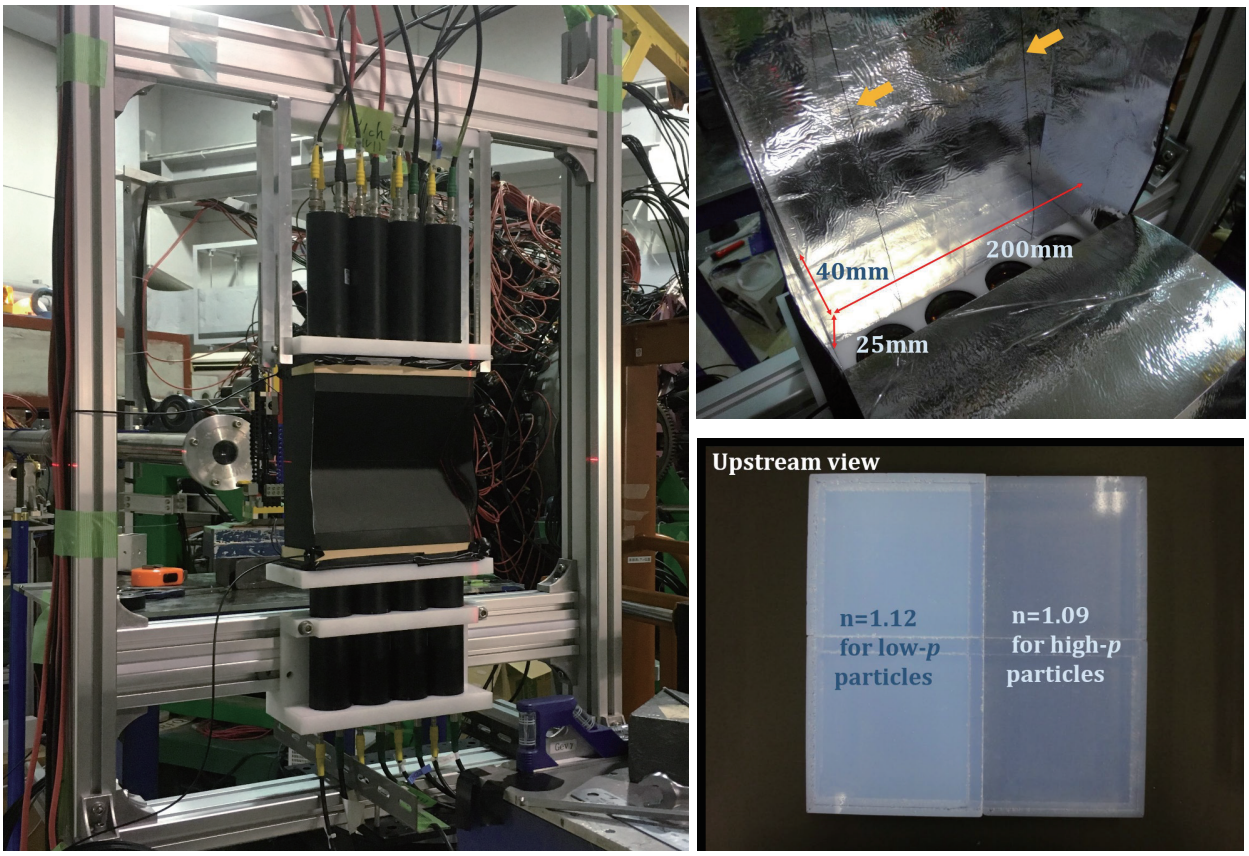

Fig.8. Photo of the AC detector to be used in the FOREST/BLC experiment (left), the supporting block and threads for the radiator placement (upper right), and silica aerogel blocks used for the radiator (lower right). The photo is taken from the downstream side. The supporting block is a dummy silica aerogel with a size of 40 $\times$ 25 mm^3 and a refractive index of 1.03. The silica aerogel blocks with refractive indices of 1.12 and 1.09 are used in the low- and high-momentum sides, respectively.

of 1.09 for the higher momentum side. Fig. 8(lower right) shows a photo of the silica aerogel blocks used in the radiator.

The experimental setup was similar to that for the first (second) beam test. Fig. 9 shows the impact positions of positrons for the light-yield measurement with and without the silica aerogel radiator. The X and Y axes in the frame of the AC detector were rotated by 90° with respect to the z axis in the third beam test as compared with the first and second tests. The 7 (4) PMTs are placed so that those windows are at $Y = +130$ (-130) mm.

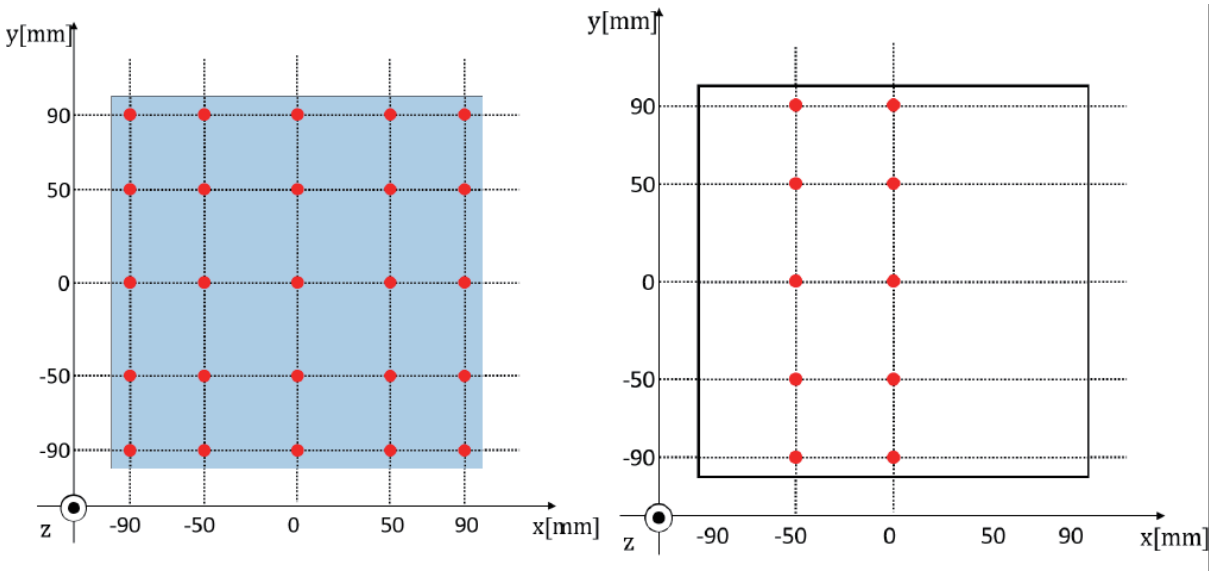

Fig.9. Impact positions of positrons for the light yield measurement with (left) and without (right) the silica aerogel radiator. The 7 (4) PMTs are placed so that those windows are at $Y = +130$ (-130) mm.

The total light yield was obtained by summing up all the energies in the 11 PMTs. Fig. 10 shows the light yield as a function of the Y position (corresponding to the distance from the PMT windows). It does not take a convex downward shape but shows a monotonically increasing behavior. This is because the number of the PMTs placed at $Y = -130$ mm was 4, and because Cherenkov photons were not sufficiently collected in these PMTs.

At first, the efficiency was estimated from the total light yield with a fixed threshold value. In this case, an efficiency of 98.1% and a mis-identification probability of 4.1% were obtained with a threshold value of 5.5 pe. Fig. 11(left) shows the efficiency and a mis-identification probability as a function of the threshold for the total light yield. Since the reasonable threshold value of 5.5 pe is too high for the typical light yield. We estimated the efficiency in an alternative way: the detector is considered to respond to a positron when the number of PMTs having higher light yield than 0.5 pe is larger than the threshold number of PMTs. In this case, an efficiency of 98.4% and a mis-identification probability of 2.4% were obtained with a threshold value of 4. Fig. 11(right) shows the efficiency and a mis-identification probability as a function of the threshold number of responding PMTs.

Thus far, efficiencies were estimated for the 600-MeV/c positrons with almost the speed of light. The

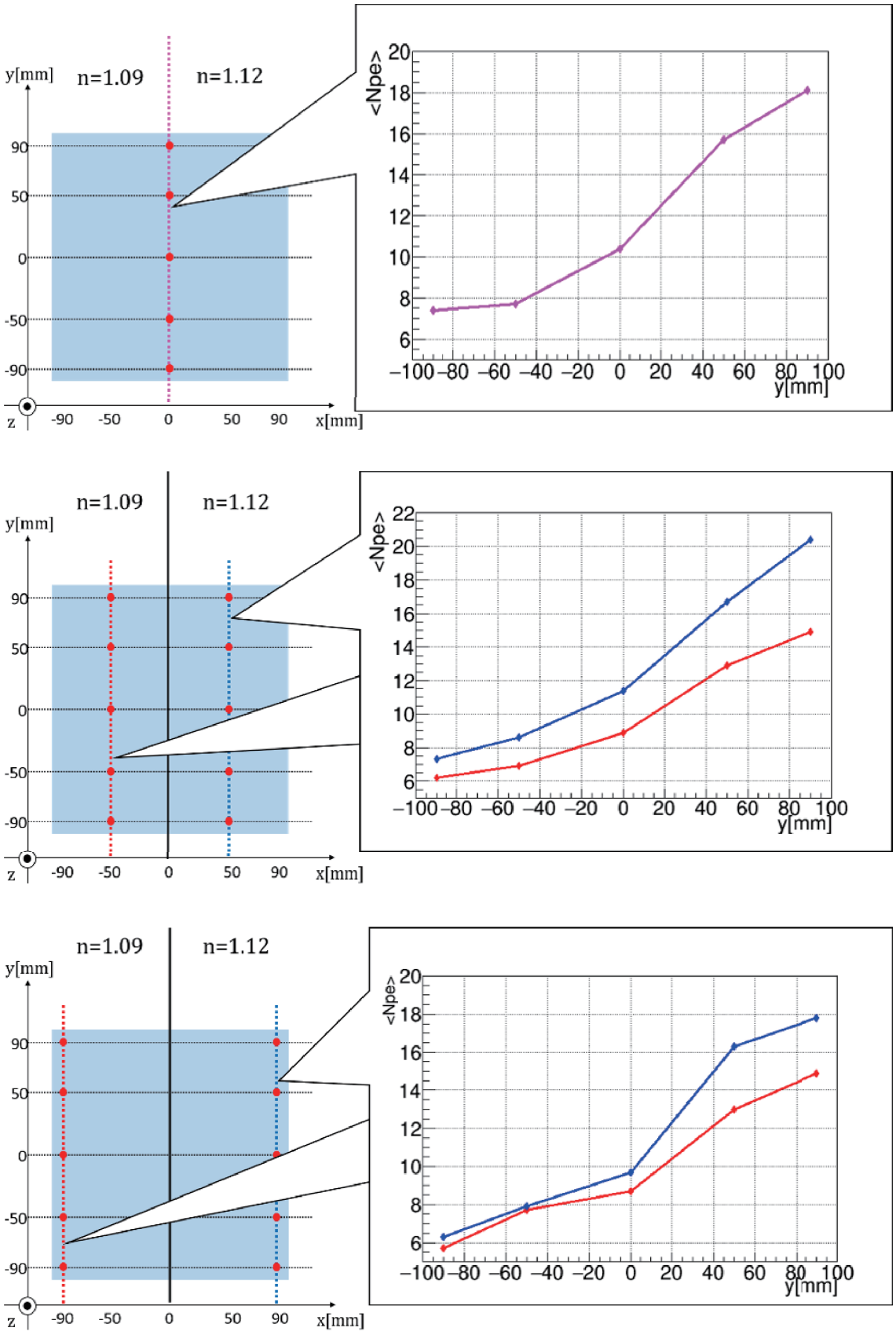

Fig.10. Light yield as a function of the Y position (corresponding to the distance from the PMT windows). Seven PMTs are placed at $Y = +130$ mm, and four at $Y = -130$ mm.

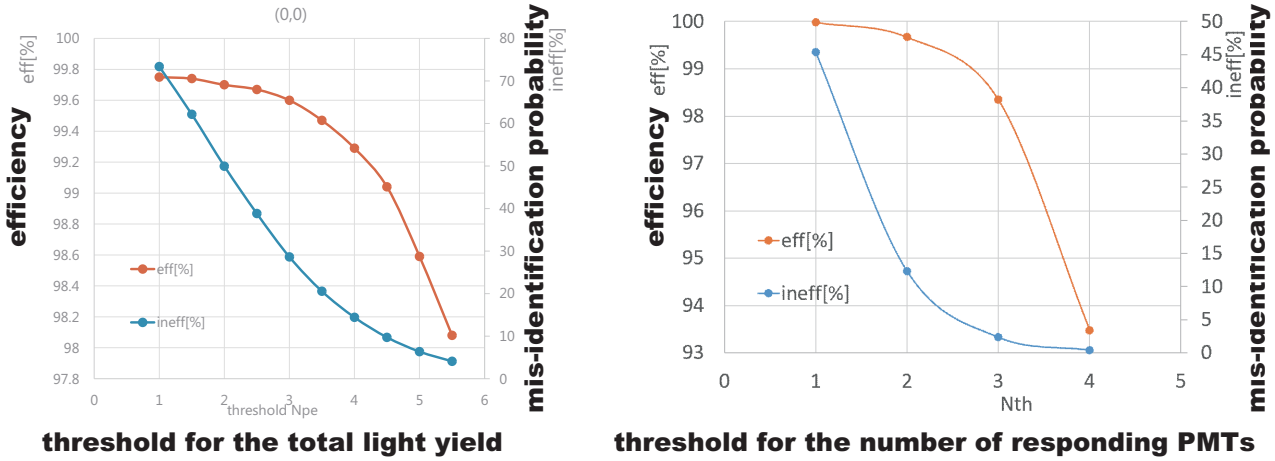

Fig.11. Efficiency and a mis-identification probability as a function of the threshold for the total light yield (left), and those as a function of the threshold number of responding PMTs (left), The red points represent the efficiency for 600-MeV/c positrons with the left vertical axis, and the blue shows the mis-identification probability with the right axis.

light yield for 675-MeV/c pions are 4/5 of that for the 600-MeV/c positrons . Fig. 12 shows the efficiencies as a function of the Y position for different X positions with a threshold value of 2 pe. Except in the edge region, efficiencies were obtained higher than 97% for 675-MeV/c pions.

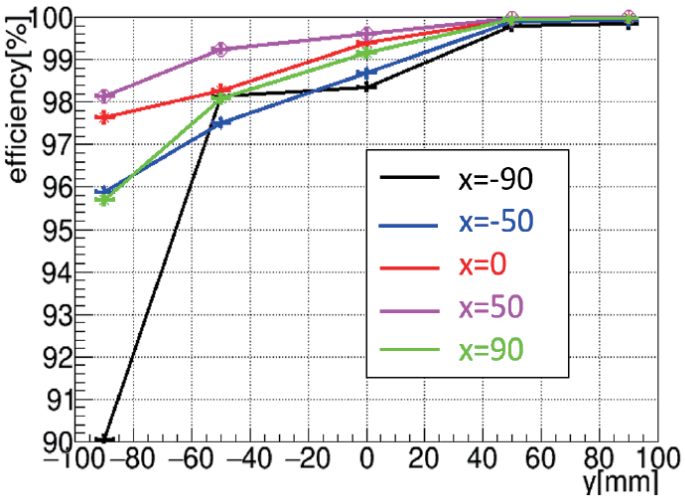

Fig.12. Efficiency as a function of the Y position for different X positions with a threshold value of 2 pe.

§4. Summary

We are developing an AC detector for π/K separation fitted to the FOREST/BLC experiment. We have found that the mirror-type is advantageous over the diffuser-type for guiding a Cherenkov light to the PMTs. We have constructed the AC detector, and investigated its performance using 600-MeV/c positrons at ELPH. Silica aerogel blocks with refractive indices of 1.12 and 1.09 have been used in the

lower- and higher-momentum side of the radiator. The light yield of 10.4 pe have been obtained at the center. And we have obtained efficiencies higher than 97% except in the edge region. The low light yield was considered to come from using a low index (1.09) aerogel blocks. We will have enough efficiencies by replacing them with 1.12 ones.

Acknowledgment

The authors express gratitude to the ELPH accelerator staff for stable operation of the accelerators for testing the AC detector. They acknowledge Mr. Ken'ichi Nanbu, and Mr. Ikuro Nagasawa for their technical assistance. This work was supported in part by the Japan Society for the Promotion of Science (JSPS) through Grants-in-Aid for Scientific Research (B) No. 19H01902, and for Scientific Research on Innovative Areas Nos. 19H05141 and 19H05181.

References

[1] T.O. Yamamoto et al. (J-PARC E13 collaboration): Phys. Rev. Lett. **115** (2015) 222501.
[2] A. Esser et al. (A1 collaboration at MAMI): Phys. Rev. Lett. **114** (2015) 232501.
[3] A. Budzanowski *et al.* (HIRES collaboration): Phys. Lett. B **687** (2010) 31.
[4] A. Gasparyan, J. Haidenbauer, C. Hanhart, J. Speth: Phys. Rev. C **69** (2004) 034006.
[5] A. Gasparyan, J. Haidenbauer, C. Hanhart: Phys. Rev. C **72** (2005) 034006.
[6] J.T. Balewski *et al.*, Eur. Phys. J. A **2** (1998) 99.
[7] F. Hinterberger, A. Sibirtsev, Eur. Phys. J. A **21** (2004) 313.
[8] F.M. Renard, Y. Renard, Nucl. Phys. B **1** (1967) 389.
[9] B.O. Kerbikov, B.L.G. Bakker, R. Daling: Nucl. Phys. A **480** (1988) 585.
[10] B.O. Kerbikov: Phys. At. Nucl. **64** (2001) 1835.
[11] R.A. Adelseck, L.E. Wright: Phys. Rev. C **39** (1989) 580.
[12] X. Li, L.E. Wright: J. Phys. G **17** (1991) 1127.
[13] H. Yamamura *et al.*, Phys. Rev. C **61** (1999) 014001.
[14] O.V. Maxwell: Phys. Rev. C **69** (2004) 034605.
[15] O.V. Maxwell: Phys. Rev. C **70** (2004) 044612.
[16] A. Salam, H. Arenhövel: Phys. Rev. C **70** (2004) 044008.
[17] K. Miyagawa, T. Mart, C. Bennhold, W. Glöckle: Phys. Rev. C **74** (2006) 034002.
[18] A. Salam, K. Miyagawa, T. Mart, C. Bennhold, W. Glöckle: Phys. Rev. C **74** (2006) 044004.
[19] J.M. Laget: Phys. Rev. C **75** (2007) 014002.
[20] A. Gasparyan *et al.*: Eur. Phys. J. A **32** (2007) 61.
[21] T. Ishikawa *et al.*: JPS Conf. Proc. **13** (2016) 020031.
[22] T. Ishikawa *et al.*, Acta Phys. Polon. B **48** (2017) 1801.
[23] S.X. Nakamura, H. Kamano, T. Ishikawa, Phys. Rev. C **96** (2017) 042201 (R).
[24] T. Ishikawa *et al.*: Nucl. Instrum. and Meth. A **832** (2016) 108.

[25] T. Ishikawa *et al.*: Nucl. Instrum. and Meth. A **694** (2012) 348.

[26] H. Hama, AAPPS Bulletin **30** (2020) 41.

(ELPH Experiment : #2897, #2908)

Development of a simple imaging system for radioisotopes Using a cooled CCD camera

Hidetoshi KIKUNAGA[1]

[1]*Research Center for Electron Photon Science, Tohoku University, Sendai, 982-0826*

In this study, we develop a simple imaging system for radioisotopes (RI) using a cooled CCD camera to promote research using RI at Research Center for Electron Photon Science, Tohoku University (ELPH). The system consists of a cooled CCD camera and a plastic scintillator installed in a dark box to detect radiation from a source located outside the dark box. As a test experiment, a nickel foil was irradiated with bremsstrahlung and their radioactivity distributions were measured using the device developed in this study. As a result, we were able to obtain an image that was consistent with the distribution of the radioactivity.

§1. Introduction

Various radioisotopes produced by the high-intensity electron linear accelerator are used for research at ELPH. For example, potassium isotopes are used as tracers to study the dynamics of potassium in plants. Copper isotopes are used in basic research for the development of drugs for nuclear medicine. In addition, photo-quantum activation analysis, in which various materials are irradiated with bremsstrahlung to measure their elemental content, has been conducted.

We plan to develop an imaging system for radioisotopes to promote research using RI at ELPH. The imaging system allows, for example, in vivo tracking of elemental behavior in real time and beam diagnostics using activation analysis. In this paper, we report on the preparation of a simple imaging system for radioisotopes (RIs) using a cooled CCD camera and the measurement of the radioactivity distribution of the activated metal foil using the system.

§2. Experimental

The schematic diagram of the developed system (CCD-PS system) is shown in Fig. 1. The plastic scintillator was a TYPE CIP-3 from C. I. Industry Co., Ltd. with a size of 300 mm square and a thickness of 1 mm. The cooled CCD camera (BU-61M, BITRAN co.) was fixed approximately 300 mm from the scintillator. The scintillator and camera were enclosed in a dark box, and the outside of the box was covered with a light-shielding curtain.

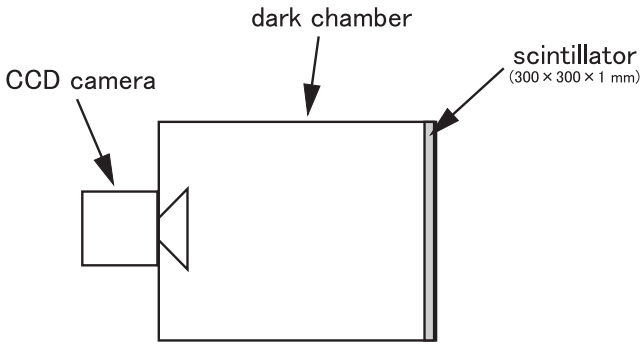

Fig.1. Schematic diagram of the developed system (CCD-PS system)

The activation of the metal foil was performed using the high intensity electron linear accelerator at ELPH. A picture of the irradiation setup is shown in Fig. 2. A nickel foil with 50 mm square and 50 μm thickness was placed about 20 mm downstream of the 3 mm tantalum converter at the end of the RI production beam line. The accelerator was operated at an electron energy of 55 MeV with a mean current around 0.1 mA. The irradiation was carried out for 10 minutes. Separately, a 100 μm thick Ti foil with 5 mm $\times$ 30 mm size was irradiated for 3 minutes in order to use it as a sample for position checking.

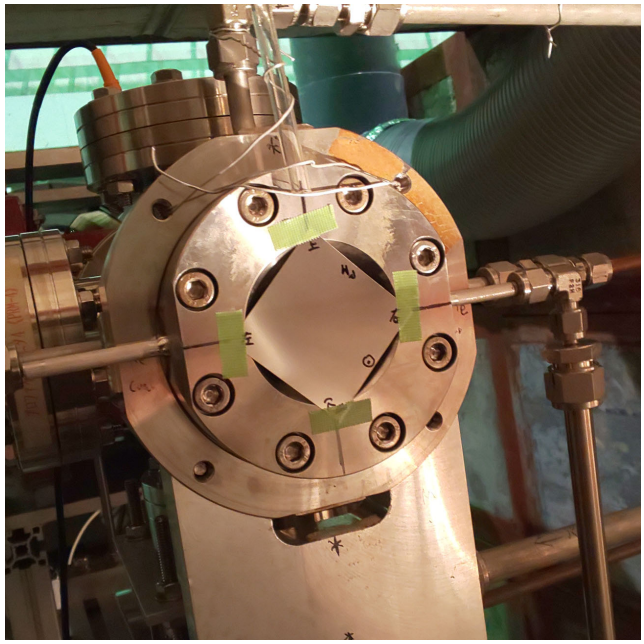

Fig.2. Irradiation setup for a Ni target

An example of a sample measurement is shown in Fig. 3. The irradiated nickel foil was fixed to the scintillator side of the CCD-PS system. The edge of the Ni foil was not activated, so it could not be imaged by the CCD-PS system. Therefore, activated Ti foil was placed on the four edges of the Ni foil to determine its position. The measurements were performed for 3 minutes at 1.5 hours after the end of irradiation.

Fig.3. Example of a sample measurement with CCD-PS system.

§3. Results

The image obtained by the CCD-PS system is shown in Fig. 4. The major radioactivity in the Ni sample was found to be ^{5}7Ni (about 4.8 MBq) produced in the ^{5}8Ni(γ,n) reaction by γ spectrometry with a high-purity Ge semiconductor detector. Therefore, this distribution is considered to indicate the spread of bremsstrahlung. It is possible to investigate the distribution of the irradiated bremsstrahlung by correcting the distribution by point spread. We are currently investigating the detection limits and other performance properties.

Fig.4. Example of an image obtained by the CCD-PS system.

II. Status Report

Status of Accelerator Facilities in FY2019

T. Muto, K. Kanomata, S. Kashiwagi, F. Hinode, S. Miura, I.Nagasawa,
K. Nanbu, K. Shibata, K. Takahashi and H. Hama

Accelerator group in ELPH, Tohoku University, Sendai, 982-0826

In FY2019, the total operating time of electron accelerator complex in ELPH; high intensity 60MeV linac, 90MeV injector linac and 1.3GeV BST (Booster-Storage Ring) and test accelerator t-ACTS, exceeded 2000 hours. Two large update work was done at the high intensity linac. One was the changing of the control system's software in spring. For higher maintainability, the software of control system changed to EPICS and LabVIEW, which were same software of injector and BST ring control system. Another one was the replacement of electron gun in summer. The new gun cathode EIMAC Y646-B was widely used and would be provided for long term. The high intensity linac with the new gun could become to provide same quality electron beam.

§1. High intensity linac

The high intensity linac can provide the electron beam with repetition rate up to 300Hz and energy range of 10-60MeV. The typical beam current is 120μA for 50MeV operation. The operating beam time of the high intensity linac in FY 2019 exceeded 350 hours.

Upgrade work of control system was carried out on the spring. Pervious control system was made by Simple Transmission and Retrieval System (STARS)[1] and Visual Basic[2]. New control system was made by Experimental Physics and Industrial Control System (EPICS)[3] and LabVIEW[4], which are same software used on the control system of the injector linac and the BST ring. By using same software of two control systems, maintainability would be increased, but human resource for maintenance would be reduced. However, two control systems are still independent for the rigidity of each accelerator systems and different operation schedule. The window of new control system is shown in Fig.1.

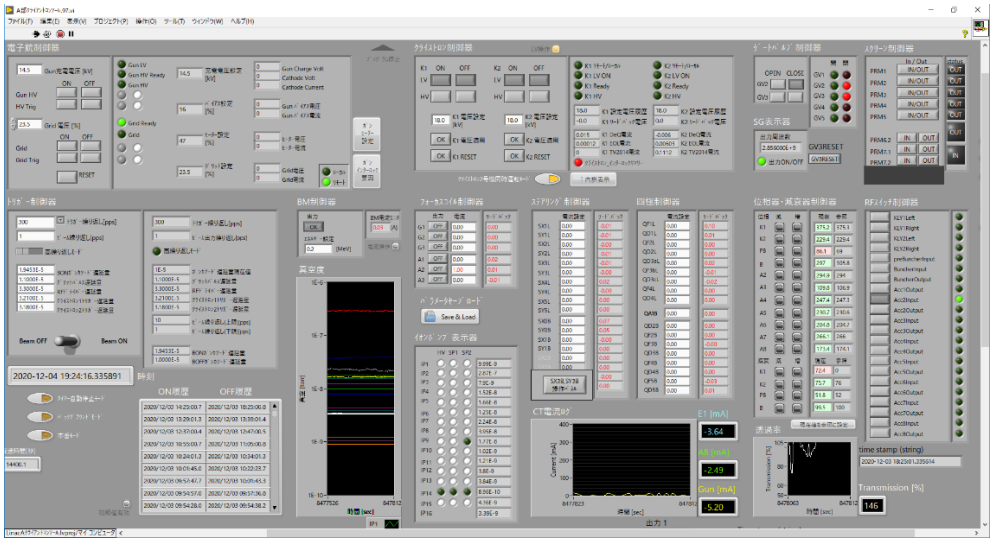

Figure 1 New control window of high intensity linac

In summer shutdown, the update work of the electron gun was done. It had been difficult to maintenance because of gun cathode was stopped to supply by the manufacturer. New electron gun was designed to fit the cathode EIMAC Y646-B, which was widely used for the accelerator of sterilization, and which would be provided by the manufacture for long term. There were some small troubles in staring up, but the replacement work was done. The high intensity linac with the new gun could become to provide same quality electron beam with beam current 120μA (50MeV operation).

A large vacuum leak was happened on beam tuning in October. This leak at flanges near bending magnet in 1st experimental hall would be caused by heating that the electron beam hit to beam duct. To monitor this heating, four thermocouples was put on beam duct around leak position. The heating of beam ducts could be avoided by checking these temperatures and careful beam tuning. There was no vacuum leak around bending magnet after this modification.

In December operation, two incidents were occurred. One incident was irradiation to converter without cooling water. This problem caused by lack of cooling water in reservoir tank. Another one was more serious. That was vacuum leak at Ti window of beam irradiation system. By the elements analysis of the Ti window, Oxygen molecule was detected at leaking position of Ti window (Fig.2). However, Oxygen molecule was not detected at another part of Ti window (Fig.3). It suggested presence of water in He circulating by cooling system and some reaction between water and Ti by beam irradiation was occurred.

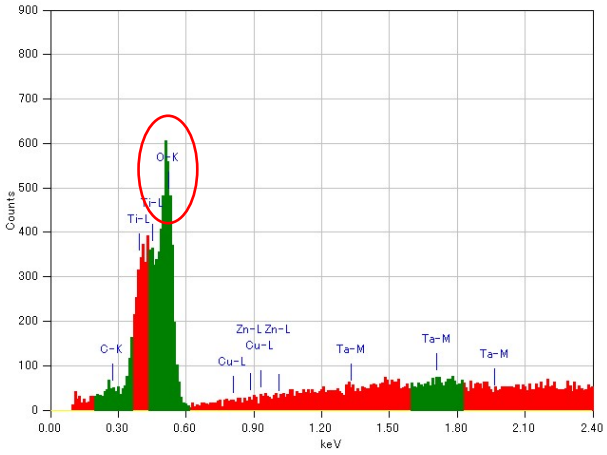

Figure 2 Elemental distribution of leak position of Ti window. Red circle was Oxygen peak.

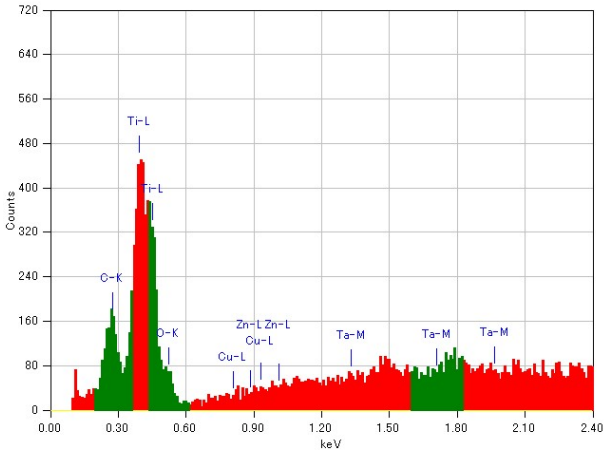

Figure 3 Elemental distribution of another part of Ti window. There was no Oxygen peak.

Both incidents were caused by failure of cooling system which is part of irradiation system. So, the irradiation system was modified. In the water cooling system for the converter, the water level gauge was added to reservoir tank to check water level. The He cooling system was simplified and added the dew-point meter to check water in He. After this modification, cooling system was tested. However, the dew-point of He was still not enough low. There would be the slow leak of converter's cooling water to He cooling system. To remove the moisture, Molecular Sieve, which is a kind of Zeolite, was installed to He cooling system. By Molecular Sieve, the dew-point of He system was reduced to enough low. From February, beam time for users was served.

§2. Injector linac

The injector linac stably supplies an electron beam to the BST ring with 90MeV. However, there is a problem that discharge of thermionic rf gun was occurred and the gun became unstable in May operation. This problem already has been occurred few times[5]. It was recovered by replacement of gun cathode.

By the permission of the change request to Nuclear Regulation Authority, new electron beamline could be operated. This beamline so-called "beamline II" provided 90MeV electron beam direct to experiment area in Accelerator room (Fig.4). In October operation, beamline II provided electron beam to users.

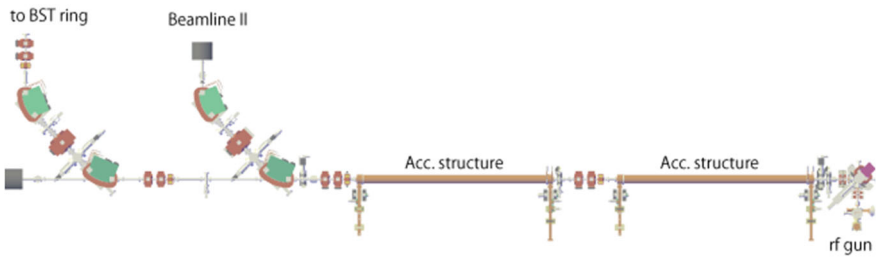

Figure 4 Layout of the Injector linac

The operating time of the injector linac exceeded 1300 hours in FY2019.

§3. BST ring

The 1.3GeV BST ring has well operated to generate high energy gamma rays via bremsstrahlung from internal target wire inserted to electron orbit. Generated gamma rays are not only utilized to the experiment for quark/hadron physics, but also supplied to the test beam line for testing of detectors used in high energy experiments. The operating time of the BST ring exceeded to 1250 hours in FY2019.

On long beam time for hadron physics experiment in April and May, the power supply of DC septum was broken and replaced at three time. In June, the thyratron of kicker in BST ring was replaced.

§4. Test accelerator t-ACTS

The test accelerator as Coherent THz Source (t-ACTS) provided extremely short electron beam with bunch length ~80fs for generation of various radiation as coherent transition radiation (CTR), coherent undulator radiation and coherent Cherenkov radiation[6]. The operating time of t-ACTS in FY2019 exceeded 350 hours.

References

[1] http://stars.kek.jp/

[2] https://docs.microsoft.com/ja-jp/dotnet/visual-basic/

[3] https://epics-controls.org/

[4] https://www.ni.com/ja-jp/shop/labview.html

[5] F. Hinode *et al.*, “Status of Accelerator Facilities in FY2018”, ELPH Annual Report, Tohoku University (2018)

[6] S. Kahiwagi *et al.*, “STATUS OF TEST-ACCELERATOR AS COHERENT THz SOURCE (t-ACTS) AT ELPH, TOHOKU UNIVERSITY“, proceedings of 10th Int. Particle Accelerator Conf. (IPAC2019), Melbourne, (2019), 1475-1477

User Support Office Report in FY2019

M. Miyabe[1] and The user support office[1]

[1]*Research Center for Electron Photon Science, Tohoku University, Sendai, 982-0826, Japan*

The User Support Office coordinate across the users and our facility for management of the beam-time. In 2019 financial year, we had provided the electron, photon and positron beam. But Vacuum leak problems were occurred several times, we could not provide the beam as planned initially. In May, October and December 2019, because the failure of the Vacuum leak has occurred, we couldn't provide any user beam-time because of the repairing work during these period. In addition, in early December, the electric gun problem has occurred at 70 MeV electric linear accelerator [1, 2].

§1. Introduction

ELPH has three accelerators for Joint Usage/Research. Our facility could provide several beams with following three beam lines,

- 70 MeV electron linear accelerator (linac) at the first irradiation lab (For Radiochemistry, **BEAM LINE I**)
- Tagged photon beam from 1.3 GeV electron synchrotron called BST ring with 90 MeV injector at the second irradiation lab (For Hadron Physics, **BEAM LINE II, Photon beamline I**)
- Tagged photon beam at the GeV-γ irradiation room (For Hadron Physics, **BEAM LINE III, Photon beamline II**)

In addition, positron/electron beam line for testing detectors is located at the GeV-γ irradiation room. The 70 MeV electron linear accelerator was utilized for the Radiochemistry experiments by photo-nuclear reactions. It could produce radio active source with its high intensity. Both tagged photon beam line was used for Hadron physics experiments. NKS2 and FOREST/BLC experiment have bean held in recent years.

§2. Beamtime operated

The total radiation time was 311 hours for the RI linac operation and 1269 hours for the BST operation, and it was 1580 hours in total. Table 1 summarizes the radiation times, and user beam times in fiscal.

Many experiments for testing detectors were made by positron beam line. Positron beam was produced by bremsstrahlung photon beams from the synchrotron. Total 39 shifts experiments are performed using this positron beam in this financial year.

A Next generation FOREST experiments (FOREST/BLC) was started by GeV-γ group in ELPH. New bending magnet was installed on the downstream of FOREST detectors and it covers the most forward angle. These new experimental setup enable the zero degree proton detection for the $\gamma d \to p\eta n$ reaction at $E_\gamma \sim 0.9$ GeV. This reaction gives the zero relative momentum between the η and n. This situation will enable to determine the ηn scattering length. In this financial year, physical data was taken with hydrogen and deuteron target. Total 58 shifts of FOREST/BLC experiment(#2894) were carried out.

In Photon beam line I, New detectors research and developments for NKS2 experiment(#2787) has been carried out in this financial year.

one experiment was carried out for the undergraduate students. This experiment (#2926: H. Ohnishi, ELPH, Tohoku University) is for the education of the undergraduate students in ELPH [**?**].

Table 1. Radiation times, and user beamtimes in financial year 2019. They are given by the sum of the times that the beam is coming to the beamline, and that the beam is provided to the users.

Month	RI Linuac radiation (h)	BST Ring radiation (h)
April	0	547
May	19	165
Jun	61	112
July	88	0
August	0	0
September	0	0
October	29	17
November	1	153
December	48	173
January	0	48
February	64	54
March	0	0
Sum	311	1269

§3. ELPH workshops and ELPH seminars

In this fiscal year, ELPH supported two ELPH workshops. the first one is "SNP school 2019 [4]" (C025: S. N. Nakamura, Tohoku University), The second one is hadron physics "ハドロン構造における多粒子相関" (C024: D. Jido, Tokyo Institute of Technology). Additionally, 13 ELPH seminars were held in this fiscal year. Seminars title and talker are listed below.

- 前田 幸重, 宮崎大学工学教育研究部工学基礎教育センター, "少数核子系散乱実験による核力の三体力効果の研究"
- 羽島 良一, 量子科学技術研究開発機構, "レーザー・コンプトン散乱ガンマ線、基礎と応用の間で"
- 黒田 直史, 東京大学大学院総合文化研究科広域科学専攻 相関基礎科学系, "反水素原子ビーム分光による基礎物理研究"
- M. Cargnelutti, Instrumentation Technologie, Slovenia, "An overview of beam diagnostics and readout electronics for particle accelerators"

- Vladimir Dubinko, National Science Centre Kharkov Institute of Physics and Technology, "Nuclear Fusion of Hydrogen Isotopes Induced by the Localized Anharmonic Vibrations"
- Tadeusz LESIAK, Institute of Nuclear Physics of the Polish Academy of Sciences, "QCD aspects at future e^+e^- colliders at the energy frontier"
- Tomasz SKWARNICKI, College of Arts and Sciences at Syracuse University, "Exotic Baryons"
- 浅川 誠, 関西大学, "低エネルギー電子バンチを用いたスミス・パーセル放射光源の開発"
- 齋藤 武彦, 理研、GSI、蘭州大学, "重イオンビームを用いたストレンジネス原子核研究：HypHI 実験と今後の計画について"
- 日野原 伸生, 筑波大学計算科学研究センター, "二重ベータ崩壊原子核行列要素の核構造計算"
- 藤原 守, 大阪大学核物理研究センター, "Sustainability medical isotope productions of ^{99m}Tc for SPECT inspection and of ^{18}F for PET inspection"
- 田辺 克明, 京都大学工学研究科, "凝縮系核融合の研究について"
- Michael Famiano, Western Michigan University, United States, "A Nuclear Physics Explanation of Biomolecular Homochirality: Theory and Experiment"

References

[1] Beam time schedule 2019A < https://www.lns.tohoku.ac.jp/archives/3250/ >

[2] Beam time schedule 2019B < https://www.lns.tohoku.ac.jp/archives/3635/ >

[3] Approved proposvals < https://www.lns.tohoku.ac.jp/users/saitaku/ >

[4] SNP School 2019 < https://lambda.phys.tohoku.ac.jp/snpsc2019/ >

Radiation Safety Report 2019

Radiatn Safety Office

放射線安全管理室より 2019 年度（平成 31 年 4 月～令和 2 年度 3 月）の報告を以下の通り行う。

§1. 許認可申請

令和元年 5 月 20 日　　承認使用に係る変更承認申請書の提出
令和元年 7 月 18 日　　変更の承認
令和元年 8 月 21 日　　放射線障害予防規程の改定、変更届の提出
令和 2 年 3 月 2 日　　原子力規制庁 立入検査

§2. 個人管理

2.1 放射線業務従事者登録

179人（ 東北大 77人　学外 84人　研究者以外 18人）

2.2 個人被ばく管理

1年間の個人被ばく線量　　5 mSv 以下　179人

2.3 教育訓練

定期講習（再教育のみ）　令和元年 10月 30日　82人

不定期の講習
（規程改正前）　再教育　11回　23人　　登録前教育（新規教育）9回　21人
（規程改正後）　再教育　12回　21人　　登録前教育（新規教育）20回　49人
　　変更点の周知　11回　20人

§3. 自主点検

年2回実施　　令和元年 9月20日、令和2年3月9日

§4. 放射性同位元素製造記録

2019 年度に本加速器施設で製造され，共同研究に使用された放射性同位元素は次のとお

り。

核種	数量（kBq）	核種	数量（kBq）
As-74	2	Na-24	5,000
Au-196	1,000	Nb-95	5,000
Ba-131	20	Ni-57	11,010
Ba-133m	1	Pm-143	100
Ba-135m	2,401	Ra-225	0.24
Ca-47	1,140	Rb-83	2.4
Co-57	1,106	Rb-84	2.4
Cs-132	204	Rb-86	40
Cs-136	2,040	Sc-46	19,000
Hg-203	302	Sc-48	1,000
K-42	28,100	Sr-85	180
K-43	143,240	Tl-202	302,000
Mo-99	12,000	V-48	4,000
Na-22	900	Zn-65	2
		全 28 核種	計 539793.04 kBq

§5. その他

菊永、武藤 受講予定の 2020/3/13 の主任者定期講習が、新型コロナウイルス感染拡大に伴い中止となった

III. List of Publication

List of Publication (論文リスト) (2019)

Papers Published in Refereed Journals

Profile measurement of circulating electrons in a synchrotron by inserting a carbon wire

Y. Obara, T. Ishikawa, H. Hama, F. Hinode, H. Kanda, S. Kashiwagi, M. Miyabe, T. Muto, K. Ozawa, H. Shimizu, A.O. Tokiyasu

Nucl. Inst. Meth. A 922, p.p. 108-113, (2019).

Light source based on a 100 mm-long monolithic undulator magnet with a very short 4 mm-period length

S. Yamamoto, S. Kashiwagi, S. Masuda, N. Nakanii, T. Hosokai, M. Kando, T. Muto, K. - Nanbu, F. Hinode and H. Hama

J. Synchrotron Rad. 26, 1902-1910, (2019).

Performance evaluation of a silicon strip detector for positrons/electrons from a pulsed a muon beam

T. Aoyagi, Y. Honda, H. Ikeda, M. Ikeno, K. Kawagoe, T. Kohriki, T. Kume, T. Mibe, K. Namba, S. Nishimura, N. Saito, O. Sasaki, N. Sato, Y. Sato, H. Sendai, K. Shimomura, S. Shirabe, M. Shoji, T. Suda, T. Suehara, T. Takatomi, M. Tanaka, J. Tojo, K. Tsukada, T. Uchida, T. Ushizawa, H. Wauke, T. Yamanak and T. Yoshioka

JINST 15(2020) P04027.

Energy of the 229Th Nuclear Clock Isomer Determined by Absolute γ-ray Energy Difference

A. Yamaguchi, H. Muramatsu, T. Hayashi, N. Yuasa, K. Nakamura, M. Takimoto, H. Haba, K. Konashi, M. Watanabe, H. Kikunaga, K. Maehata, N. Y. Yamasaki, K. Mitsuda

Physical Review Letters 123 (2019) 222501

Vertical Migration of Cs-137 in Japanese Orchards after the Fukushima Daiichi Nuclear Power Plant Accident

M. Sato, K. Matsuoka, T. Takase, NI Kobayshi, H. Kikunaga, D. Tanaka, K. Tanoi, T. Ohtsuki, S. Kusada, K. Yamaguchi

Horticulture Journal 88 (2019) 150-163

Dispersal rates of 225Ac in exhaust, surface, and waste water under chemical operations

T. Yamamura, K. Shirasaki, H. Kikunaga, K. Nagata, Z. Zhang, K. Washiyama, A. Toyoshima, T. Yoshimura, A. Shinohara

Radiation Safety Management (accepted)

Synthesis and Photoluminescence of Tetracyanidonitridorhenium(V) Complexes with Five-membered N-heteroaromatic Ligands and Photoluminescence-intensity Change

Moe Seike, Kojiro Nagata, Hayato Ikeda, Akitaka Ito, Eri Sakuda, Noboru Kitamura, Atsushi Shinohara, Takashi Yoshimura

ACS Omega, 4 (2019) 21251-21259.

Microvascular Dysfunction Related to Progressive Left Ventricular Remodeling due to Chronic Occlusion of the Left Anterior Descending Artery in an Adult Porcine Heart

Shin Yajima, Shigeru Miyagawa, Satsuki Fukushima, Kayako Isohashi, Tadashi Watabe, Hayato Ikeda, Genki Horitsugi, Akima Harada, Ryoto Sakaniwa, Jun Hatazawa, Yoshiki Sawa

International Heart Journal 60 (2019) 715–727.

Quantitative measurement of regional cerebral blood flow and oxygen metabolism in a rat model of cerebral hypoperfusion

Hiroki Kato, Yasukazu Kanai, Tadashi Watabe, Hayato Ikeda, Genki Horitsugi, Jun Hatazawa

Brain Research 1719, (2019) 208–216.

Distribution of LAT1-targeting PET tracer was independent of the tumor blood flow in rat xenograft models of C6 glioma and MIA PaCa-2

Masanao Aoki, Tadashi Watabe Shushi Nagamori, Sadahiro Naka, Hayato Ikeda, Pornparn Kongpracha, Genki Horitsugi, Yasukazu Kanai, Eku Shimosegawa, Yoshikatsu Kanai, Jun Hatazawa

Annals of Nuclear Medicine 33, (2019) 394–403.

Positron tracking detector for J-PARC muon g−2/EDM experiment

T. Yamanaka, T. Aoyagi, H. Ikeda, M. Ikeno, T. Ito, K. Ueno, T. Uchida, K. Kawagoe, T. Kishishita, T. Kume, T. Kohriki, N. Saito, O. Sasaki, T. Sata, N. Sato, Y. Sato, M. Shoji, S. Shirabe, T. Suehara, Y. Sue, T. Suda, H. Sendai, T. Takatomi, M. Tanaka, K. Tsukada, Y. Tsutsumi, J. Tojo, K. Namba, S. Nishimura, Y. Honda, M. Matama, T. Mibe, T. Murakami, H. Yasuda, and T. Yoshioka
NIMA 958 (2020) 162786.

Future Possibilities for Accelerators in Nuclear Physics
Shoji Nagamiya, Hideto En'yo, Hirokazu Tamura
Review of Accelerator Science and Technology 10 (2019) 13-32

Evidence for potassium transport acitivity of Arabidopsis KEA1-KEA6
Tsujii, M., Kera, K., Hamamoto, S., Kuromori, T., Shikanai, T., and Uozumi, N.
Sci. Rep., 9, 10040 (2019)

The mechanosensitive channel YbdG from Escherichia coil has a role in adaptation to osmotic up-shock
Amemiya, S., Toyoda, H. Kimura, M., Saito, H., Kobayashi, H., hara, K., Kamagata, K., Kawabata, R., Kato, S., Nakashimada, Y., Furuta, T., Hamamoto, S., and Uozumi, N.
J. Biol. Chem. 294, 12281-12292 (2019)

Guard cell membrane anion transport systems and their regulatory components: an eleborate mechanism controlling stress-induced stomatal closure
Saito, S. and Uozumi, N.
Plants 8, 9 (2019)

Cesium inhibits plant growth primarily through reduction of potassium influx and accumulation in Arabidopsis
Adams, E., Miyazaki, T., Saito, S., Uozumi, N. and Shin, R.
Plant Cell Physiol. 60 (1), 63-76 (2019)

DAY-LENGTH-DEPENDENT DELAYED-GREENING1, the Arabidopsis homolog of the cyanobacterial H+-extrusion protein, is essential for chloroplast pH regulation and optimization of non-photochemical quenching
Harada, K., Arizono, T., Sato, R., Trinh, M.D.L., Hashimoto, A., Kono, M., Tsujii, M., Uozumi, N., Takaichi, S., and Masuda, S.

Plant Cell Physiol. 60 (12), 2660–2671 (2019)

Relativistic corrections to the binding energy of positronic alkali-metal atoms
Takuma Yamashita, Yasushi Kino
Physical Review A, 100 (2019) 062511 (12 pages).

Correlation of Radiocesium Activity between Muscle and Peripheral Blood of Live Cattle Depending on Presence or Absence of Radiocontamination in Feed
Masatoshi Suzuki, Hidehiko Suzuki, Hirotoshi Ishiguro, Yosuke Saito, Satoshi Watanabe, Tomoyuki Kozutsumi, Yuichiro Sochi, Kiyoshi Nishi, Yusuke Urushihara, Yasushi Kino, Takashi Numabe, Tsutomu Sekine, Koichi Chida, and Manabu Fukumoto
Radiation Research, 192 (2019) 589-601.

Synthesis, structures, redox properties, and theoretical calculations of thiohalide capped octahedral hexanuclear technetium(III) clusters
Takashi Yoshimura, Kojiro Nagata, Ayumi Matsuda, Toshiki Omote, Yasushi Kino, Tsutomu Takayama, Tsutomu Sekine and Atsushi Shinohara
Dalton Transactions, 48 (2019) 14085-14095.

Four-body treatment of the antihydrogen-positronium system: binding, structure, resonant states and collisions
Piotr Froelich, Yasushi Kino, Emiko Hiyama, Takuma Yamashita, Konrad Piszczatowski, Svante Jonsell
Hyperfine Interactions, 240 (2019) 46 (16 pages).

Analysis of Radioactive Elements in Testes of Large Japanese Field Mice Using an Electron Probe Micro-Analyser after the Fukushima Accident
Takuya Ohdaira, Kanna Meguro, Kazuki Komatsu, Rina Syoji, Yohei Fujishima, Valerie Swee Ting Goh, Kosuke Kasai, Kentaro Ariyoshi, Akifumi Nakata, Yusuke Urushihara, Kazuma Koarai, Yasushi Kino, Tsutomu Sekine, Masatoshi Suzuki, Atsushi Takahasi, Yoshinaka Shimizu, Hisashi Shinoda, Mitsuaki A Yoshida, Manabu Fukumoto, Hideaki Yamashiro, Tomisato Miura
Ionizing and Non-ionizing Radiation, IntechOpen, UK, (2019) 9 pages

Intestinal bacteria as powerful trapping lifeforms for the elimination of radioactive cesium

Kazuki Saito, Kengo Kuroda, Rie Suzuki, Yasushi Kino, Tsutomu Sekine, Hisashi Shinoda, Hideaki Yamashiro, Tomokazu Fukuda, Jin Kobayashi, Yasuyuki Abe, Junko Nishimura, Yusuke Urushihara, Hiroshi Yoneyama, Manabu Fukumoto, Emiko Isogai

Frontiers in veterinary science, 6 (2019) 70 (8pages)

Time-dependent Hartree-Fock plus Langevin approach for hot fusion reactions to synthesize the superheavy element with Z=120

K. Sekizawa and K. Hagino

Phys. Rev. C99, 051602(R) (2019) (5 pages).

Potential model for nuclear astrophysical fusion reactions with a square-well potential

R. Ogura, K. Hagino, and C.A. Bertulani

Phys. Rev. C99, 065808 (2019) (4 pages).

Sub-barrier fusion involving odd mass nuclei: the case of $^{36}S+^{50}Ti,^{51}V$

G. Colucci, G. Montagnoli, A.M. Stefanini, K. Hagino, A. Caciolli, P. Colovic, L. Corradi, E. Fioretto, F. Galtarossa, A. Goasdu, J. Grebosz, M. Mazzocco, D. Montanari, C. Parascandolo, F. Scarlassara, M. Siciliano, E. Strano, S. Szilner and N. Vukman

Euro. Phys. J. A55, 111 (2019) (6 pages).

Dissipation and tunneling in heavy-ion reactions near the Coulomb barrier

E. Piasecki, M. Kowalczyk, S. Yusa, A. Trzcinska, and K. Hagino

Phys. Rev. C100, 014616 (2019) (11 pages)

ラザフォードの指導を受けた日本人若手研究者―S. Obaとは誰か

萩野浩一、小林良彦、豊田直樹、中村哲

日本物理学会誌 74(9), 655-658 (2019).

Subbarrier fusion reactions of an aligned deformed nucleus

K. Hagino and S. Sakaguchi

Phys. Rev. C100, 064614 (2019) (6 pages).

A new approach for open quantum systems based on a phonon number representation of a harmonic oscillator bath
M. Tokieda and K. Hagino
Ann. of Phys. 412, 168005 (2020) (29 pages).

Constraining the $^{12}C+^{12}C$ astrophysical S-factors with the $^{12}C+^{13}C$ measurements at very low Energies
N.T. Zhang, X.Y. Wang, H. Chen, Z.J. Chen, W.P. Lin, X.D. Tang, W.Y. Xin, S.W. Xu, D. Tudor, A.I. Chilug, I.C. Stefanescu, M. Straticiuc, I. Burducea, D.G. Ghita, R. Margineanu, C. Gomoiu, A. Pantelica, D. Chesneanu, L. Trache, B. Bucher, L.R. Gasques, K. Hagino, S. Kubono, Y.J. Li, C.J. Lin, A.S. Umar, and Y. Xu
Phys. Lett. B801, 135170 (2020) (5 pages).

Resonance width for a particle-core coupling model with a square-well potential
K. Hagino, H. Sagawa, S. Kanaya, and A. Odahara
Prog. Theo. Exp. Phys. 2000, 023D01 (2020) (19 pages).

Time-dependent approaches to open quantum systems
M. Tokieda and K. Hagino
Frontiers Phys. 8, 8 (2020) (8 pages).

Fusion Dynamics for Hot Fusion Reactions to Synthesize Superheavy Nuclei revealed in Quasielastic Barrier Distributions
T. Tanaka, K. Morita, K. Morimoto, D. Kaji, H. Haba, R.A. Boll, N. T. Brewer, S. Van Cleve, D.J. Dean, S. Ishizawa, Y. Ito, Y. Komori, K. Nishio, T. Niwase, B.C. Rasco, J.B. Roberto, K.P. Rykaczewski, H. Sakai, D.W. Stracener, and K. Hagino
Phys. Rev. Lett. 124, 052502 (2020) (6 pages).

An overview of the scientific contribution of Andrea Vitturi to Nuclear Physics
L. Fortunato, C.E. Alonso, J.M. Arias, J. Casal, K. Hagino, J.A. Lay, E.G. Lanza, S.M. Lenzi, J. Lubian, T. Oishi, F. Perez-Bernal
Euro. Phys. J. A56, 49 (2020) (25 pages).

Image-processing the topological charge density in the CP(N-1) model
Y. Abe, K. Fukushima, Y. Hidaka, H. Matsueda, K. Murase and S. Sasaki.
Prog. Theor. Exp. Phys. (2020) 013D02.

Hadron Physics at J-PARC

Hiroaki Ohnishi, Fuminori Sakuma and Toshiyuki Takahashi

Prog.Part.Nucl.Phys. (2020) 103773

Measurement of neutral pion photoproduction off the proton with the large acceptance electromagnetic calorimeter BGOegg

N. Muramatsu, J. K. Ahn, W. C. Chang, J. Y. Chen, M. L. Chu, S. Daté, T. Gogami, H. Goto, H. Hamano, T. Hashimoto, Q. H. He, K. Hicks, T. Hiraiwa, Y. Honda, T. Hotta, H. Ikuno, Y. Inoue, T. Ishikawa, I. Jaegle, J. M. Jo, Y. Kasamatsu, H. Katsuragawa, S. Kido, Y. Kon, S. Masumoto, Y. Matsumura, M. Miyabe, K. Mizutani, T. Nakamura, T. Nakano, T. Nam, T. N. T. Ngan, M. Niiyama, Y. Nozawa, Y. Ohashi, H. Ohnishi, T. Ohta, K. Ozawa, C. Rangacharyulu, S. Y. Ryu, Y. Sada, M. Sasagawa, T. Shibukawa, H. Shimizu, R. Shirai, K. Shiraishi, E. A. Strokovsky, Y. Sugaya, M. Sumihama, S. Suzuki, S. Tanaka, A. Tokiyasu, N. Tomida, Y. Tsuchikawa, T. Ueda, H. Yamazaki, R. Yamazaki, Y. Yanai, T. Yorita, C. Yoshida, and M. Yosoi

Phys. Rev. C 100(2019), 055202

Nuclear dependence of light neutral meson production in p-A collisions at 400 GeV with NA60

R. Arnaldi, K. Banicz, K. Borer, J. Castor, B. Chaurand, W. Chen, C. Cicalò, A. Colla, P. Cortese, S. Damjanovic, A. David, A. De Falco, A. Devaux, L. Ducroux, H. En'yo, J. Fargeix, A. Ferretti, M. Floris, A. Förster, P. Force, N. Guettet, A. Guichard, H. Gulkanian, J. M. Heuser, P. Jarron, M. Keil, L. Kluberg, Z. Li, C. Lourenço, J. Lozano, F. Manso, P. Martins, A. Masoni, A. Neves, H. Ohnishi, C. Oppedisano, P. Parracho, P. Pillot, T. Poghosyan, G. Puddu, E. Radermacher, P. Ramalhete, P. Rosinsky, E. Scomparin, J. Seixas, S. Serci, R. Shahoyan, P. Sonderegger, H. J. Specht, R. Tieulent, A. Uras, G. Usai, R. Veenhof, H. K. Wöhri

Eur.Phys.J.C 79 (2019) 5, 443

Position tracking detector for J-PARC muon g-2/EDM experiment

T. Yamanaka, T. Aoyagi, H. Ikeda, M.Ikeno, T.Ito, K.Ueno,, T.Uchida, K.Kawagoe, T.Kishishita, T.Kume, T.Kohriki, N.Saito, O.Sasaki, T.Sata, N.Sato, Y.Sato, M.Shoji, S.Shirabe, T.Suehara, Y.Sue, T.Suda, H.Sendai, T.Takatomi, M.Tanaka, K.Tsukada, Y.Tsutsumi, J.Tojo, K.Namba, S.Nishimura, Y.Honda, M.Matama, T. Mibe, T. Murakami, H. Yasuda, T. Yoshioka

Nuclear Instruments and Methods in Physics A958 (2020) 162786

Recent Progress and Prospects of the LEPS2/BGOegg Experiment at SPring-8

N. Muramatsu for the LEPS2/BGOegg Collaboration

Acta Physica Polonica B 51 No.1 (2020) 231–238.

Non-strange dibaryons studied in the $\gamma d \to \pi^0 \pi^0 d$ reaction

T. Ishikawa, H. Fujimura, H. Fukasawa, R. Hashimoto, Q. He, Y. Honda, T. Iwata, S. Kaida, H. Kanda, J. Kasagi, A. Kawano, S. Kuwasaki, K. Maeda, S. Masumoto, M. Miyabe, F. Miyahara, K. Mochizuki, N. Muramatsu, A. Nakamura, K. Nawa, S. Ogushi, Y. Okada, K. Okamura, Y. Onodera, K. Ozawa, Y. Sakamoto, M. Sato, H. Shimizu, H. Sugai, K. Suzuki, Y. Tajima, Y. Taniguchi, Y. Tsuchikawa, H. Yamazaki, R. Yamazaki, H.Y. Yoshida.

Phys. Lett. B 789, 413 (2019).

ηN Scattering Parameters and Possible η'd Bound State from η Photoproduction on the Deuteron

T. Ishikawa, K. Aoki, H. Fujimura, H. Fukasawa, H. Fujioka, R. Hashimoto, Q. He, Y. Honda, T. Hotta, Y. Inoue, K. Itahashi, T. Iwata, S. Kaida, H. Kanda, J. Kasagi, A. Kawano, S. Kusawaki, H. Kawai, K. Maeda, S. Masumoto, Y. Matsumura, M. Miyabe, F. Miyahara, K. Mochizuki, S. Miyata, N. Muramatsu, A. Nakamura, K. Nawa, T. Nishi, S. Ohgushi, Y. Okada, H. Ohnishi, Y. Onodera, K. Ozawa, Y. Sakamoto, M. Sato, H. Shimizu, H. Sugai, K. Suzuki, R. Shirai, M. Tabata, Y. Tajima, S. Takahashi, Y. Taniguchi, A.O. Tokiyasu, Y. Tsuchikawa, H. Yamazaki, R. Yamazaki, C. Yoshida, H.Y. Yoshida

Acta Phys.Polon.B 51 (2020) 27-32

"K^-pp", a Kbar-meson nuclear bound state, observed in ^{3}He(K^-, Λp)n reactions

J-PARC E15 collaboration, S. Ajimura, H. Asano, G. Beer, C. Berucci, H. Bhang, M. Bragadireanu, P. Buehler, L. Busso, M. Cargnelli, S. Choi, C. Curceanu, S. Enomoto, H. Fujioka, Y. Fujiwara, T. Fukuda, C. Guaraldo, T. Hashimoto, R. S. Hayano, T. Hiraiwa, M. Iio, M. Iliescu, K. Inoue, Y. Ishiguro, T. Ishikawa, S. Ishimoto, K. Itahashi, M. Iwasaki, K. Kanno, K. Kato, Y. Kato, S. Kawasaki, P. Kienle, H. Kou, Y. Ma, J. Marton, Y. Matsuda, Y. Mizoi, O. Morra, T. Nagae, H. Noumi, H. Ohnishi, S. Okada, H. Outa, K. Piscicchia, Y. Sada, A. Sakaguchi, F. Sakuma, M. Sato, A. Scordo, M. Sekimoto, H. Shi, K. Shirotori, D. Sirghi, F. Sirghi, K. Suzuki, S. Suzuki, T. Suzuki, K. Tanida, H. Tatsuno, M. Tokuda, D. Tomono, A. Toyoda, K. Tsukada, O. Vazquez Doce, E. Widmann, T. Yamaga,

T. Yamazaki, Q. Zhang, J. Zmeskal
Physics Letters B 789 (2019) 620-625.

Proton form factor ratio $\mu_p G_E^p/G_M^p$ from double spin asymmetry

A. Liyanage, W. Armstrong, H. Kang, J. Maxwell, J. Mulholland, L. Ndukum, A. Ahmidouch, I. Albayrak, A. Asaturyan, O. Ates, H. Baghdasaryan, W. Boeglin, P. Bosted, E. Brash, C. Butuceanu,M. Bychkov, P. Carter, C. Chen, J.-P. Chen, S. Choi, E. Christy, S. Covrig, D. Crabb, S. Danagoulian, A. Daniel, A. M. Davidenko, B. Davis, D. Day, W. Deconinck, A. Deur, J. Dunne, D. Dutta, L. El Fassi, M. Elaasar, C. Ellis, R. Ent, D. Flay, E. Frlez, D. Gaskell, O. Geagla, J. German, R. Gilman, T. Gogami, J. Gomez, Y. M. Goncharenko, O. Hashimoto, D. Higinbotham, T. Horn, G. M. Huber, M. Jones, M. K. Jones, N. Kalantarians, H.-K. Kang, D. Kawama, C. Keppel, M. Khandaker, Y. Kim, P. M. King, M. Kohl, K. Kovacs, V. Kubarovsky, Y. Li, N. Liyanage, V. Mamyan, P. Markowitz, T. Maruta, Y. M. Melnik, Z.-E. Meziani, A. Mkrtchyan, H. Mkrtchyan, V. V. Mochalov, P. Monaghan, A. Narayan, S. N. Nakamura, Nuruzzaman, L. Pentchev, D. Pocanic, M. Posik, A. Puckett, X. Qiu, J. Reinhold, S. Riordan, J. Roche, O. A. Rondón, B. Sawatzky, M. Shabestari, K. Slifer, G. Smith, L. F. Soloviev, P. Solvignon, V. Tadevosyan, L. Tang, A. N. Vasiliev, M. Veilleux, T. Walton, F. Wesselmann, S. A. Wood, H. Yao, Z. Ye, and L. Zhu (SANE Collaboration)
Physical Review C 101(2020) 035206-1-12

Decay pion spectroscopy: A new approach

A.Margaryan, R.Ajvazyan, N.Grigoryan, V.Kakoyan, V.Khachatryan, H.Vardanyan, S.Zhamkochyan, P.Achenbach, J.Pochodzalla, S.N.Nakamura, S.Nagao, Y.Toyama, J.R.M.Annand, K.Livingston, R.Montgomery
Nucl. Inst. and Meth. A 935 (2019) 40-50

Search for $K_L \to \pi^0 \nu\bar{\nu}$ and $K_L \to \pi^0 X^0$ Decays at the J-PARC KOTO Experiment

J. K. Ahn, B. Beckford, J. Beechert, K. Bryant, M. Campbell, S. H. Chen, J. Comfort, K. Dona, N. Hara, H. Haraguchi, Y. B. Hsiung, M. Hutcheson, T. Inagaki, I. Kamiji, N. Kawasaki, E. J. Kim, J. L. Kim, Y. J. Kim, J. W. Ko, T. K. Komatsubara, K. Kotera, A. S. Kurilin, J. W. Lee, G. Y. Lim, C. Lin, Q. Lin, Y. Luo, J. Ma, Y. Maeda, T. Mari, T. Masuda, T. Matsumura, D. Mcfarland, N. McNeal, J. Micallef, K. Miyazaki, R. Murayama, D. Naito, K. Nakagiri, H. Nanjo, H. Nishimiya, T. Nomura, M. Ohsugi, H. Okuno, M. Sasaki, N. Sasao, K. Sato, T. Sato, Y. Sato, H. Schamis, S. Seki,

N. Shimizu, T. Shimogawa, T. Shinkawa, S. Shinohara, K. Shiomi, S. Su, Y. Sugiyama, S. Suzuki, Y. Tajima, M. Taylor, M. Tecchio, M. Togawa, Y. C. Tung, Y. W. Wah, H. Watanabe, J. K. Woo, T. Yamanaka, and H. Y. Yoshida
Phys. Rev. Lett. 122, (2019) 021802 1-6

Profile measurement of circulating electrons in a synchrotron by inserting a carbon wire
Y. Obara, T. Ishikawa, H. Hama, F. Hinode, H. Kanda, S. Kashiwagi, M. Miyabe, T. Muto, K. Ozawa, H. Shimizu, A.O. Tokiyasu
Nucl. Instr. Meth. A922 (2019) 108.

Anomalous Heat Effects Induced by Metal Nano-composites and Hydrogen Gas
Y. Iwamura, T. Itoh, J. Kasagi, A. Kitamura, A. Takahashi, K. Takahashi, R. Seto, T. Hatano, T. Hioki, T. Motohiro, M. Nakamura, M. Uchimura, H. Takahashi, S. Sumitomo, Y. Furuyama. M. Kishida and H. Matsune,
J. Condensed Matter Nucl. Sci. 29 (2019) 119–128.

Papers Published in Conference Proceedings, Books etc.

Characteristics of Polarized Coherent Radiation in THz Region from a Crossed Undulator
H. Saito, H. Hama, F. Hinode, K. Kanomata, S. Kashiwagi, S. Miura, N.M. Morita, T. Muto, I. Nagasawa, K. Nanbu, S. Ninomiya, K. Takahashi, H. Yamada
10th Int. Particle Accelerator Conf. (IPAC'19), Melbourne, 1769-1771, (2019).

Status of Test-Accelerator as Coherent THz Source at ELPH, Tohoku University
S. Kashiwagi, H. Hama, F. Hinode, K. Kanomata, S. Miura, N.M. Morita, T. Muto, I. Nagasawa, K. Nanbu, S. Ninomiya, H. Saito, K. Takahashi, H. Yamada
10th Int. Particle Accelerator Conf. (IPAC2019), Melbourne, 1475-1477, (2019).

Measurement of Cherenkov Diffraction Radiation from Short Electron Bunches at t-ACTS
S. Ninomiya, H. Hama, F. Hinode, K. Kanomata, S. Kashiwagi, S. Miura, N.M. Morita, T. Muto, I. Nagasawa, K. Nanbu, H. Saito, K. Takahashi, H. Yamada
10th Int. Particle Accelerator Conf. (IPAC'19), Melbourne, 2536-2538, (2019).

Crossed-Undulator Configuration for Variable Polarized THz Source

H. Saito, H. Hama, S. Kashiwagi, N.M. Morita, T. Muto, K. Nanbu, H. Yamada
39th Free Electron Laser Conf. (FEL2019), Hamburg, Germany, 69-72, (2019).

コヒーレントスミス=パーセル放射を用いた非破壊型バンチ長モニターの研究
山田 悠樹，日出 富士雄，柏木 茂，武藤 俊哉，三浦 禎雄，南部 健一，髙橋 健，長澤 育郎，鹿又 健，齊藤 寛峻，森田 希望，濱 広幸
日本加速器学会 第16回年会プロシーディングス, (2019), 40-42

交叉型アンジュレータにおける移相器の設計と開発
森田 希望，柏木 茂，日出 富士夫，三浦 禎雄，武藤 俊哉，南部 健一，長澤 育郎，髙橋 健，鹿又 健，柴田 晃太郎，齋藤 寛峻，山田　悠樹，濱 広幸
日本加速器学会 第16回年会プロシーディングス, (2019), 157-160

極短周期アンジュレータの開発と光源性能評価試験
山本 樹，益田 伸一，浜 広幸，柏木 茂，日出 富士雄，武藤 俊哉，南部 健一
日本加速器学会 第16回年会プロシーディングス, (2019), 170-174

交叉型アンジュレータからのTHz域コヒーレント放射の偏光特性(II)
齊藤 寛峻，柏木 茂，日出 富士雄，三浦 禎雄，武藤 俊哉，南部 健一，長澤 育郎，髙橋 健，鹿又 健，柴田 晃太朗，森田 希望，山田 悠樹，石附 勇人，寺田 健人，濱 広幸
日本加速器学会 第16回年会プロシーディングス, (2019), 445-448

テラヘルツコヒーレントアンジュレータ放射の偏光制御
柏木 茂，齊藤 寛峻，全 炳俊，入澤 明典，日出 富士雄，武藤 俊哉，森田 希望，山田 悠樹，南部 健一，鹿又 健，髙橋 健，長澤 育郎，柴田 晃太朗，三浦 禎雄，濱 広幸
日本加速器学会 第16回年会プロシーディングス, (2019), 747-750

t-ACTSにおける中空誘電体からのチェレンコフ光の測定
南部 健一，日出 富士雄，柏木 茂，武藤 俊哉，齊藤 寛峻，森田 希望，山田 悠樹，鹿又 健，髙橋 健，長澤 育郎，柴田 晃太朗，三浦 禎雄，濱 広幸
日本加速器学会 第16回年会プロシーディングス, (2019), 1122-1124

東北大学電子光理学研究センター加速器群の現状
日出 富士雄，柏木 茂，鹿又 健，柴崎 義信，柴田 晃太朗，髙橋 健，長澤 育郎，

南部 健一，三浦 禎雄，武藤 俊哉，濱 広幸
日本加速器学会 第16回年会プロシーディングス, (2019), 1279-1281

Λ(1405) Spectroscopy via the In-flight d(K^-, n) Reaction at the J-PARC K1.8BR

Shingo Kawasaki, Shu Aikawa, Shuhei Ajimura, Takaya Akaishi, Hidemitsu Asano, George Beer, Carolina Berruci, Mario Bragadireanu, Paul Buehler, Luigi Busso, Michael Cargnelli, Seonho Choi, Catalina Curceanu, Shun Enomoto, Hiroyuki Fujioka , Yuya Fujiwara, Tomokazu Fukuda, Carlo Guaraldo, Tadashi Hashimoto, Ryugo S. Hayano, Toshihiko Hiraiwa, Masami Iio, Mihai Iliescu, Kentaro Inoue, Yosuke Ishiguro, Takashi Ishikawa, Shigeru Ishimoto, Kenta Itahashi, Masaaki Iwai, Masahiko Iwasaki, Koki Kanno, Kazuma Kato, Yuko Kato, Paul Kienle, Yusuke Komatsu, Hirofumi Kou, Yue Ma, Johann Marton, Yasuyuki Matsuda, Yutaka Mizoi, Ombretta Morra, Tomofumi Nagae, Hiroyuki Noumi, Hiroaki Ohnishi, Shinji Okada, Zhadyra Omar, Haruhiko Outa, Kristian Piscicchia, Yuta Sada, Atsushi Sakaguchi, Fuminori Sakuma, Masaharu Sato, Alessandro Scordo, Michiko Sekimoto, Hexi Shi, Kotaro Shirotori, Diana Sirghi, Florin Sirghi, Ken Suzuki, Shoji Suzuki, Takatoshi Suzuki, Kiyoshi Tanida, Hideyuki Tatsuno, Atsushi O. Tokiyasu, Makoto Tokuda, Dai Tomono, Akihisa Toyoda, Kyo Tsukada, Oton Vazquez Doce, Eberhard Widmann, Takumi Yamaga, Toshimitsu Yamazaki, Heejoong Yim, Qi Zhang, and Johann Zmeskal
JPS Conf. Proc. 26 (2019) 022009

Results of KbarNN Search via the (K^-,n) Reaction at J-PARC

Takumi Yamaga, Shuhei Ajimura, Hidemitsu Asano, George Beer, Carolina Berruci, Hyeongchan Bhang, Mario Bragadireanu, Paul Buehler, Luigi Busso, Michael Cargnelli, Seonho Choi, Catalina Curceanu, Shun Enomoto, Hiroyuki Fujioka, Yuya Fujiwara, Tomokazu Fukuda, Carlo Guaraldo, Tadashi Hashimoto, Ryugo S. Hayano, Toshihiko Hiraiwa, Masami Iio, Mihai Iliescu, Kentaro Inoue, Yosuke Ishiguro, Takashi Ishikawa, Shigeru Ishimoto, Kenta Itahashi, Masahiko Iwasaki, Koki Kanno, Kazuma Kato, Yuko Kato, Shingo Kawasaki, Paul Kienle, Hirofumi Kou, Yue Ma, Johann Marton, Yasuyuki Matsuda, Yutaka Mizoi, Ombretta Morra, Tomofumi Nagae, Hiroyuki Noumi, Hiroaki Ohnishi, Shinji Okada, Haruhiko Outa, Kristian Piscicchia, Yuta Sada, Atsushi Sakaguchi, Fuminori Sakuma, Masaharu Sato, Alessandro Scordo, Michiko Sekimoto, Hexi Shi, Kotaro Shirotori, Diana Sirghi, Florin Sirghi, Ken Suzuki, Shoji Suzuki, Takatoshi Suzuki, Kiyoshi Tanida, Hideyuki Tatsuno, Makoto Tokuda, Dai Tomono, Akihisa Toyoda, Kyo Tsukada, Oton Vazquez Doce, Eberhard Widmann, Toshimitsu Yamazaki, Qi Zhang, and Johann Zmeskal

JPS Conf. Proc. 26 (2019) 023008

Kaonic Atom Experiments at J-PARC

T. Hashimoto, S. Aikawa, S. Ajimura, T. Akaishi, H. Asano, M. Bazzi, G. Beer, D. Bennett, C. Berucci, D. Bosnar, M. Bragadireanu, P. Bhler, L. Busso, A. D. Butt, M. Cargnelli, Seonho Choi, C. Curceanu, W. B. Doriese, M. S. Durkin, S. Enomoto, Y. Ezoe, J. W. Fowler, H. Fujioka, T. Fukuda, C. Guaraldo, F. P. Gustafsson, C. Han, R. Hayakawa, R. S. Hayano, T. Hayashi, J. P. Hays-Wehle, G. C. Hilton, T. Hiraiwa, Y. Ichinohe, M. Iio, Y. Iizawa, M. Iliescu, K. Inoue, S. Ishimoto, Y. Ishisaki, K. Itahashi, M. Iwasaki, S. Kawasaki, Y. Ma4, J. Marton, Y. Matsuda, Y. Mizoi, O. Morra, T. Murakami, T. Nagae, T. Nishi, H. Noda, H. Noumi, K. Nunomura, G. C. O'Neil, T. Ohashi, H. Ohnishi, S. Okada, H. Outa, K. Piscicchia, C. D. Reintsema, Y. Sada, A. Sakaguchi, F. Sakuma, M. Sato, D. R. Schmidt, A. Scordo, M. Sekimoto, H. Shi, K. Shirotori, D. Sirghi, F. Sirghi, K. Suzuki, S. Suzuki, T. Suzuki, D. S. Swetz, A. Takamine, K. Tanida, H. Tatsuno, D. Tomono, A. Toyoda, C. Trippl, K. Tsukada, J. Uhlig, J. N. Ullom, O. Vazquez Doce, E. Widmann, S. Yamada, T. Yamaga, T. Yamazaki, and J. Zmeskal
JPS Conf. Proc. 26 (2019) 023013

Electron scattering from ^{208}Pb and ^{132}Xe ions at the SCRIT facility

Kyo Tsukada, Kousuke Adachi, Akitomo Enokizono, Takahiro Fujita, Masahiro Hara, Toshitada Hori, Mitsuki Hori, Shin-ichi Ichikawa, Keita Kasama, Kazuyoshi Kurita, Kazuki Namba, Tetsuya Ohnishi, Toshimi Suda, Tadaaki Tamae, Mamoru Togasaki, Masanori Wakasugi, Masamitsu Watanabe, Kouhei Yamada
Hyperfine Interact. 240 (2019) 1, 102

Spectroscopic study of the Λ (1405) resonance via the d(K^-,n) reaction at J-PARC

H. Asano, S. Aikawa, S. Ajimura, T. Akaishi, G. Beer, C. Berucci, M. Bragadireanu, P. Buehler, L. Busso, M. Cargnelli, S. Choi, C. Curceanu, S. Enomoto, H. Fujioka, Y. Fujiwara, T. Fukuda, C. Guaraldo, T. Hashimoto, R. S. Hayano, T. Hiraiwa, M. Iio, M. Iliescu, K. Inoue, Y. Ishiguro, T. Ishikawa, S. Ishimoto, K. Itahashi, M. Iwai, M. Iwasaki, K. Kanno, K. Kato, Y. Kato, S. Kawasaki, P. Kienle, Y. Komatsu, H. Kou, Y. Ma, J. Marton, Y. Matsuda, Y. Mizoi, O. Morra, T. Nagae, H. Noumi, H. Ohnishi, S. Okada, Z. Omar, H. Outa, K. Piscicchia, Y. Sada, A. Sakaguchi, F. Sakuma, M. Sato, A. Scordo, M. Sekimoto, H. Shi, K. Shirotori, D. Sirghi, F. Sirghi, K. Suzuki, S. Suzuki, T. Suzuki, K. Tanida, H. Tatsuno, A. O. Tokiyasu, M. Tokuda,

D. Tomono, A. Toyoda, K. Tsukada, O. Vazquez Doce, E. Widmann, T. Yamaga, T. Yamazaki, H. Yim, Q. Zhang, and J. Zmeskal
AIP Conf. Proc. 2130 (2019) 1, 0400183

Spectroscopy of pionic atoms in ^{122}Sn(d,^{3}He) reaction and angular dependence of the formation cross sections

T. Nishi, K. Itahashi, G. P. A. Berg, H. Fujioka, N. Fukuda, N. Fukunishi, H. Geissel, R. S. Hayano, S. Hirenzaki, K. Ichikawa, N. Ikeno, N. Inabe, S. Itoh, M. Iwasaki, D. Kameda, S. Kawase, T. Kubo, K. Kusaka, H. Matsubara, S. Michimasa, K. Miki, G. Mishima, H. Miya, H. Nagahiro, M. Nakamura, S. Noji, K. Okochi, S. Ota, N. Sakamoto, K. Suzuki, H. Takeda, Y. K. Tanaka, K. Todoroki, K. Tsukada, T. Uesaka, Y. N. Watanabe, H. Weick, H. Yamakami, and K. Yoshida
RIKEN Accel. Prog. Rep. 52 (2019) 91

Precise magnetic field measurement of WiSES

H. Wauke, A. Enokizono, Y. Honda, K. Sasama, T. Ohnishi, T. Suda, S. Takayama, T. Tamae, K. Tsukada, M. Wakasugi, and M. Watanabe
RIKEN Accel. Prog. Rep. 52 (2019) 145

Design of an Ion Source for the eSHE project Toward Pioneering Electron Scattering on Superheavy Elements

S. Naimi, T. K. Sato, K. Tsukada, P. Schury, Y. Ito, H. Haba, Y. Komori, T. Ohnishi, and T. Uesaka
RIKEN Accel. Prog. Rep. 52 (2019) 151

Status of Accelerator Facilities in FY2018

F. Hinode, K. Kanomata, S. Kashiwagi, S. Miura, T. Muto, I. Nagasawa, K. Nanbu,
Y. Shibasaki, K. Takahashi and H. Hama
ELPH Annual Report, Tohoku University (2018), 129-133

Development of simultaneous production method for carrier-free RI multitracer of potassium, rubidium and cesium

H. Ikeda, H. Kikunaga, H. Watabe
ELPH Annual Report 2018 (2019) 116–119.

Column chromatography of astatine using weak base anion exchange resin
H. Ikeda, H. Kikunaga, Y. Komori, T. Yokokita, D. Mori, H. Haba, and H. Watabe
RIKEN Accelerator Progress Report 2018 Vol. 52 (2019) 203.

Production of arsenic RI tracer from gallium oxide target by alpha beam irradiation
H. Ikeda, H. Kikunaga, Y. Komori, T. Yokokita, D. Mori, H. Haba, and H. Watabe
RIKEN Accelerator Progress Report 2018 Vol. 52 (2019) 206.

Cold Fusion：Advances in Condensed Matter
J. Kasagi, Y. Honda and K. Fang,
Nuclear Science (Elsevier Inc., 2020), pp 167-187.

Present status and prospect of nuclear physics with strangeness—summary of HYP2018
H. Tamura
Proc. 13th International Conference on Hypernuclear and Strange Particle Physics (HYP 2018), AIP Conference Proceedings 2130 (2019) 60001

Observation of a Ξ bound state in the $^{12}C(K^-,K^+)$ reaction at 1.8 GeV/c
T. Nagae et al.
Proc. 13th International Conference on Hypernuclear and Strange Particle Physics (HYP 2018), AIP Conference Proceedings 2130 (2019) 20015

K^{bar} and nucleus system studied by $^{12}C(K^-,p)$ spectrum
Y. Ichikawa et al.
Proc. 13th International Conference on Hypernuclear and Strange Particle Physics (HYP 2018), AIP Conference Proceedings 2130 (2019) 40017

Σp scattering experiment at J-PARC － results of commissioning run
K. Miwa et al.
Proc. 13th International Conference on Hypernuclear and Strange Particle Physics (HYP 2018), AIP Conference Proceedings 2130 (2019) 20006

Strangeness Nuclear Physics
H. Tamura
Proc. 8th International Conference on Quarks and Nuclear Physics (QNP2018),

JPS Conference Proceedings 26 (2019) 11003

First γ-Ray Spectroscopy of an sd-Shell Hypernucleus, ${}^{19}_{\Lambda}F$

S.B. Yang et al.

Proc. 8th International Conference on Quarks and Nuclear Physics (QNP2018),

JPS Conference Proceedings 26 (22019) 23015

Study of Y in Nuclei through C(K⁻, π⁺)X Spectrum at 1.8 GeV/c in the J-PARC E05 Experiment*

R. Honda et al.

Proc. 8th International Conference on Quarks and Nuclear Physics (QNP2018),

JPS Conference Proceedings 26 (2019) 23014

Status of the J-PARC E07, Systematic Study of Double Strangeness Nuclei with the Hybrid Emulsion Method

J. Yoshida et al.

Proc. 8th International Conference on Quarks and Nuclear Physics (QNP2018),

JPS Conference Proceedings 26 (2019) 23006

A Σp scattering Experiment at J-PARC and the Analysis Status

Y. Nakada et al.

Proc. 8th International Conference on Quarks and Nuclear Physics (QNP2018),

JPS Conference Proceedings 26 (2019) 23024

The Ξ⁻ Atom X-ray Spectroscopy at J-PARC

M. Fujita et al.

Proc. 8th International Conference on Quarks and Nuclear Physics (QNP2018),

JPS Conference Proceedings 26 (2019) 31016

Operation of Multi-MPPC System for Cylindrical Scintillation Fiber Tracker

Y. Akazawa et al.

Proc. 5th International Workshop on New Photon Detectors (PD18),

JPS Conference Proceedings 27 (2019) 011008

基礎科学で未来をつくる―科学的意義と社会的意義

田村裕和、村山斉、櫻井博儀、常田佐久、前野悦輝、岡本拓司、中村幸司、梶田隆章

丸善出版、 2019.

微生物TRPチャネルの機能と役割

魚住信之，山下敦子

TRPチャネルのすべて　医学のあゆみ 270巻10号　医歯薬出版　(2019)

Muon catalyzed fusion, present and future

Atsuo Iiyoshi, Yasushi Kino, Motoyasu Sato, Yoshiharu Tanahashi, Norimasa Yamamoto, Shin Nakatani, Takuma Yamashita, Michael Tendler, Osamu Motojima

AIP Conference Proceedings 2179 (2019) 020010 (7 pages)

キノコ栽培用木材の放射性および安定セシウム濃度測定

田巻廣明、木野康志、村野井友、板橋康弘、中島丈博、郡山慎一、木村栄一、鴨原隆

KEK Proceedings of the 20th Workshop on Environmental Radioactivity, 2019 (2019) 120-125

福島原発事故後のウシ、サルの硬組織への環境中からの90Srの移行

小荒井一真, 木野康志、小野拓実、岡壽崇、高橋温、鈴木敏彦、清水良央、千葉美麗、小坂健、佐々木啓一、鈴木正敏、漆原佑介、福田智一、磯貝恵美子、関根勉、篠田壽、福本学

KEK Proceedings of the 20th Workshop on Environmental Radioactivity, 2019 (2019) 183-188

福島第一原発事故影響調査のための野生動物体内の放射性核種分布と被ばく線量の評価

小野拓実、小荒井一真, 木野康志、田巻廣明、岡壽崇、高橋温、鈴木敏彦、清水良央、千葉美麗、藤嶋洋平、Varerie Goh Swee Ting、有吉健太郎、中田章史、鈴木正敏、山城秀昭、福本学、関根勉、篠田壽、三浦富智

KEK Proceedings of the 20th Workshop on Environmental Radioactivity, 2019 (2019) 189-194

自生キノコの放射能測定による環境汚染調査

木野康志

東北大学大学院理学研究科・理学部技術「平成30年度技術部報告」(2019) 11-16

2018年に採取された自生キノコの放射能の動向

木野康志

仙台キノコ同好会会誌 43 (2019) 24-34

Fusion barrier distribution and superheavy elements
K. Hagino and T. Tanaka
J. of Phys. Conf. Ser. 1291, 012010 (2019) (7 pages).

A report on outreach activities at the Research Center for Electron Photon Science (ELPH),
H. Ohnishi,
ELPH annual report 2018

Development for the resistive plate chamber (RPC)
Y. Ishizuki, J. Takahashi, D. Taki K. Terada and H. Ohnishi,
ELPH annual report 2018

BL07Aを利用した軟X線の逆コンプトン散乱による高エネルギーガンマ線生成
村松 憲仁, 岡部 雅大, 鈴木 伸介, 伊達 伸, 清水 肇, 大熊 春夫, 神田 一浩,
宮本 修治, 原田 哲男, 渡邊 健夫, 宮部 学, 時安 敦史
ニュースバルシンポジウム2020 (2020) 76.

Recent results of SPring-8 LEPS2/ BGOegg experiment
N. Muramatsu, T. Hashimoto, Y. Matsumura, M. Miyabe, T. Nam, H. Shimizu, N. Tomida, J.K. Ahn, W.C. Chang, J.Y. Chen, S. Daté, T. Gogami, H. Hamano, Q.H. He, K. Hicks, T. Hiraiwa, Y. Honda, T. Hotta, Y. Inoue, T. Ishikawa, I. Jaegle, J.M. Jo, Y. Kasamatsu, H. Katsuragawa, S. Kido, Y. Kon, S. Masumoto, K. Miki, K. Mizutani, T. Nakamura, T. Nakano, M. Niiyama, Y. Nozawa, Y. Ohashi, H. Ohkuma, H. Ohnishi, T. Ohta, M. Oka, M. Okabe, K. Ozawa, C. Rangacharyulu, Y. Sada, M. Sasagawa, T. Shibukawa, R. Shirai, K. Shiraishi, E.A. Strokovsky, Y. Sugaya, M. Sumihama, S. Suzuki, S. Tanaka, A. Tokiyasu, Y. Tsuchikawa, T. Ueda, H. Yamazaki, R. Yamazaki, Y. Yanai, T. Yorita, C. Yoshida, and M. Yosoi
ELPH Annual Report 2018 (2019) 89–96.

Production of a high energy γ beam via inverse Compton scattering of soft x-rays from a short undulator

Norihito Muramatsu, Masahiro Okabe, Shinsuke Suzuki, Schin Daté, Hajime Shimizu, Haruo Ohkuma, Kazuhiro Kanda, Shuji Miyamoto, Tetsuo Harada, Takeo Watanabe, Manabu Miyabe, and Atsushi Tokiyasu
ELPH Annual Report 2018 (2019) 97–101.

Development of Multilayer Mirror for Producing a Next-generation Photon Beam
Masahiro Okabe, Norihito Muramatsu, and Isamu Ishikawa
ELPH Annual Report 2018 (2019) 102–104.

石川貴嗣、笠木治郎太、最近の研究から「光子ビームで探るクォーク・グルーオン多体系―ダイバリオンの発見から分光へ」、日本物理学会誌 BUTSURI 第75巻第1号、 22～27 (2020)

Development of a beam timing detector for the charmed baryon spectroscopy
T. Akaishi, T. Aramaki, H. Asano, C.-Y. Chang, W.-C. Chang, R. Honda, Y. Igarashi, T. Ishikawa, S. Kajikawa, Y. Ma, K. Nagai , H. Noumi, A. Sakaguchi, H. Sako, K. Shirotori, T.N. Takahashi for the J-PARC E50 collaboration
RCNP Annual Report 2018, Research Center for Nuclear Physics, Osaka University, p. 1-3, 2019.

Development of Prototype for the Streaming Data Acquisition System of the Charmed Baryon Spectroscopy at J-PARC
T.N. Takahashi, H. Asano, T. Akaishi, T. Aramaki, M. Chang, W.-C. Chang, R. Honda, Y. Igarashi, T. Ishikawa, S. Kajikawa4 , Y. Ma, K. Nagai, H. Noumi, H. Sako, and K. Shirotori
RCNP Annual Report 2018, Research Center for Nuclear Physics, Osaka University, p. 1-2, 2019.

ωN Scattering Length from ω Photoproduction on the Proton near the Threshold
T. Ishikawa, H. Fujimura, H. Fukasawa, R. Hashimoto, Q. He, Y. Honda, A. Hosaka, T. Iwata, S. Kaida, J. Kasagi, A. Kawano, S. Kuwasaki, K. Maeda, S. Masumoto, M. Miyabe, F. Miyahara, K. Mochizuki, N. Muramatsu, A. Nakamura, S.X. Nakamura, K. Nawa, S. Ogushi, Y. Okada, K. Okamura, Y. Onodera, K. Ozawa, Y. Sakamoto, M. Sato, T. Sato, H. Shimizu, H. Sugai, K. Suzuki, Y. Tajima, S. Takahashi, Y. Taniguchi, Y. Tsuchikawa, H. Yamazaki, R. Yamazaki, and H.Y. Yoshida

ELPH Annual Report 2018, Research Center for Electron Photon Science, Tohoku University, p. 5-9, 2019.

Study of dibaryons via $\gamma d \rightarrow \pi^0 \pi^0 d$ at E_γ=0.75–1.15 GeV (II)

T. Ishikawa, H. Fujimura, H. Fukasawa, R. Hashimoto, Q. He, Y. Honda, T. Iwata, S. Kaida, H. Kanda, J. Kasagi, A. Kawano, S. Kuwasaki, K. Maeda, S. Masumoto, M. Miyabe, F. Miyahara, K. Mochizuki, N. Muramatsu, A. Nakamura, K. Nawa, S. Ogushi, Y. Okada, K. Okamura, Y. Onodera, K. Ozawa, Y. Sakamoto, M. Sato, H. Shimizu, H. Sugai, K. Suzuki, Y. Tajima, S. Takahashi, Y. Taniguchi, Y. Tsuchikawa, H. Yamazaki, R. Yamazaki, and H.Y. Yoshida

ELPH Annual Report 2018, Research Center for Electron Photon Science, Tohoku University, p. 10-12, 2019.

Current status of the FOREST/BLC experiments at ELPH

T. Ishikawa, K. Aoki, H. Fujioka, Y. Honda, T. Hotta, Y. Inoue, K. Itahashi, H. Kanda, H. Kawai, K. Maeda, Y. Matsumura, M. Miyabe, S. Miyata, N. Muramatsu, T. Nishi, H. Ohnishi, K. Ozawa, H. Shimizu, R. Shirai, M. Tabata, A.O. Tokiyasu, Y. Tsuchikawa, H. Yamazaki, and C. Yoshida

ELPH Annual Report 2018, Research Center for Electron Photon Science, Tohoku University, p. 13-17, 2019.

Profile measurement of circulating electrons in a synchrotron using an internal radiator

Y. Obara, T. Ishikawa, H. Hama, F. Hinode, H. Kanda, S. Kashiwagi, M. Miyabe, T. Muto, K. Ozawa, H. Shimizu, and A.O. Tokiyasu

ELPH Annual Report 2018, Research Center for Electron Photon Science, Tohoku University, p. 18-21, 2019.

Performance evaluation of a scintillating fiber detector for the high-momentum secondary beamline at J-PARC

T. Aramaki, T. Akaishi, H. Asano, C.-Y. Chang, W.-C. Chang, R. Honda, Y. Igarashi, T. Ishikawa, S. Kajikawa, Y. Ma, K. Nagai, H. Noumi, H. Sako, K. Shirotori, T.N. Takahashi, and for the J-PARC E50 collaboration

ELPH Annual Report 2018, Research Center for Electron Photon Science, Tohoku University, p. 44-57, 2019.

Development of a beam-timing detector for the charmed-baryon s pectroscopy experiment at J-PARC 58

T. Akaishi, T. Aramaki, H. Asano, C.-Y. Chang, W.-C. Chang, R. Honda, Y. Igarashi, T. Ishikawa, S. Kajikawa, Y. Ma, K. Nagai, H. Noumi, A. Sakaguchi, H. Sako, K. Shirotori, T.N. Takahashi, and for the J-PARC E50 collaboration
ELPH Annual Report 2018, Research Center for Electron Photon Science, Tohoku University, p. 58-65, 2019.

Spectroscopy of electro-produced hypernuclei at JLab
S.N.Nakamura,
AIP Conference Proceedings 2130, 020012 (2019)

Studying Λ interactions in nuclear matter with the ^{208}Pb(e,e′ K$^+$)^{208} Λ Tl reaction
F. Garibaldi, O. Benhar, P. Bydžovský S. Covrig, T. Gogami, P. E. C. Markowitz, D. J. Millener, S. N. Nakamura, J. Reinhold, L. Tang, G. M. Urciuoli, and I. Vidana.,
AIP Conference Proceedings 2130, 040003 (2019).

物理科学,この1年 2020
電子で作って探る“奇妙な”原子核：最強電子線施設JLabにおけるハイパー核電磁生成分光）
中村哲 （パリティ編集委員会編）
丸善出版 2020年1月（ISBN: 9784621304860）

ラザフォードの指導を受けた日本人若手研究者---S.Obaとは誰か
萩野浩一，小林良彦，豊田直樹，中村哲
日本物理学会誌 74(9) 655 - 658 2019年9月

Proceedings of the 8th International Conference on Quarks and Nuclear Physics (QNP2018)
Editors; A.Dote, Y.Goto, A.JHosaka, S.Kumano, A.Monnai, O.Morimatsu,
S.N.Nakamura, M.Naruki, H.Noumi, S.Sawada
JPS Conference Proceedings Vol. 26 (2020) Feb.

Status of Λn interaction study via the final state interaction effect in γ d → K$^+$Λn production
Masashi Kaneta for the NKS2 collaboration
JPS Conf. Proc. 26 (2019) 023017-1 - 023017-4
DOI: 10.7566/JPSCP.26.023017

Status of a Lifetime Measurement of Light Hypernuclei Using High Intensity Tagged Photon Beam at ELPH

Y. Toyama, T. Gogami, K. Itabashi, H. Kanda, Y. Konishi, K. Maeda, S. Nagao, S.N. Nakamura, K. Uehara, and M. Kaneta.

JPS Conference Proceedings, 26 (2019) 031018.

Search for Excited State of ${}^{4}_{\Sigma}$He Hypernucleus in the J-PARC E13 Experiment

M. Nakagawa, M. Agnello, Y. Akazawa, N. Amano, K. Aoki, E. Botta, N. Chiga, H. Ekawa, P. Evtoukhovitch, A. Feliciello, M. Fujita, T. Gogami, S. Hasegawa, S.H. Hayakawa, T. Hayakawa, R. Honda, K. Hosomi, S. Hwang, N. Ichige, Y. Ichikawa, M. Ikeda, K. Imai, S. Ishimoto, S. Kanatsuki, M. Kim, S. Kim, S. Kinbara, T. Koike, J. Lee, S. Marcello7, K. Miwa, T. Moon, T. Nagae, S. Nagao, Y. Nakada, Y. Ogura, A. Sakaguchi, H. Sako, Y. Sasaki, S. Sato, T. Shiozaki, K. Shirotori, H. Sugimura, S. Suto, S. Suzuki, T. Takahashi, H. Tamura, K. Tanabe, K. Tanida, Z. Tsamalaidze, M. Ukai, T.O. Yamamoto, Y. Yamamoto, and S. Yang.

JPS Conference Proceedings, 26 (2019) 023005.

Gamma-ray spectroscopy of single Λ-hypernuclei at J-PARC: Results and perspective

T. Koike, M. Agnello, J.K. Ahn, Y. Akazawa, N. Amano, K. Aoki, E. Botta, N. Chiga, H. Ekawa, P. Evtoukhovitch, A. Feliciello, M. Fujita, T. Gogami, S. Hasegawa, S. H. Hayakawa, T. Hayakawa, R. Honda, K. Hosomi, S.H. Hwang, N. Ichige, Y. Ichikawa, M. Ikeda, K. Imai, S. Ishimoto, S. Kanatsuki, M.H. Kim, S.H. Kim, S. Kinbara, K. Kobayashi, J.Y. Lee, S. Marcello, K. Miwa, T.J. Moon, T. Nagae, S. Nagao, Y. Nakada, M. Nakagawa, Y. Ogura, A. Sakaguchi, H. Sako, Y. Sasaki, S. Sato, T. Shiozaki, K. Shirotori, H. Sugimura, S. Suto, S. Suzuki, T. Takahashi, H. Tamura, K. Tanabe, K. Tanida, Y. Togawa, Z. Tsamalaidze, M. Ukai, T.F. Wang, T.O. Yamamoto, and S.B. Yang

AIP Conference Proceedings, 2130 (2019) 020011.

Non-strange Dibaryon Resonances Observed in Coherent Double Neutral-Pion Photoproduction on the Deuteron

Takatsugu Ishikawa, Hisako Fujimura, Hiroshi Fukasawa, Ryo Hashimoto, Qinghua He, Yuki Honda, Takahiro Iwata, Shun Kaida, Hiroki Kanda, Jirohta Kasagi, Atsushi Kawano, Shuzo Kuwasaki, Kazushige Maeda, Shin'ichi Masumoto, Manabu Miyabe,

Fusashi Miyahara, Kei'ichi Mochizuki, Norihito Muramatsu, Akihiko Nakamura, Ken'ichi Nawa, Shoei Ogushi, Yasuyuki Okada, Yoshihito Onodera, Kyoichiro Ozawa, Yasunobu Sakamoto, Mamoru Sato, Hajime Shimizu, Hiroyuki Sugai, Koutaku Suzuki, Yasuhisa Tajima, Shin'ichiro Takahashi, Yusuke Taniguchi, Yusuke Tsuchikawa, Hirohito Yamazaki, Ryuji Yamazaki, and Hiroshi Y. Yoshida (FOREST collaboration)
JPS Conference Proceedings 26, 022014 (2019).

Measuring Space-Time Properties of the Δ(1232) via Bose-Einstein Correlations

Qinghua HE, Hisako FUJIMURA, Hiroshi FUKASAWA, Ryo HASHIMOTO, Yuki HONDA, Takatsugu ISHIKAWA, Takahiro IWATA, Shun KAIDA, Hiroki KANDA, Jirohta KASAGI, Atsushi KAWANO, Shuzo KUWASAKI, Kazushige MAEDA, Shinichi MASUMOTO, Manabu MIYABE, Fusashi MIYAHARA, Keiichi MOCHIZUKI, Norihito MURAMATSU, Akihiko NAKAMURA, Kenichi NAWA, Shoei OGUSHI, Yasuyuki OKADA, Yoshihito ONODERA, Kyoichiro OZAWA, Yasunobu SAKAMOTO, Mamoru SATO, Hajime SHIMIZU, Hiroyuki SUGAI, Koutaku SUZUKI, Yasuhisa TAJIMA, Shinichiro TAKAHASHI, Yusuke TANIGUCHI, Yusuke TSUCHIKAWA, Hirohito YAMAZAKI, Ryuji YAMAZAKI, Hiroshi Y. YOSHIDA (FOREST collaboration)
JPS Conference Proceedings 26, 024004 (2019).

Non-strange dibaryons studied in coherent double neutral-meson photoproduction on the deuteron

T. Ishikawa, H. Fujimura, H. Fukasawa, R. Hashimoto, Q. He, Y. Honda, T. Iwata, S. Kaida, H. Kanda, J. Kasagi, A. Kawano, S. Kuwasaki, K. Maeda, S. Masumoto, M. Miyabe, F. Miyahara, K. Mochizuki, N. Muramatsu, A. Nakamura, K. Nawa, S. Ogushi, Y. Okada, Y. Onodera, K. Ozawa, Y. Sakamoto, M. Sato, H. Shimizu, H. Sugai, K. Suzuki, Y. Tajima, S. Takahashi, Y. Taniguchi, Y. Tsuchikawa, H. Yamazaki, R. Yamazaki, H.Y. Yoshida
Acta Physica Polonica B 51, 329-332 (2020).

Performance of the FOREST/BLC Spectrometer for Study of the η-nucleon Interaction via the $\gamma d \to p \eta n$ Reaction

S. Miyata, K. Aoki, H. Fujioka, Y. Honda, T. Hotta, T. Ishikawa, K. Itahashi, H. Kanda, H. Kawai, K. Maeda, M. Miyabe, Y. Matsumura, N. Muramatsu, H. Ohnishi, K. Ozawa, H. Shimizu, M. Tabata, A.O. Tokiyasu, Y. Tsuchikawa, T. Ueda, C. Yoshida
Springer Proceedings in Physics 238, 705-708 (2020).

Study of Non-strange Dibaryon Resonances Via Coherent Double Neutral-Meson Photoproduction from the Deuteron

T. Ishikawa, H. Fujimura, H. Fukasawa, R. Hashimoto, Q. He, Y. Honda, T. Iwata, S. Kaida, H. Kanda, A. Kawano, S. Kuwasaki, K. Maeda, S. Masumoto, M. Miyabe, F. Miyahara, K. Mochizuki, N. Muramatsu, A. Nakamura, K. Nawa, S. Ogushi, Y. Okada, K. Okamura, Y. Onodera, K. Ozawa, Y. Sakamoto, M. Sato, H. Shimizu, H. Sugai, K. Suzuki, Y. Tajima, S. Takahashi, Y. Taniguchi, Y. Tsuchikawa, H. Yamazaki, R. Yamazaki, H.Y. Yoshida

Springer Proceedings in Physics 238, 609-613 (2020).

Electromagnetic calorimeter BGOegg for quark nuclear physics

H. Shimizu (LEPS2/BGOegg Collaboration)

KEK Proceedings 2019-4 (December 2019) pp. 51-63.

軟X線を用いた逆コンプトン散乱による高エネルギーガンマ線ビームの開発

村松憲仁、岡部雅大、鈴木伸介、伊達伸、清水肇、大熊春夫、神田一浩、宮本修治、原田哲男、渡邊健夫、宮部学、時安敦史

「加速器」Vol.16, No.3, 2019 (154-160).

Review of permeation-induced nuclear transmutation reactions

Yasuhiro. Iwamura

Cold Fusion: Advances in Condensed Matter Nuclear Science, Ed. Jean-Paul Biberian, Elsevier, Amsterdam, (2020)191-204.

Heat generation experiments using nano-sized metal composite and hydrogen gas

Yasuhiro Iwamura

Cold Fusion: Advances in Condensed Matter Nuclear Science, Ed. Jean-Paul Biberian, Elsevier, Amsterdam, (2020)157-165.

Overview of Condensed Matter Nuclear Reaction Division

Yasuhiro Iwamura

ELPH annual report 2018, (2019) 3-4.

光子ビームで探るクォーク・グルーオン多体系　～ダイバリオンの発見から分光へ

石川貴嗣、笠木治郎太

日本物理学会誌、第 75 巻第 1 号、 pp. 22 - 26 (2020)

Screening Energy for Low Energy Nuclear Reactions in Condensed Matter
J. Kasagi, Y. Honda, K. Fang
"Cold Fusion -Advances in Condensed Matter Nuclear Science-" (Elsevier Inc., 2020), pp 167-187.

Study of silicon sensors for precise timing measurement
Y. Deguchi, K. Kawagoe, R. Mori, E. Mestre, T. Suehara and T. Yoshioka:
2020 JINST 15 C05051

Study of Position Sensitive Silicon Detector (PSD) for SiW-ECAL at ILC
Y. Uesugi, R. Mori, H. Yamashiro, T. Suehara, T. Yoshioka, K. Kawagoe
2020 JINST 15 C05033

Invited Talk, Oral, and Poster Presentations at International Conferences

Crossed-Undulator Configuration for Variable Polarized THz Source
H. Hama
39th Free Electron Laser Conf. (FEL2019), 25 – 30 August, 2019, Hamburg, Germany.

Designing work of a compact 3 GeV light source employing multi-bend lattice (Invited talk)
Hiroyuki Hama
National Synchrotron Radiation Laboratory, University of Science and Technology of China, 12th November, 2019, Hefei, China.

Superconducting Electron Accelerators for Various Applications (Invited talk)
Hiroyuki Hama
Int. Conf. on Radiation and Emission in Materials 2019, 18th December, 2019, Bangkok, Thailand.

Demonstration of variable polarized coherent terahertz source (Poster presentation)
S. Kashiwagi, H. Saito, F. Hinode, Y. Ishizuki, K. Kanomata, S. Miura, N. Morita, T. Muto, I. Nagasawa, K. Nanbu, K. Shibata, K. Takahashi, H. Hama, H. Zen and A. Irizawa

The 10th International Workshop on Infrared Microscopy and Spectroscopy with Accelerator Based Sources, WIRMS 2019
23-27 September, 2019 Campinas & Ubatuba, Brazil

Measurement of Cherenkov Diffraction Radiation from Short Electron Bunches at t-ACTS,
F. Hinode
10th Int. Particle Accelerator Conference, Melbourne (Australia), May 19-24, 2019, (Poster)

"Proton Charge Radius by Low-Energy Electron Scattering"
T. Suda
International workshop on the structure of the proton, Yamagata, Feb. 10-11,（招待講演）

"Nuclear Physics with low-energy and high-intensity electron beam"
T. Suda
Neutrino Nuclear Response 2019 (NNR19), RCNP, Osaka, May 8-9, (口頭発表)

"Electron Scattering for Short-Live Nuclei"
T. Suda
Gordon Conference on "Exploring simple structural patterns and dynamics of nuclei" June 16-21, New London US, （招待講演）

"Nuclear Physics with Electron Beam"
T. Suda
Connecting Fundamental Physics, Chemistry and the Origins of Biomolecular Homochirarity, June 26-27, National Observatory of Japan, （招待講演）

"Electron scattering for short-lived nuclei"
T. Suda
International Nuclear Physics Conference 2019, July 29-Au. 2, Glasgow UK, (Plenary talk)

"Proton Radius"
T. Suda

The 11th Circum-Pan-Pacific Symposium on High Energy Spin Physics, Aug. 27-30, Miyazaki, （招待講演）

"Proton Radius"

T. Suda

14th Asia-Pacific Physics Conference, Nov. 17-22, Kuching Malyasia, （招待講演）

"Electron-scattering activities in Japan for nucleon and nuclei"

T. Suda

KVI seminar, Jan. 8, KVI Groningen, Netherlands, （招待講演）

"ULQ2 project"

T. Suda

Collaborative Seminar by REIMEI, RCNP and Clusters, Feb. 20, （招待講演）

Present status and prospects of the SCRIT electron scattering facility

K. Tsukada

The 9th International Symposium on Nuclear Symmetry Energy (NuSYM2019)

Danang City, Vietnam, Sept. 30 to Oct. 4, 2019 (一般講演)

Present status of SCRIT electron scattering facility

K. Tsukada

The 14th Asia-Pacific Physics Conference (APPC2019)

Kuching, Malaysia, 17 Nov. to 22 Nov., 2019 (一般講演)

Elastic electron-proton scattering with low-energy electron beam at ELPH.

Y. Honda

HU physics colloquium, Hampton, USA, April 25, 2019.（招待講演）

Status of Nuclear Physics in Japan -- Future Projects --

H. Tamura

ANPHA 2019 Symposium, Jeju, Korea, June 28-29, 2019（招待講演）

Hypernuclear Physics – Recent Results and Future Prospects

H. Tamura

Symposium on Rare Isotope Sciences, Institute for Basic Science, Daejeon, Korea, July 10, 2019（招待講演）

Hypernuclear Physics -- How to Solve the Hyperon Puzzle --
H. Tamura
International Symposium on Nuclear Symmetry Energy (NuSYM2019),
Da Nan, Vietnam, Sept. 30 - Oct. 4, 2019　（招待講演）

J-PARC Heavy Ion Project
H. Tamura
THEIA-STRONG2020 workshop 2019,
Speyer, Germany, November 25-29, 2019（招待講演）

Hypernuclear Physics at J-PARC
H. Tamura
THEIA-STRONG2020 workshop 2019,
Speyer, Germany, November 25-29, 2019

Status and perspective of hypernuclear physics at J-PARC
H. Tamura
3rd EMMI Workshop: Anti-matter, hyper-matter and exotica production at the LHC
Wroclaw, Poland, December 2-6, 2019（招待講演）

Possible Modification of a Hyperon in Hypernuclei
H. Tamura
STRANEX: Recent progress and perspectives in STRANge EXotic atoms studies and related topics
ECT*, Trento, Italy, Oct. 21-25, 2019

Experimental studies on possible modification of baryons in nuclei
H. Tamura
International symposium on Clustering as a Window on the Hierarchical Structure of Quantum Systems (CLUSHIQ2020)
Beppu, Japan, Jan. 23-24, 2020

Elucidation of the mechanism of Na+ and Cs+-induced cell growth through cation transporters

Nobuyuki Uozumi, Masaru Tsujii, Ellen Tanudjaja and Kota Kera

18th International Workshop on Plant Membrane Biology, July 7-12, Glasgow UK

Energy levels and stabilities of muonic molecule in muon catalyzed fusion

Yasushi Kino

15th International Conference of Computational Methods in Sciences and Engineering (ICCMSE 2019), Rhodes, Greece, 2019/5/1-5. (Invited talk)

Reaction dynamics for hot fusion reactions with a deformed nucleus

K. Hagino

The 4th International Symposium on Superheavy Elements (SHE2019)・箱根・2019 年 12 月 1-5 日

Perspectives on nuclear reaction theory and superheavy elements superheavy regions

K. Hagino

Workshop on nuclear physics and nuclear astrophysics・Soongsil大学・2020 年 1 月 15 日

ϕ meson in nucleus

H. Ohnishi

STRANEX: Recent progress and prespectives in STRANge Exotic atoms studies and related topics, 10/21-25/2019, ECT*, Trento, Italy [招待講演]

Hadron Physics with anti-proton at J-PARC

H. Ohnishi

E50 DAQ Meeting, 5/17/2019, Institute of Physics, Academia Sinica, 台湾 [招待講演]

Recent Progress and Prospects of the LEPS2/BGOegg Experiment at SPring-8

N. Muramatsu

3rd Jagiellonian Symposium on Fundamental and Applied Subatomic Physics, Jagiellonian Univ., Krakow, Poland, June 23-28, 2019 (招待講演).

Production of a coherent bremsstrahlung photon beam with several tens of GeV at ILC

N. Muramatsu

International Workshop on Future Linear Colliders (LCWS 2019), Sendai, Oct. 28 - Nov. 1, 2019 (口頭発表).

ωN scattering length from ω photoproduction on the proton near the threshold,

T. Ishikawa

The 15th International Conference on Meson-Nucleon Physics and the Structure of the Nucleon, MENU2019, Cohon University Center, Carnegie Mellon University, Pittsburgh Pennsylvania, USA, Jun. 2-7, 2019, 口頭発表

Non-Strange Dibaryons studied in coherent double neutral-meson photoproduction on the deuteron

T. Ishikawa

The 12th Internal workshop on the Physics of Excited Nucleons (NSTAR2019), Poppelsdof Campus, Bonn University, Bonn, Germany, Jun 10-14, 2019, 口頭発表

ηN scattering parameters and possible η'N bound state from η photoproduction on the deuteron

T. Ishikawa

3rd Jagiellonian Symposium on Fundamental and Applied Subatomic Physics, Krakow, Poland, Jun. 23-28, 2019, 招待講演

Non-strange dibaryons studied in coherent double neutral-meson photoproduction on the deuteron

T. Ishikawa

3rd Jagiellonian Symposium on Fundamental and Applied Subatomic Physics, Krakow, Poland, Jun. 23-28, 2019, ポスター発表

ωN scattering length from ω photoproduction on the proton near the threshold,

T. Ishikawa

The 14th Asia-Pacific Physics Conference 2019 (APPC2019), Borneo Convention Center Kuching, Sarawak, Malaysia, Nov. 17-22, 2019, 口頭発表

Photo-production of the eta-meson on the deuteron,

T. Ishikawa
International Symposium on Clustering as a Window on the Hierarchical Structure of Quantum Systems (CLUSHIQ2020), Beppu, Jan 23-24, 2020、ポスター発表

Dibaryon photoproduction on the deuteron detecting two neutral pions and deuteron,
T. Ishikawa
KEK/Tokai Internal workshop on "Physics of heavy-quark and exotic hadrons", KEK-Tokai Campus, Tokai, Jan 26-28, 2020、招待講演

Ideas of Kaonicnuclei search at LEPS
A. O. Tokiyasu
Kaon Physics at DAΦNE, J-PARC @ RIKEN, and SPring-8, Dec. 19th (招待講演)

Axion Search Experiment:Past, present, and future
A. O. Tokiyasu
KMI seminar @ Nagoya University, May 13th, 2019 (招待講演)

Study of the phi meson bound state in nucleus in J-PARC K1.8BR beamline
Y. Sada
International symposium on Clustering as a Window on the Hierarchical Structure of Quantum Systems (CLUSHIQ2020), Beppu, Oita, Japan, January 23-24 (ポスター)

Strangeness Nuclear Physics with Electron/Photon Beams,
S.N.Nakamura
THEIA-STRONG2020-Workshop2019, Speyer, Germany 2019.11.25 (口頭発表)

Status of Experiment for Λn Interaction Measurement via Final State Interaction in γ d → K^+Λn Production
Masashi Kaneta for the NKS2 collaboration
The 14th Asia-Pacific Physics Conference 2019 (APPC14)
2019/11/17-22　招待講演

Design of New Particle Charge Separation Magnet
S. Nagao

International meeting for electron beam spectroscopy of Λ hypernuclei: nnΛ analysis (JLab E12-17-003), Kyoto, Japan, May 24 (一般公演)

Precision Spectroscopy of Lambda Hypernuclei with Electro-photo production
S. Nagao
3rd EMMI Workshop, Wrocław, Poland, December 5 (招待講演)

Overview of lifetime measurements on hyper-hydrogens at ELPH Tohoku
S. Nagao
Workshop on electro- and photo-production of hypernuclei 2020, Prague, Czech, February 16 (一般公演)

Design & Construction of new separation magnets for the next hypernuclear experiment
S. Nagao
JLab Hall-A meeting, Newport News, USA, March 3

Excess Energy Generation using a Nano-sized Multilayer Metal Composite and Hydrogen Gas
Y. Iwamura, T. Itoh, S. Murakami, Mari Saito and J Kasagi,
22nd International Conference on Condensed Matter Nuclear Science; ICCF-22
Hotel and Conference Centre Domus Pacis, Assisi, Italy, September 8-13, 2019.
（口頭発表）

Possible radiation from thin film metal surface with anomalous excess heat: Can we observe hot spots or Bremsstrahlung?
J. Kasagi
The 22nd International Conference on Condensed Matter Nuclear Science ICCF22, Assisi, Italy, September 9-13, 2019 (口頭発表)

"Precise magnetic field measurement of electron spectrometer for the electron scattering off unstable nuclei experiment"、
Hikari Wauke (M2)
International school for Strangeness Nuclear Physics 2019、東北大学、2019.09.05-08、ポスターセッション、SNP School Incentive Prize　受賞

Development of an aerogel Cherenkov counter for the LEPS2 solenoid experiment at SPring-8

Chihiro Yoshida、
International Symposium on Clustering as a Window on the Hierarchical Structure of Quantum Systems (CLUSHIQ2020)、別府、2020/1/23 - 2020/1/24、ポスター

Study of silicon sensors for precise timing measurement

Y. Deguchi, K. Kawagoe, R. Mori, E. Mestre, T. Suehara and T. Yoshioka:
Calorimetry for High Energy Frontier (CHEF2019), Nov. 2019, Fukuoka, Japan

Study of Position Sensitive Silicon Detector (PSD) for SiW-ECAL at ILC

Y. Uesugi, R. Mori, H. Yamashiro, T. Suehara, T. Yoshioka, K. Kawagoe
Calorimetry for High Energy Frontier (CHEF2019), Nov. 2019, Fukuoka, Japan

Time Projection Chamber "HypTPC" for the hadron spectroscopy at J-PARC

Y. Ichikawa for the J-PARC E42, E45, E72 Collaborations,
J-PARC Symposium 2019, Tsukuba, Japan, 2019 Sept.

学位論文（センター内）

修士（理学）

岡部 雅大
「軟X線の逆コンプトン散乱による高エネルギー光子ビームの開発」
（指導教員：大西 宏明）

森田 希望
「低エネルギー極短電子パルスのビーム輸送におけるバンチ伸長に関する研究」
（指導教員：濱 広幸）

山田 悠樹
「極短電子ビームによるコヒーレントスミス=パーセル放射の研究」
（指導教員：濱 広幸）

竹屋 匡皓
「金属-水素ガス系における異常発熱測定のためのフローカロリーメータの詳細テスト」
（指導教員：菊永英寿、笠木治郎太）

和宇慶 ひかり

「SCRIT電子スペクトロメータの3次元磁場測定」（指導教員：須田 利美）

学位論文（センター外）

修士論文

東 大起（東北大学・工）

「植物カリウム吸収・移行を調節する輸送体KUP/HAKの機能解析」

（指導教員：魚住 信之）

出口 遊斗, 2019年度九州大学修士学位論文

「国際リニアコライダーにおける粒子識別精度向上のための高時間分解能シリコンセンサー開発に向けた研究」

（指導教員: 末原大幹（主査: 川越清以））

上杉 悠人, 2019年度九州大学修士学位論文

「国際リニアコライダーのための高位置分解能シリコンセンサーの開発」

（指導教員: 末原大幹（主査: 川越清以））

IV. Members of Committees

Steering Committee

2019

HAMA Hiroyuki*	ELPH
SUDA Toshimi	ELPH
OHNISHI Hiroaki	ELPH
HINODE Fujio	ELPH
KASHIWAGI Shigeru	ELPH
MURAMATSU Norihito	ELPH
KIKUNAGA Hidetoshi	ELPH
TAMURA Hirokazu	Graduate School of Science
NAKAMURA Satoshi	Graduate School of Science
HAGINO Kouichi	Graduate School of Science
SASAKI Shoichi	Graduate School of Science
MISAIZU Fuminori	Graduate School of Science
KINO Yasushi	Graduate School of Science
UOZUMI Nobuyuki	Graduate School of Engineering
MATSUYAMA Shigeo	Graduate School of Engineering
KASADA Ryuta	Institute for Materials Research
TAKAKUWA Yuji	Institute of Multidisciplinary Research for Advanced Materials
EJIMA Takeo	Institute of Multidisciplinary Research for Advanced Materials
EDAMATSU Keiichi	Research Institute of Electrical Communication
ITOH Masatoshi	Cyclotron and Radioisotope Center
TSUDA Kenji	Frontier Research Institute for Interdisciplinary Sciences

* Chairperson

General Advisory Committee

2019

HAMA Hiroyuki*	ELPH, Tohoku University
SUDA Toshimi	ELPH, Tohoku University
OHNISHI Hiroaki	ELPH, Tohoku University
KIKUNAGA Hidetoshi	ELPH, Tohoku University
TAMURA Hirokazu	Graduate School of Science, Tohoku University
KINO Yasushi	Graduate School of Science, Tohoku University
ITOH Masatoshi	Cyclotron and Radioisotope Center, Tohoku University
TSUDA Kenji	Frontier Research Institute for Interdisciplinary Sciences, Tohoku University
UESAKA Tomohiro	RIKEN Nishina Center
HIRENZAKI Satoru	Faculty Division of Natural Science, Nara Women's University
NAKANO Takashi	RCNP, Osaka University
SAWADA Shinya	Institute for Particle and Nuclear Studies, KEK
KATO Ryukou	Accelerator Laboratory, KEK
OHGAKI Hideaki	IAE, Kyoto University
SHINOHAR Atsushi	Graduate School of Science, Osaka University
OURA Yasuji	Graduate School of Science and Engineering, Tokyo Metropolitan University

* Chairperson

Program Advisory Committee

2019

SUDA Toshimi	ELPH, Tohoku University
OHNISHI Hiroaki	ELPH, Tohoku University
KASHIWAGI Shigeru	ELPH, Tohoku University
KIKUNAGA Hidetoshi	ELPH, Tohoku University
NAKAMURA Satoshi*	Graduate School of Science, Tohoku University
SUGIYAMA Kazumasa	Institute for Materials Research, Tohoku University
OZAWA Kyoichiro	Graduate School of Science, KEK2
HOTTA Tomoaki	RCNP, Osaka University
FUJIOKA Hiroyuki	School of Science, Tokyo Institute of Technology
SHOJI Yoshihiko	LASTI, University of Hyogo
GOTO Shin-ichi	Graduate School of Science and Technology, Niigata University
KUBOTA Takumi	Institute for Integrated Radiation and Nuclear Science, Kyoto University

* Chairperson

V. Approved Experiments

2019 年度採択課題

課題番号	課題名	申込責任者
2915	T2K 実験ミューオンモニターのための新型検出器・電子増倍管の電子ビームを用いた性能評価	市川温子
2916	LEPS2 ソレノイド実験のためのエアロゲルチェレンコフカウンターの性能評価	時安敦史
2917	グザイハイパー核分光実験 J-PARC E70 に用いるアクティブシンチレーションファイバ標的の性能試験	後神利志
2918	ハドロン生成実験 EMPHATIC のためのエアロゲルチェレンコフ検出器の開発	田端誠
2920	放射性バナジウム V-48 を用いたバナジウム・レドックスフロー電池の隔膜の研究 ～加速器による V-48 の製造・第 3 期～	白崎謙次
2921	電子ライナック由来 Tc-99m を用いたネズミイメージングのための Mo-99 製造	上坂充
2922	Performance evaluation for a Cherenkov calorimeter with PbF2 crystal	MA, Yue
2923	ハドロン生成実験 EMPHATIC に向けた RICH 検出器のためのマルチレイヤーエアロゲルスキームの最適化	田端誠
2924	FOREST 超前方荷電粒子検出で拓く物理	石川貴嗣
2925	高時間分解能飛行時間差測定装置(resistive plate chamber)特性の高抵抗膜電極依存性の研究	大西宏明
2926	4 年生学生実験：環境に優しいガスを使った Multi-Gap Resistive plate Chamber の基礎研究	大西宏明
2927	LEPS2 ソレノイド実験のためのエアロジェルチェレンコフカウンターの性能評価 II	時安敦史
2928	J-PARC E42 実験のための水チェレンコフ検出器のビーム試験	市川裕大
2929	FOREST 前方ホドスコープ SPIDER の改良	石川貴嗣
2930	γd→dX 反応の断面積測定	藤岡宏之
2931	JLab における高精度ハイパー核分光実験のための水チェレンコフ検出器の性能評価	永尾翔

2932	MPPC を用いたビーム位置検出器の開発と電子・陽電子ビーム形状の測定 II	宮部学
2933	PPD 構造を持つ SOI ピクセルセンサーの電荷収集効率の測定	坪山透
2934	FOREST 超前方 π+/K+メソン識別用 AC の最終テスト	石川貴嗣
2935	時間分解能・位置分解能を実現する新型シリコンセンサーの評価	末原大幹
2936	超低運動量移行領域での電子散乱による陽子の荷電半径測定	本多佑記
2937	Λn Interaction Study via the Final State Interaction Effect in γd→K+Λn Production	金田 雅司
2938	家庭ごみ焼却スラグに含まれる希少金属元素の回収を目指した光量子放射化法による成分同定およびトレーサー作成 4	秋山 和彦
2939	放射性バナジウム V-48 を用いたバナジウム・レドックスフロー電池の隔膜の研究～加速器による V-48 の製造・第 4 期～	白崎 謙次
2940	塩化水銀(I)のトレーサスケールにおける揮発挙動研究のための無担体 203Hg の製造	後藤真一
2941	Ra-226(γ,n)反応の反応収率測定	菊永英寿

ELPH Annual Report 2019

(April 2019-March 2020) March 2021
ONLINE ISSN 2435-9165

Published by
Research Center for Electron-Photon Science (ELPH), Tohoku University
1-2-1 Mikamine, Taihaku, Sendai, Miyagi 982-0826, Japan
Phone: +81-22-743-3411
FAX: +81-22-743-3402
Email: koho@lns.tohoku.ac.jp
Homepage: https://www.lns.tohoku.ac.jp/

2021 年（令和 3 年）3 月 31 日 発行
発行者 国立大学法人東北大学電子光理学研究センター
センター長 濱 広幸
〒982-0826 宮城県仙台市太白区三神峯 1－2－1
電話： 022-743-3411
FAX： 022-743-3402
Email： koho@lns.tohoku.ac.jp
ホームページ：https://www.lns.tohoku.ac.jp/